

AGE-RELATED CHANGES IN HUMAN ANATOMICAL AND FUNCTIONAL BRAIN  
NETWORKS

Richard F. Betzel

Submitted to the faculty of the University Graduate School  
In partial fulfillment of the requirements  
For the degree  
Doctor of Philosophy  
In the Department of Psychological and Brain Sciences  
Indiana University  
September 2015

Accepted by the Graduate Faculty, Indiana University, in partial fulfillment of the requirements for the degree of Doctor of Philosophy.

Doctoral Committee

---

Olaf Sporns, Ph. D.

---

Yong-Yeol Ahn, Ph. D.

---

John M. Beggs, Ph.D.

---

Daniel P. Kennedy, Ph. D.

September 17, 2015



## ACKNOWLEDGEMENTS

While this dissertation bears my name, it was only possible because I had such a strong supporting cast of advisors, committee members, educators, lab-mates, and collaborators willing to work late at night and on weekends, tolerate long (and, let's face it, usually unproductive) conversations about brains and networks, humor me and my requests to reprocess data, and otherwise provide the perfect culture for a young(ish) scientist to flourish.

I would be remiss if I failed to thank Olaf Sporns. Five years ago I whimsically enrolled in a course entitled "Networks of the Brain," expecting only that I would learn a bit about brains and maybe a little network science, too. Instead, what I got from that course was a mentor and a friend.

To my lab-mates (past and present): Joaquín Goñi, Andrea Avena-Koenigsberger, Nieves Velez de Mendizabal, Artemy Kolchinsky (you're an honorary lab member, of course), Bratislav Mišić, Peng Fang, Jeff Rumschlag, Rui Cao, and Makoto Fukushima. This dissertation grew out of our discussions and lab meetings and would never have been possible were it not for all of you: while true; fprintf("Thank you for everything\n"); end;

To all my collaborators and visitors to the lab, especially Alessandra Griffa, Patric Hagmann, Martijn van den Heuvel, Ye He, and Xi-Nian Zuo: By donating your time and devoting countless CPU cycles to processing MRI data and running tractography, you have made it possible for me to complete a Ph.D. without collecting even a single kilobyte of my own data. I am eternally grateful.

I would also like to thank my brothers: Adam, Mark, and Alex. The only reason I ever wanted a Ph.D. was to demonstrate, unequivocally, that I am better and smarter than all of you. Never forget this.

To my parents, Diane and Edward: It was your unwavering support, encouragement, enthusiasm, and love that made this dissertation possible.

This dissertation is dedicated to Galina. Everything I do in life starts and stops with you. I love you.

Richard F. Betzel

AGE-RELATED CHANGES IN HUMAN ANATOMICAL AND FUNCTIONAL BRAIN NETWORKS

The human brain can be treated as a network of brain regions and functional/structural connections. An important question is how the organization of brain networks changes over the human lifespan. This dissertation address this question with three components:

- i) The first component characterizes age-related changes in specific connections. We find that functional connections within and between intrinsic connectivity networks (ICNs) follow distinct lifespan trajectories. We further characterize these changes in terms of each ICN’s “modularity” and find that most ICNs become less modular (i.e. less segregated) with age. In anatomical networks we find that hub regions are disproportionately affected by age and become less efficiently connected to the rest of the brain. Finally, we find that, with age stronger functional connections are supported by longer (multi-step) anatomical pathways for communication.
- ii) The second component is concerned with characterizing age-related changes in the boundaries of ICNs. To this end we used a multi-layer variant of modularity maximization to decompose networks into modules at different organizational scales, which we find exhibit scale-specific trends with age. At coarse scales, for example, we find that modules become more segregated whereas modules defined at finer scales become less segregated. We also find that module composition changes with age, and specific areas associated with memory change their module allegiance with age.
- iii) In the final component we use generative models to uncover wiring rules for the anatomical brain networks. Modeling network growth as a spatial penalty combined with homophily, we find that we can generate synthetic networks with many of the same properties as real-world brain networks. Fitting this model to individuals, we show that the parameter governing the severity of the spatial penalty weakens monotonically with age and that the overall ability to reproduce realistic connectomes for older individuals suffers. These results suggest that, with age, additional constraints may play an important role in shaping the topology of brain structural networks.

---

Olaf Sporns, Ph. D.

---

Yong-Yeol Ahn, Ph. D.

---

John M. Beggs, Ph.D.

---

Daniel P. Kennedy, Ph. D.

## TABLE OF CONTENTS

Chapter 1: Introduction.....	1
1.1. Overview.....	1
1.2. Network science.....	3
1.3. Network science applied to neural systems.....	4
1.4. Flavors of connectivity.....	4
1.5. Empirical studies of brain connectivity.....	8
1.6. Summary of research contributions.....	12
Chapter 2: Changes in structural and functional connectivity among resting-state networks across the human lifespan.....	14
2.1. Introduction.....	16
2.2. Methods and materials.....	18
2.2.1. NKI-RS lifespan sample and image preprocessing.....	18
2.2.2. Construction of FC networks.....	20
2.2.3. Construction of SC networks.....	21
2.2.4. Multiple linear regression analysis.....	23
2.2.5. FC edge trajectories.....	25
2.2.6. FC modularity analysis.....	25
2.2.7. SC measures and hubs.....	26
2.2.8. Path efficiency framework.....	27
2.2.9. FC distance dependence.....	28
2.3 Results.....	29

2.3.1. FC decreases within RSNs and tends to increase between RSNs.....	29
2.3.2. RSNs modularity decreases with age.....	31
2.3.3. Structural changes across the lifespan .....	31
2.3.4. Communication capacity decreases in proportion to “hubness” .....	32
2.3.5. Magnitude of age x FC correlation is dependent upon topological distance .....	33
2.4. Discussion.....	34
2.4.1. Lifespan changes in functional connectivity.....	35
2.4.2. Lifespan changes in structural connectivity.....	37
2.4.3. Implications for lifespan changes in communication patterns.....	39
2.4.4. Limitations of current study.....	42
2.4.5. Conclusions.....	45
2.4.6. Acknowledgements.....	45
Chapter 3: Functional brain modules reconfigure at multiple scales across the human lifespan .....	46
3.1. Introduction.....	47
3.2. Methods.....	50
3.2.1. Data acquisition and processing.....	50
3.2.2. Network construction.....	51
3.2.3. Single-scale modularity .....	52
3.2.4. Multi-scale modularity maximization.....	54
3.2.5. Multi-layer, multi-scale modularity maximization.....	55
3.2.6. Network measurements.....	57
3.2.7. Null models.....	58

3.3. Results.....	59
3.3.1. Multi-layer/multi-scale modularity maximization uncovers known ICNs.....	60
3.3.2. Age-dependent changes in community structure are scale dependent.....	60
3.3.3. Community structure varies with age.....	63
3.3.4. Functional roles change with age.....	65
3.4. Discussion.....	66
3.4.1. Age-related change in community structure varies with scale.....	67
3.4.2. Possible mechanisms.....	69
3.4.3. Community detection for functional brain networks.....	70
3.4.4. Methodological Considerations.....	72
3.4.5. Conclusion.....	73
Chapter 4: Generative models of the human connectome.....	74
4.1. Introduction.....	75
4.2. Results.....	77
4.2.1. Geometric models cannot generate clustered networks with long connections.....	79
4.2.2. Models driven by geometry and topology outperform pure geometric models.....	80
4.2.3. Evaluating synthetic networks using additional measures.....	82
4.2.4. Graph theoretic measures.....	82
4.2.5. Distance-dependent degree assortativity.....	83
4.2.6. Local statistics.....	84
4.2.7. Application to human lifespan data.....	85
4.3. Discussion.....	85

4.4. Methods.....	91
4.4.1. Generative algorithm .....	91
4.4.2. Model optimization.....	92
4.4.3. Data acquisition and processing.....	93
4.5. Supplement .....	93
4.5.1. Additional Datasets.....	94
4.5.2. Fiber length versus Euclidean distance.....	97
Chapter 5: Conclusion.....	98
5.1. Dissertation summary .....	98
5.2. Limitations .....	100
5.3. Future work.....	102
Figures.....	106
Figure 2.1 .....	106
Figure 2.2 .....	107
Figure 2.3 .....	108
Figure 2.4.....	109
Figure 2.5 .....	110
Figure 2.6.....	111
Figure 2.7 .....	112
Figure 2.8 .....	113
Figure 2.9 .....	114

Figure 2.10 .....	115
Figure 2.11 .....	116
Figure 2.12 .....	117
Figure 2.13 .....	118
Figure 2.14 .....	119
Figure 3.1 .....	120
Figure 3.2 .....	121
Figure 3.3 .....	122
Figure 3.4 .....	124
Figure 3.5 .....	125
Figure 3.6 .....	126
Figure 3.7 .....	127
Figure 3.8 .....	129
Figure 3.9 .....	130
Figure 3.10 .....	131
Figure 3.11 .....	133
Figure 3.12 .....	135
Figure 3.13 .....	137
Figure 3.14 .....	138
Figure 3.15 .....	140
Figure 3.16 .....	141
Figure 3.17 .....	142

Figure 3.18 .....	143
Figure 4.1 .....	144
Figure 4.2 .....	145
Figure 4.3 .....	146
Figure 4.4 .....	148
Figure 4.5 .....	149
Figure 4.6 .....	150
Figure 4.7 .....	151
Figure 4.8 .....	152
Figure 4.9 .....	153
Figure 4.10 .....	154
Figure 4.11 .....	155
Figure 4.12 .....	156
Figure 4.13 .....	157
Figure 4.14 .....	158
Table 4.1 .....	159
Appendix A1. GRAPH THEORETIC TERMINOLOGY .....	160
References .....	164
Curriculum Vitae .....	184



## **CHAPTER 1: INTRODUCTION**

### **1.1 Overview**

It has become increasingly common to study the human brain under the auspices of modern network science (Bullmore & Sporns 2009). To render such a complex organ into a format amenable to network analysis necessarily distills away many important details of the brain's organization; what remains, however, is a concise and mathematically tractable description of the connections among neural elements: the human "connectome". At the macroscopic scale, the human connectome describes the network of myelinated fiber bundles that link together brain regions over long distances. The connectome acts to facilitate and constrain the flow of information between brain regions. From these constraints emerges a "functional network" whose connectivity pattern reflects the interdependence of brain regions' activity and, ostensibly, the propensity for brain regions to communicate with one another (Friston 2011).

In the nascent field of network neuroscience one of the principle goals is to understand how brain networks help support human cognition. The processes of healthy development, maturation, and senescence are typified by profound cognitive changes; both early and late in life we manifest cognitive frailty, while the middle of our lives are characterized by robust function (Craik & Bialystok 2006). For this reason, it is important and natural that we try to answer the question whether such overt changes in cognitive capacity across the lifespan are accompanied or precipitated by changes in brain connectivity.

This dissertation summarizes several studies undertaken in an attempt to help address this question. These studies make use of two freely available datasets, released as part of the Nathan

Kline Institute (NKI), Rockland, NY lifespan sample (Nooner et al 2012) and include functional, diffusion-weighted, and structural magnetic resonance imaging (MRI) scans for 126 and 316 individuals aged 7-85 years. From these data, we reconstructed each individual participant's connectome as well as generated an estimate of their functional brain network. We characterized the organization of these networks using tools from network science, thereby allowing us to track the evolution of different organizational aspects across the human lifespan.

This dissertation is divided into five chapters. The middle three chapters represent three papers that are in some stage of peer review or have already been reviewed. The other two chapters serve as an introduction and discussion, bookending the middle three:

- In Chapter 1 we discuss, broadly, the basic tenets of network science, focusing on their application to neural systems.
- In Chapter 2 we characterize basic structural and functional changes in brain networks across the lifespan, paying close attention to how these changes relate to “intrinsic connectivity networks” (ICNs) which represent distinct functional sub-systems. This chapter is based on the published text of Betzel et al (2014).
- In Chapter 3 we use community detection methods to identify multi-scale modules, which we relate to canonical ICNs. We show that cortical modules undergo scale-specific changes with respect to age. This chapter is based on the manuscript Betzel et al (2015a).
- In Chapter 4 we leverage network generative modeling techniques in an attempt to disentangle the wiring rules that underlie the organization of the human connectome. This chapter follows the text of Betzel et al (2015b).

- Chapter 5 summarizes the previous chapters, discusses their contribution to the research area of network neuroscience, and identifies several avenues for future work.

As much as possible, these chapters adhere to the structure of the articles that they are based on. In some cases this may cause mild confusion, as nomenclature used in one article may be slightly different from that of another. To help mitigate such issues, an appendix of commonly used terminology is included at the end of this dissertation.

## **1.2 Network Science**

It has become commonplace to study the organization of the networks that underlie complex systems (Costa et al 2007; Börner et al 2007). The systems that lend themselves to this approach are varied, and include both real and virtual societies (Leskovec et al 2008; Traud et al 2011), economies (Hidalgo & Hausmann 2009), disease (Barabási et al 2011), food and ingredients (Ahn et al 2011), as well as nervous systems like the human brain (Sporns 2011), to name but a few. Though these systems are varied in terms of their defining features and characteristics, each can be modeled as a network. For a single model to successfully capture such variety, complex systems must be recast into a common framework, namely one that expresses a system's elements as a set of points (nodes) and the interactions among pairs of those elements as a set of lines (links). What these two sets represent depends upon the system in question. A network model of society might define nodes to be individual agents; whether two nodes share a connection is then based on the friendship status of the individuals that they represent. In a network model of cellular function (Barabási & Oltvai 2004), on the other hand, nodes represent cellular elements (e.g. genes, proteins, molecules, etc.) that share a connection provided they participate in the same pathway or are involved in similar functions.

The social and cellular network examples illustrate perfectly the utility of the network model. Outwardly, the systems represented by these models have little in common: one is concerned with social interactions among people while the other is concerned with electrostatic and chemical interactions among cellular components. However, from the point of view of the mathematical machinery used to analyze these networks, such differences are of little concern. Once a system has been described in terms of nodes and edges the same set of mathematical tools can be used to analyze the structure of the resulting network.

### **1.3 Network science applied to neural systems**

Recently, elements of network science have made their way into the neural sciences (Bullmore & Sporns 2009). Advances in non-invasive imaging, microscopy, and cellular recording methods have made it possible to observe neural systems at multiple spatial scales with, in some cases, sub-millisecond temporal resolution, and within a multitude of different organisms. Around these advances has sprung the field of “connectomics” (or, sometimes used interchangeably, “network neuroscience”) which is concerned not only with the technologies for acquiring neural data but also with analyzing and making sense of the petabytes of data that these techniques generate. In particular, connectomics embraces the inherent interconnectedness of neural systems (after all, at the microscopic scale neural systems are composed of neurons linked to one another by a mesh of axons and dendrites) and constructs for that system a network or graph describing its connectivity pattern (Rubinov & Sporns 2010).

### **1.4 Flavors of connectivity**

Broadly construed, biological neural networks can be divided into two classes according to how connectivity among neural elements is defined. Networks concerned with physical links among neural elements are referred to as “anatomical” or “structural” connectivity (SC) networks, and model synaptic connections among neurons at the micro-scale or the presence of myelinated fiber tracts among brain regions at the macro-scale. The other class of networks is concerned with statistical relationships between neural elements based on their activity and co-activity over time (Friston 2011). Networks of this type are sub-classified as “functional” or “effective” networks. Functional connectivity (FC) networks characterize the statistical dependency of elements’ neurobiological activity, often using an undirected measure such as correlation or coherence to quantify connectivity strength (Smith et al 2011). The undirectedness of these measures means that it is impossible to ascertain whether the activity of brain region  $x$  influences that of region  $y$  or whether it is the other way around. Effective connectivity networks, on the other hand, rely on temporal precedence (Seth 2010) or statistical models (Friston et al 2003) to infer directed or causal relationships between pairs of neural elements. Like structural networks, functional and effective connectivity networks can be estimated at multiple scales from spiking activity and local field potentials at the neuronal level to hemodynamic fluctuations at the macro-scale.

The focus of this dissertation is on human brain networks. Unlike the nervous systems of model organisms, which can sometimes be studied using invasive techniques, the human brain is usually imaged non-invasively with methods like electroencephalography (EEG), magnetoencephalography (MEG), or magnetic resonance imaging (MRI). EEG and MEG measure fast changes in electric and magnetic fields at the level of the scalp, which makes it

difficult to ascertain the precise location from which the signal originates (if the signal has a neuronal provenance, at all) (Nunez & Srinivasan 2006; Hämäläinen et al 1993). MRI methods, on the other hand, use fluctuating magnetic fields to excite atoms. From the atoms' responses, information such as tissue perfusion, blood volume, and oxygen concentration (ostensibly related to neuronal activity) can be measured. These measurements can then be used to estimate the presence of structural and functional connections between different parts of the brain (Basser et al 1994; Rogers et al 2007). This thesis focuses on networks constructed from MRI data, so it is worthwhile to briefly discuss the process of transforming MRI data into a format recognizable to a network scientist.

The field of cognitive neuroscience is awash in functional MRI (fMRI) studies purporting to show that the level of activity in specific brain regions or the extent to which different regions become coupled to one another can be manipulated by experimental condition. Such claims are made based on the premise that blood flow and neuronal activity are coupled to one another (Logothetis et al 2011). Using fMRI and recording how the hemodynamic signal changes over time in different parts of the brain, one can measure the activity of neuronal populations, albeit indirectly. In slightly more detail, sustained activity in a population of neurons requires oxygen, which is transported by hemoglobin in red blood cells. As a consequence, the area around active neurons will exhibit an excess of oxygen-rich blood shortly after the onset of activity. Blood that is oxygen-rich has different magnetic properties compared to blood that is oxygen-depleted, which makes it possible to distinguish between the two using the fMRI Blood-Oxygen-Level-Dependent (BOLD) contrast. To estimate connectivity from this signal, one can observe its temporal evolution, one can identify pairs of brain regions whose BOLD signals co-fluctuate (i.e.

are correlated with one another). The correlation coefficients for all pairs of brain regions can be arranged into a square correlation matrix such that no element is empty. In many cases, however, the correlation matrix is thresholded and binarized so that only a small subset of the strongest correlations coefficients is retained, rendering the full correlation matrix into a sparse adjacency matrix and making it amendable to graph-theoretic analysis. More recently, however, analysis tools have been developed that make it unnecessary to apply any threshold (Rubinov & Sporns 2011). It should be noted that there are number of available methods, besides correlations, for estimating the functional coupling between neural elements including coherence, partial correlations, covariance with regularization, information theoretic measures, and model-based estimates (Smith et al 2011). There are also important pre-processing steps that must be taken to ensure that the BOLD signal is not contaminated by head motion, respiratory, cardiovascular, or scanner artifacts. In addition, there are other pre-preprocessing steps that are more contentious including regression on global gray-matter signal and data censoring, which may improve the quality of the BOLD signal by reducing the motion artifacts (Power et al 2015), but may also remove neuro-biologically meaningful signal or induce spurious anti-correlations (Murphy et al 2009).

While fMRI is useful for generating estimates of brain functional connectivity, a second type of MRI scan known as diffusion weighted imaging can be used to reconstruct anatomical or structural brain networks (Hagmann et al 2007). Diffusion imaging models the motion of water molecules throughout the brain. In some areas, the motion appears to have no preferred diffusion direction – i.e. isotropic motion – whereas other areas show preferences for diffusion in one or more directions – i.e. anisotropic motion (Basser et al 2000; Mori 2002). One factor that

influences whether or not a water molecule's motion is anisotropic is the presence of myelinated axon bundles. Such bundles constrain the motion of water molecules so that they diffuse preferentially along the bundle's longitudinal axis. Thus, spatially contiguous groups of neural elements whose diffusion directions are aligned can be used to infer the presence of such bundles. To reconstruct networks from diffusion imaging data, one first estimates, for each neural element, its preferred direction(s) of motion. Next, pathways are reconstructed by integrating through the three-dimensional diffusion field. This entails planting millions of "seeds" throughout the brain's gray matter and moving the seed in small steps from its current location to a new location according to the direction of the diffusion field. This process, which traces trajectories or "streamlines" through the brain's white matter, is repeated until some termination criteria is reached or until the streamlines reaches gray matter. The presence of a gray matter-to-gray matter streamline is usually treated as evidence that those two points are anatomically connected to one another. Aggregating streamlines between all pairs of elements produces an element-by-element matrix that defines the brain's macro-scale anatomical connectivity network.

### **1.5 Empirical studies of brain connectivity**

Empirical studies of both functional and anatomical brain networks have provided insight into the large-scale organization of the human brain. Here I review some of these findings, beginning my discussion with FC, which is typically investigated using an experimental paradigm known as "the resting state" wherein subjects are scanned in the absence of any explicit neurocognitive task.



Network analyses of the resting brain have revealed a multitude of apparently non-random attributes, including a “small-world” architecture (Achard et al 2006), the presence of highly connected and highly central functional hub regions (Buckner et al 2009; Zuo et al 2012), a temporally flexible set of peripheral brain areas and a stable set of core regions (Bassett et al 2011), and a community structure of mutually-correlated regions (He et al 2009; Power et al 2011) that map onto many of the brain’s well-known functional systems (Smith et al 2009; Crossley et al 2013; Cole et al 2014). While these results are encouraging, they need to be qualified with several statements. First, these results were made by applying graph-theoretic measures to thresholded correlation matrices, which can only provide indirect evidence of a functional relationship between brain regions. Furthermore, correlation matrices have several peculiarities that may introduce systematic biases when they are interpreted as graphs. For example, Pearson’s correlation obeys a transitive property, and if connections AB and BC survive thresholding then the connection AC likely survives, as well. This leads to an overrepresentation of triangles in the thresholded matrix, which artificially inflates estimates graph measures like clustering and also influences the results of community detection (Zalesky et al 2012). Accounting for this bias requires comparison against an appropriate null model designed for correlation/covariance matrices (Hirschberger et al 2004), though in practice most studies compare against more popular (but perhaps inappropriate) null models (Maslov & Sneppen 2002). A second, more philosophical, issue is related to how FC is interpreted. In many cases, the connections in a thresholded FC matrix are accepted unconditionally, treated as though they were physical connections between brain regions and used to calculate path length and network efficiency (both of which number of steps from one node to another). This is certainly not the case, as functional connections, by definition, indicate statistical relationships only

(though the strength of a functional connection and the likelihood that an anatomical connection is present are related to one another; see Honey et al 2009). For this reason, it may be unwise to unconditionally accept the results of studies that rely heavily on this intuition, for example the hubs in Achard et al (2007) or the multi-step “paths” in Sepulcre et al (2012).

The other class of brain networks is anatomical or structural networks, which represent the physical wiring diagram of the human brain. Much like the plumbing of a building constrains the flow of water, the brain’s anatomical network helps constrain the flow of information between different brain regions and hence influences the extent to which those regions are functionally connected (Honey et al 2009; Deco et al 2010). Like FC, network analyses of SC uncover a number of non-random attributes. For example, SC networks have also been described as modular, though modules in this case refer to collections of brain regions with a high density of anatomical connections rather than functional connections (Bassett et al 2010; Betzel et al 2013; Sporns & Betzel 2015). Structural modules buffer flows over the network – the high density of within-module connections means that a signal can spread quickly from one brain region to another region in the same module while the lower density of between-module connections makes it difficult for that same signal to be passed to a different module.

SC networks also exhibit hub regions (Hagmann et al 2008; van den Heuvel & Sporns 2013). Whereas modules act to segregate brain areas from one another, hubs confer massive integrative capacity, forming links across module boundaries and exercising simultaneous control over and receiving input from a multitude of other brain regions. Empirical studies have found that hubs may differ in their integrative roles. Middle-posterior hubs appear to act as “connectors,”

forming links to many modules and representing conduits through which information is exchanged across hemispheres. Hubs located in either hemisphere appear to have more autonomy and function as “provincial” hubs, concentrating their links to a limited number of modules and controlling local information flow. The brain’s hubs themselves are densely interconnected and form “rich clubs” and cores of different sizes and scales (van den Heuvel & Sporns 2013). Rich club architecture confers further integrative capacity by making it possible for hub regions to share information among one another. Also like FC networks, SC networks are thought to be “small-world” and exhibit long-distance shortcuts, which allow for rapid interregional communication.

One of the most interesting features of SC networks is their apparent cost-effectiveness (Bassett et al 2010; Bullmore & Sporns 2012). Cost, in terms of brain networks, is typically operationalized to mean the total wiring length – i.e. the sum of the length of all connections. Connection length is a natural proxy for the cost of a network, as longer connections require more cellular material to build as well as more energy to sustain. Networks composed of many long-distance connections are more costly by this measure than, say, a network composed strictly of short-range connections. On the other hand, many of the hallmark features of SC networks, including hubs, long-distance shortcuts, and rich clubs, involve, to some extent, high-cost (i.e. long-distance connections). So a strict minimization of cost, which would entail forming connections between brain regions that are near one another, which would result in a network in which these features would be conspicuously absent. Therefore it is often said that real-world SC networks tradeoff between the formation of adaptive networks features and total cost (Kaiser & Hilgetag 2006; Avena-Koenigsber et al 2014).

## **1.6 Summary of research contributions**

The rest of this thesis is divided into three chapters. Each is self-contained and represents either a completed (peer-reviewed and published) paper or a paper currently in some stage of the review process. The first chapter is the most general, and contains a description of age-related changes in brain structural and functional networks. The focus of this chapter is on how functional changes relate to intrinsic connectivity networks (ICNs) and how the structure-function relationship is modulated with age. We find that ICNs become more integrated with age, suggesting a loss of specificity. Additionally, we find that hub regions become less efficiently connected to the rest of the brain (compared to non-hub regions) and that the functional connectivity of regions connected by longer anatomical paths increases with age. The second chapter deals with the topic of community detection, again in the context of functional brain networks and age-related change. We show that community detection decomposes brain networks into recognizable communities/modules and that the module composition and the segregation of modules from one another follow characteristic trajectories across the lifespan, though this trajectory depends upon the scale at which the modules are defined (i.e. whether we consider larger or smaller modules). We also show that these changes are driven by specific modules; at a coarse scale the task-positive modules shows increased segregation while at fine scales modules consisting of parahippocampal, retrosplenial, and posterior cingulate cortices become less segregated. The third and final chapter deals with the topic of network generative models for the human connectome. In this chapter we propose a flexible modeling framework for generating synthetic connectome data that allows for testing and comparing any number of wiring rules. We go on to test a set of possible wiring rules, including preferential attachment,

assortative mixing, homophily, and geometric models, and find that homophily-based wiring rules outperform all other models that we tested by generating synthetic structural networks that embody many of the properties found in real-world structural networks. Finally, we apply these models to lifespan data and show that parameters governing the role of spatial constraints weaken with age, as does the overall ability to reproduce connectome data. This suggests that later in life the organization of the connectome is incompletely captured by the dual-factor homophily and geometry model, and that, perhaps, additional constraints or a variant of the current wiring rule might do a better job.

## **CHAPTER 2: CHANGES IN STRUCTURAL AND FUNCTIONAL CONNECTIVITY AMONG RESTING-STATE NETWORKS ACROSS THE HUMAN LIFESPAN**

This chapter attempts to address the following questions:

- What aspects of brain network architecture change with age?
- Which functional connections strengthen/weaken across the lifespan and how are these connections related to the brain's functional systems (i.e. ICNs).
- Structural networks are thought to constrain functional patterns: are there age-related changes in brain structure that could explain the changes in function?

Adapted from the paper:

Betzel RF, Byrge L, He Y, Goñi J, Zuo XN, Sporns O (2014). Changes in structural and functional connectivity among resting-state networks across the human lifespan. *Neuroimage*, 102(2), 345-357.

Abstract: At rest, the brain's sensorimotor and higher cognitive systems engage in organized patterns of correlated activity forming resting-state networks. An important empirical question is how functional connectivity and structural connectivity within and between resting-state networks change with age. In this study we use network modeling techniques to identify significant changes in network organization across the human lifespan. The results of this study demonstrate that whole-brain functional and structural connectivity both exhibit reorganization with age. On average, functional connections within resting-state networks weaken in magnitude while connections between resting-state networks tend to increase. These changes can be localized to a small subset of functional connections that exhibit systematic changes across the lifespan. Collectively, changes in functional connectivity are also manifest at a system-wide

level, as components of the control, default mode, saliency/ventral attention, dorsal attention, and visual networks become less functionally cohesive, as evidenced by decreased component modularity. Paralleling this functional reorganization is a decrease in the density and weight of anatomical white-matter connections. Hub regions are particularly affected by these changes, and the capacity of those regions to communicate with other regions exhibits a lifelong pattern of decline. Finally, the relationship between functional connectivity and structural connectivity also appears to change with age; functional connectivity along multi-step structural paths tends to be stronger in older subjects than in younger subjects. Overall, our analysis points to age-related changes in inter-regional communication unfolding within and between resting-state networks.

## 2.1 Introduction

The brain is a complex system that can be conceptualized as a network of anatomically linked regions and thereby made amenable to analysis using tools from graph theory (Bullmore & Sporns 2009; Rubinov & Sporns 2010; Sporns 2014). The brain's structural connectivity (SC), together with other factors, contributes to shape neurophysiological activity, and thereby influences functional connectivity (FC) among neuronal populations (Wang et al 2013) and brain regions (Honey et al 2009; Deco et al 2011). Whereas SC refers to physical connections between two brain regions, FC is defined as the statistical dependency – e.g. correlation, coherence, mutual information, etc. – between those regions' activity time courses. Graph theoretical analyses of SC/FC networks have revealed a host of non-random attributes, including small-worldness (Achard & Bullmore 2006; Gong et al 2009), hubs and cores (Achard et al 2006; Hagmann et al 2008; Zuo et al 2012), a structural rich club (van den Heuvel & Sporns 2011), modular architecture (Meunier et al 2009; Meunier et al 2010), and economic wiring (Basset et al 2010; Bullmore & Sporns 2012), among others.

Resting brain FC can be decomposed into resting-state networks (RSNs) composed of brain regions that exhibit coherent activity in a task-free state (Buckner et al 2013), exhibit consistent spatial topographic patterns across the cerebral cortex (Yeo et al 2011; Power et al 2011), and strongly resemble collections of brain regions corresponding to task-evoked sensory, motor and higher-order cognitive systems (Smith et al 2009; Crossley et al 2013). RSNs can be extracted using different methodologies, including independent component analysis (ICA; Beckmann et al 2005) and clustering approaches applied to whole-brain FC networks (e.g., Bellec et al 2010; Yeo et al 2011; Power et al 2011). A number of recent studies have focused on changes in



connectivity within and between RSNs, both on fast time scales in the course of spontaneous brain dynamics (Allen et al 2014; see Hutchison et al 2013 for a systematic review), as well as in the course of visual perceptual learning (Lewis et al 2009), acquisition of motor skills (Ma et al 2011) and cognitive practice (Jolles et al 2013).

This report aims to characterize changes in the pattern of SC/FC over the course of the human lifespan, with a focus on connectivity changes within and between RSNs. A number of previous studies have shown that patterns of SC/FC undergo characteristic changes over developmental stages and aging (Zuo et al 2010; Wang et al 2012; Cao et al 2014; Yang et al 2014). In childhood, FC is dominated by short-range local links, which are gradually replaced by long-distance functional connections in adulthood, forming mature RSNs (Fair et al 2009; Kelly et al 2009; Supekar et al 2010; Power et al 2010). In contrast, aging studies have demonstrated the opposite effect, with RSNs exhibiting decreased FC (Andrews-Hanna et al 2007; Ferreira and Busatto 2013; Geerligs et al 2014). Studies of SC across the lifespan have demonstrated that hub regions and modules are present by early childhood, though changes of cortical white-matter connectivity continues across the lifespan (Gong et al 2009; Hagmann et al 2010; Lim et al 2013).

While these studies and others have provided insight into the development and maturation of specific RSNs (e.g. Fair et al (2007 2008, and 2009) for control networks and Andrews-Hanna et al (2007) for the default mode and dorsal attention networks), few reports have examined age-related changes in connectivity at the whole-brain level across the entire lifespan. Moreover, studies that focus on the intrinsic connectivity of a specific RSN necessarily overlook any

connections that that RSN makes to the rest of the brain and how these connections change as a function of age. Here, we aim to bridge this particular gap in knowledge by tracking the age-related change in all functional and structural connections in the human brain over the course of the lifespan. Because RSNs are thought to correspond to the brain's functional systems, it was of particular interest to observe how these changes were related to the boundaries of RSNs and their distributed subcomponents. An additional aim was to gain insight into how changes in SC and FC might be interrelated, and what these changes might reveal about age-related changes in interregional communication.

## **2.2 Methods and Materials**

### *2.2.1 NKI-RS Lifespan Sample and Image Preprocessing*

Lifespan data used in this study are part of the publically available NKI-Rockland sample ([http://fcon\\_1000.projects.nitrc.org/indi/pro/nki.html](http://fcon_1000.projects.nitrc.org/indi/pro/nki.html)) from the Nathan Kline Institute (NKI, NY, USA) consisting of  $N = 126$  subjects (58 female) over the age range 7-85 years (median age = 31.5). The study was approved by the NKI institutional review board and all adult and child subjects provided informed consent (Nooner et al 2012).

Subjects in this study underwent a scan session using a Siemens TrioTM 3.0 Tesla MRI scanner. Resting fMRI scans were collected using an echo-planar imaging (EPI) sequence with the following parameters: time repetition (TR)/ time echo (TE) = 2500/30 ms, flip angle (FA)=80°, field of view (FOV) = 216×216 mm<sup>2</sup>, voxel size = 3.0×3.0×3.0 mm<sup>2</sup>, distance factor = 10%, number of slices = 38. Each scan session was 650 s long and comprised 260 functional volumes. Inside the scanner, subjects received instructions to keep their eyes closed, relax their minds, and

to not move. T1-weighted images were acquired using the following magnetization-prepared rapid gradient echo (MPRAGE) sequence: TR/TE = 2500/30 ms, inversion time = 1200 ms, FA = 8°, FOV = 256×256 mm<sup>2</sup>, voxel size = 1.0×1.0×1.0 mm<sup>3</sup>, number of slices = 192. T1-weighted images were subsequently used for spatial normalization and group-specific template generation.

This sample has been used in two recent studies on the human brain functional connectivity changes across the lifespan (Yang et al 2014; Cao et al 2014). The Connectome Computation System (CCS: <http://lfcd.psych.ac.cn/ccs.html>) was used to preprocess both R-fMRI and DTI images for subsequent analyses. As in Cao et al (2014), preprocessing of functional images included discarding first four EPI volumes to allow for the signal to reach equilibrium, correction for timing offsets, 3D geometrical displacement correction for head motion, and 4D global mean-based intensity correction. Motion correction was performed using the Friston-24 model, which regresses out nuisance parameters including six head motion parameters, those same parameters at the previous time step, and both sets of parameters squared (Friston et al 1996). Additionally, global mean, white matter, and cerebrospinal fluid signals were also included as nuisance parameters and regressed out. Lastly, the signal was band-pass filtered (0.01 – 0.1 Hz) and both linear and quadratic trends removed.

The preprocessing steps of DTI images are identical to those used in an earlier study (van den Heuvel and Sporns 2011). Specifically, DTI images were corrected for eddy-current distortions and realigned to the mean image of the 12 unweighted B0 images (Andersson and Skare 2002). Using the corrected DTI data, a tensor was fit to the diffusion profile within each voxel and the

diffusion direction within each voxel was assigned as the principal eigenvector of the tensor by computing its eigen-system (Chang et al 2005). To provide information on the diffusion direction within a given voxel, its fractional anisotropy (FA) was computed as the square root of the sum of squares (SRSS) of the diffusivity differences, divided by the SRSS of the diffusivities. Using the information on preferred diffusion direction with each voxel in the whole brain mask, the white matter tracts were reconstructed with FACT (fiber assignment by continuous tracking) algorithm (Mori et al 1999; Mori and van Zijl 2002). Specifically, within each voxel, evenly distributed 32 seeds were used as starting points of possible streamlines, which generate the white matter fibers by following the preferred diffusion direction from voxel to voxel. A threshold on FA of 0.1 or a sharp turn of  $> 45^\circ$  were set to stop tracking a fiber streamline at a voxel.

### *2.2.2 Construction of FC networks*

In order to address questions related to RSNs, we used a previously established functional parcellation of the human cerebral cortex (Yeo et al 2011). This particular parcellation was derived by clustering the whole-brain functional connectivity networks of 500 subjects (along with a 500 subject replication cohort) according to the similarity of regions' functional connectivity profiles. This procedure resulted in seven clusters, whose boundaries shared a close correspondence to the known topographic boundaries of visual (Vis) and somatomotor (SomMot) networks, limbic regions (Limbic) and distributed association networks for executive control (Cont), attention (DorsAttn, SalVentAttn), and internally-directed cognition (Default). These seven RSNs displayed hierarchical organization such that each of the seven clusters could be subdivided into components with distinct patterns of FC, resulting in a total of 17 RSN

components or sub-networks: VisCent, VisPeri, SomMotA, SomMotB, LimbicA, LimbicB, ContA, ContB, ContC, DorsAttnA, DorsAttnB, SalVentAttnA, SalVentAttnB, DefaultA, DefaultB, DefaultC, and DefaultD. Across all the 17 sub-networks, there are in total  $n = 114$  separated anatomical regions of interest (ROIs). Specifically, any of the ROIs meets two basic requirements: 1) it is isolated anatomically from other regions within the sub-network it belongs to, and 2) is separated by the network boundaries from regions within other sub-networks. These ROIs were then used to represent nodes in both FC and SC networks. The functional connection between nodes  $i$  and  $j$  was defined as the Fisher-z transformed Pearson product-moment correlation of the representative BOLD time series recorded at those nodes. In the standard surface space defined by FreeSurfer (i.e., *fsaverage5*), representative time series were computed as the average time series of all voxels within an ROI extracted from the transformed individual preprocessed R-fMRI data on the *fsaverage5* surfaces (Jiang et al 2014). For each subject, FC between all pairs was organized into an  $n \times n$  weighted and signed correlation matrix,  $A^{FC}$ , whose elements  $a_{ij}^{FC}$  denoted the FC between nodes  $i$  and  $j$ . It is common practice to sparsify  $A^{FC}$  by retaining only a fraction of the strongest connections or entries that survive a threshold for statistical significance (Achard & Bullmore 2007; Cao et al 2014). In this study FC networks were not sparsified. Eliminating connections impairs our ability to assess how FC changes with age – removing a connection from some subjects but not from others results in fewer observations and a reduction in statistical power. A group-averaged FC matrix (for visualization only) representing all subjects is shown in Figure 2.2A.

### 2.2.3 Construction of SC networks

SC was measured between the same  $n = 114$  cortical ROIs used to define nodes in FC networks. Deterministic fiber tracking was performed as in previous work (van den Heuvel and Sporns 2011) except that 32 seeds were started in each voxel. The fiber tracking procedure yielded matrices  $NF_{ij}$  and  $FA_{ij}$  whose elements represented the number of reconstructed fibers connecting nodes  $i$  and  $j$  and the average fractional anisotropy of completed fiber tracts, respectively. We considered nodes  $i$  and  $j$  to be adjacent if they were connected by at least one fiber tract. For each subject, the full set of connected nodes was encoded in a binary adjacency matrix,  $A^{bin}$ , whose elements  $a_{ij}^{bin}$  were equal to 1 if  $i$  and  $j$  were connected and zero, otherwise. Each pair of connected nodes was also assigned a weight based on  $NF_{ij}$  and  $FA_{ij}$ . The set of connection weights were stored in the matrix,  $A^{wei}$  and were calculated according to the expression:

$$a_{ij}^{wei} = FA_{ij} \times NF_{ij}^{\gamma}$$

where  $\gamma$  acts like a soft threshold on the matrix  $NF_{ij}$  (Schwarz & McGoñigle 2011; Zhang & Horvath 2005; Lohse et al 2013). Only when  $\gamma = 0$ , the elements of  $NF_{ij}^{\gamma}$  become binary variables and edge weights  $a_{ij}^{wei} = FA_{ij}$ . For  $\gamma > 0$ , the elements of  $NF_{ij}$  contribute to determining the weight of structural connections. In this manuscript we explored eleven possible values of  $\gamma$  equally spaced over the interval  $[0, 2]$ . The lower bound was selected because  $\gamma < 0$  tends to reward nodes connected by a smaller number of fibers with a stronger edge weight. The upper bound was selected because for  $\gamma > 2$ , the resulting SC matrix tends to be dominated by one or two strong edges. Both of these particular regimes seem biologically unrealistic. A group-averaged SC matrix evaluated at  $\gamma = 0.6$  is shown in Figure 2.2B. We would like to note that we

explored other schemes for assigning the weight of a structural connection including some that incorporate a correction based on ROI size (e.g. by dividing  $a_{ij}^{wei}$  by  $V_i + V_j$ , where  $V_i$  is the size, in number of voxels, of region  $i$ ). In general, our results are robust to size-corrected weighting schemes. Consequently, all subsequent analyses were performed on SC matrices,  $A^{wei}$ , where the edge weights were uncorrected for ROI size.

#### 2.2.4 Multiple linear regression analysis

In general, we were interested in how some variable,  $y$ , which might represent the magnitude of a connection weight or the value of some graph-theoretic measurement, changes over the lifespan. Typically  $y$  is defined for all subjects such that we can create a  $[N \times 1]$  vector of those values, which we denote  $\mathbf{y}$ . To model  $y$  over the lifespan, we made use of multiple linear regression models (MLR), which have the standard form:

$$\hat{\mathbf{y}} = \mathbf{X} \cdot \boldsymbol{\beta}_{\mathbf{X}} + \mathbf{G} \cdot \boldsymbol{\beta}_{\mathbf{G}} + \mathbf{e}$$

Here,  $\hat{\mathbf{y}}$  is an  $[N \times 1]$  vector of estimations of  $y$ , the variable of interest,  $\mathbf{X}$  is the design matrix with associated parameters  $\boldsymbol{\beta}_{\mathbf{X}}$ ,  $\mathbf{G}$  is an  $[N \times 3]$  matrix of nuisance variables (gender, total intracranial volume, and mean frame-wise displacement) with the associated  $[3 \times 1]$  vector of nuisance parameters  $\boldsymbol{\beta}_{\mathbf{G}}$ , and  $\mathbf{e}$  is an  $[N \times 1]$  vector of error terms. The size of  $\mathbf{X}$  and  $\boldsymbol{\beta}_{\mathbf{X}}$  was dependent on the choice of design matrix, of which we explored two possibilities, corresponding to linear and quadratic models, respectively:

$$\mathbf{X}_{[N \times 2]} = \begin{bmatrix} 1 & age_1 \\ \vdots & \vdots \\ 1 & age_N \end{bmatrix} \text{ with } \boldsymbol{\beta}_X = [\beta_0 \quad \beta_1]$$

$$\mathbf{X}_{[N \times 3]} = \begin{bmatrix} 1 & age_1 & age_1^2 \\ \vdots & \vdots & \vdots \\ 1 & age_N & age_N^2 \end{bmatrix} \text{ with } \boldsymbol{\beta}_X = [\beta_0 \quad \beta_1 \quad \beta_2]$$

The model that best described the lifespan trajectory of  $\mathbf{y}$  was selected as the one with a smaller Akaike information criterion (AIC) value, representing a tradeoff between model likelihood and complexity.

The parameters  $\boldsymbol{\beta}_X$  were used to ascertain whether or not a model exhibited a statistically significant age effect. One-sample  $t$ -tests were performed on the  $\beta$  associated with the highest order age term ( $\beta_1$  if the model is linear;  $\beta_2$  if the model is quadratic). A model was said to exhibit a statistically significant age effect if the  $p$ -value associated with that test was smaller than a critical value,  $p_{crit}$ . In general,  $p_{crit} = 0.01$ . In the cases where it was necessary to correct for multiple comparisons,  $p_{crit}$  was adjusted using the linear step-up procedure for controlling the false discovery rate (FDR;  $q < 0.01$ ) (Benjamini & Hochberg, 1995).

It should be noted that the nuisance variable “mean frame-wise displacement” was estimated based on subjects’ motion during the resting fMRI scan. While the effect of motion on FC has been well-documented (see Power et al 2012) potential effects subject motion on diffusion-weighted images and tractography algorithms is less understood. Consequently, it is unclear whether it is appropriate to include the motion parameter as a nuisance variable in a MLR model. Therefore, in all cases where MLRs were fit to SC data, we tried models that included framewise



displacement as a nuisance variable as well as models that excluded it. All results reported in subsequent sections are independent of this decision.

### 2.2.5 FC edge trajectories

The first series of analyses focused on characterizing age-related changes in FC. To assess whether there were global trends in FC across the lifespan, we separately modeled the average FC within and between RSN components using MLRs. To further quantify age-related change at a finer scale, MLRs were also fit to the functional connections between every pair of nodes,  $i$  and  $j$ .

### 2.2.6 FC modularity analysis

In addition to modeling edge-level changes in FC, we also analyzed system-level properties of FC networks using tools from graph theory. Of particular interest was whether the cohesiveness of RSNs changed over the lifespan. Cohesiveness, in this case, refers to a high magnitude of internal FC and weak external FC. This conceptualization of cohesiveness is consistent with the definition of the graph-theoretic measure, “modularity.” Modularity quantifies the extent to which a network can be decomposed into internally integrated, yet globally segregated communities (Newman 2006). For weighted and signed networks like FC, modularity can be calculated as  $Q^* = \sum_c q_c^*$ , where  $q_c^*$  is the contribution to  $Q^*$  by a community  $c$  and is defined as:

$$q_c^* = \frac{1}{m^+} \sum_{ij \in c} \left[ a_{ij}^+ - \frac{s_i^+ s_j^+}{2m^+} \right] - \frac{1}{m^+ + m^-} \sum_{ij \in c} \left[ a_{ij}^- - \frac{s_i^- s_j^-}{2m^-} \right]$$

In this expression,  $a_{ij}^{\pm}$  contains either the positive or negative edge weights of  $a_{ij}^{FC}$ . The variables  $m^{\pm} = \frac{1}{2} \sum_{ij} a_{ij}^{\pm}$  and  $s_i^{\pm} = \sum_j a_{ij}^{\pm}$  are the signed weight of the entire network and node strength, respectively (Rubinov & Sporns 2011). Each RSN was regarded as a community, and its modularity contribution,  $q_{RSN}^*$ , was calculated. In order to quantify changes in the modularity of RSN components across the human lifespan, MLRs were fit to the lifespan trajectory of each of the 17 RSN components' modularity contributions,  $q_{RSN}^*$ , according to the procedure described earlier.

### 2.2.7 SC measures and hubs

We characterized SC matrices with three variables: the total number of binary connections,  $m = \frac{1}{2} \sum_{ij} a_{ij}^{bin}$ ; the total number of streamlines,  $nf = \frac{1}{2} \sum_{ij} NF_{ij}$ ; and the average FA of all edges,  $fa = \frac{1}{2m} \sum_{ij} FA_{ij}$ .

We also identified highly connected, highly central hub regions following an analysis of both binary and weighted versions of SC networks. Analysis of binary networks consisted of measuring each node's total number of connections (degree),  $k_i = \sum_j a_{ij}^{bin}$ , and each node's local efficiency,  $e_i = \frac{1}{n-1} \sum_{j \neq i} d_{ij}^{-1}$ , where  $d_{ij}$  is the length of the shortest path connecting nodes  $i$  and  $j$ . Analysis of weighted networks consisted of several node-wise measures, including node strength,  $s_i = \sum_j a_{ij}^{wei}$  and betweenness centrality,  $b_i$ , which measures the number of shortest paths traversing a given node.

We defined a region’s “hubness” as its average rank across node degree ( $k_i$ ), node strength ( $s_i$ ), nodal efficiency ( $e_i$ ), and betweenness centrality ( $b_i$ ), estimated from each participant’s SC matrices and averaged across all participants. Hubs were defined as the regions with the top-ranked aggregate hub scores. We chose this composite definition of hubness based on the fact that no single metric unambiguously qualifies a node as a hub – e.g. a high degree node may form only weak connections (low strength) or have small betweenness centrality. By assigning each node a composite hub score based on many different measures, we ensure that the nodes we label as hubs score high across several different graph metrics.

#### *2.2.8 Path efficiency framework*

SC networks enable distant brain regions to communicate with one another, and hence an important question concerns the effect of age on communication efficiency. To address this question, we defined a measure of path efficiency that could be quantified for every pair of nodes, and then modeled its trajectory across the lifespan. The path efficiency between nodes  $i$  and  $j$  is closely related to the total weight of the shortest weighted path connecting those nodes. Intuitively, if the shortest path involves few steps and is comprised of edges with large weights, then the efficiency of that shortest path should be large. Conversely, shortest weighted paths that involve many steps and weak edges are, intuitively, less efficient. This notion of efficiency is captured by first transforming edge weights from measuring the strength of association to measuring distance, which was accomplished by the simple inversion,  $\frac{1}{a_{ij}^{wei}}$ , which ensures that nodes connected by strong edges are “closer” to one another than nodes connected by weak edges. Following this inversion, the total weight of the shortest path was calculated using Dijkstra’s algorithm (Dijkstra, 1959). Calculating the shortest weighted path between every pair

of nodes defines two matrices,  $D^{wei}$  and  $D^{steps}$ , whose elements  $d_{ij}^{wei}$  and  $d_{ij}^{steps}$  were equal to the total weight of the shortest weighted path and the length (in discrete steps) of that path, respectively. Finally, to convert weight into efficiency,  $D^{wei}$  was inverted in an element-wise fashion and transformed into the efficiency matrix,  $E^{wei}$ , whose elements were equal to  $e_{ij}^{wei} = \frac{1}{d_{ij}^{wei}}$  (Latora & Marchiori 2001). Thus, the elements of  $E^{wei}$  represent the efficiencies of the shortest weighted path between any two nodes. In order to quantify changes in efficiency across the human lifespan, the trajectory of path efficiency between each pair of nodes was modeled using the same MLRs procedure described earlier but without mean frame-wise displacement included as a nuisance variable.

### 2.2.9 FC distance dependence

The final analysis of SC builds on the previous section. We hypothesized that changes in the topology of SC over the lifespan would have an impact on the capacity of SC for routing information, a change that might be manifested in FC. For example, nodes that early in life had been connected by efficient paths comprising few processing steps and strong edges may rely on less efficient, multi-step communication strategies later in life. To address whether the length of shortest paths influenced FC and whether this relationship changed over the lifespan, we examined the matrices,  $D^{steps}$ , which measured the number of steps in the shortest weighted paths connecting all pairs of nodes. For each subject, we computed the average FC of edges connected by  $d_{ij}^{steps} = 1, 2, 3, \dots$ . Then, for each number of steps we asked how the average FC at that distance was correlated with age across all subjects. This analysis, along with the other analyses of structural connectivity, was carried out at all levels of  $\gamma$ .

All analyses were run in Matlab (The Mathworks, Inc. - Natick, MA, USA). Graph theoretical analysis was performed using custom software as well as software made available as part of the Brain Connectivity Toolbox (<https://sites.google.com/site/bctnet/>; Rubinov & Sporns 2010).

## 2.3 Results

### 2.3.1 FC decreases within RSNs and tends to increase between RSNs

MLRs were fit to the average FC within and between RSN components, which revealed that, on average, FC within RSNs decreased with age, while the opposite was true of FC between RSNs. Both models were statistically significant ( $p < 0.01$ , uncorrected) (Figure 2.3). This figure suggests that, on average, functional connections within RSNs follow decreasing trajectories with age while connections between RSNs increase in magnitude. An important question is whether these changes are driven by specific functional connections/RSNs.

In order to assess whether FC between specific regions (nodes) exhibited age-related change, MLRs were fit to lifespan trajectories of the  $n_c = \frac{114 \times 113}{2} = 6441$  functional connections. This analysis revealed 85 functional connections that exhibited statistically significant age-related change, representing 1.3% of all possible edges comparisons ( $q < 0.01$ , FDR-corrected; corresponding to an uncorrected  $p = 1.3 \times 10^{-4}$ ) (Figure 2.4). These edges involved only 60 of the possible 114 cortical regions (nodes) and represented 15 of the 17 RSN components (DefaultC and LimbicB were not represented).-The interregional distances of the 85 statistically significant edges ranged from 9 mm to 130 mm. To assess whether interregional distance was systematically related to the likelihood of an edge exhibiting a statistically significant age effect, we calculated the Spearman correlation of interregional distance with the corresponding  $p$ -value.

We performed this calculation with all edges grouped together and for linear and quadratic models separately. If there was a bias towards either long- or short-range connections exhibiting an age-related effect, we would expect this correlation to be non-zero. In all cases, we found no clear relationship of  $p$ -value to interregional distance:  $r_{all} = 0.0068$ ,  $r_{linear} = -0.03$ ,  $r_{quadratic} = 0.058$ . Figures 2.5A and 2.5B depict FC versus age trajectories for select edges within and between RSN components, respectively.

Of the 85 connections exhibiting statistically significant age effects, 22 connected nodes that belonged to the same RSN component. Ten of these connections exhibited lifespan trajectories that were best described by linear decreases with respect to age and included regions representing ContC (precuneus, posterior cingulate), DefaultB (anterior temporal lobe, dorsal prefrontal, inferior parietal lobule), ContA (lateral prefrontal, anterior cingulate), VisPeri (inferior extrastriate), and SalVentAttnB (medial posterior prefrontal). The ten linearly decreasing functional connections were positively coupled early in life and included edges that were among the strongest in the entire network, with mean FC at age 7 of  $0.69 \pm 0.44$ . With age, FC between these regions is predicted to become less positive, with a mean change in FC from age 7 to 85 of  $-0.37 \pm 0.05$ . Because these connections were initially very strong, this decrease in FC magnitude served only to make them less strong, rather than weaken them to the point that their FC approached zero.

The lifespan trajectories of the remaining twelve within-component connections were best fit by convex quadratic models and involved regions from SalVentAttnA (ventral pre-central, insular, medial parietal, medial frontal), VisCent (striate), and SomMotB (insula, secondary

somatosensory). FC of these edges was of modest magnitude early in life (mean FC of  $0.36 \pm 0.19$  at age 7), but doubles by the time they reach their respective peaks (mean peak FC of  $0.74 \pm 0.19$ ; mean peak age of  $40.9 \pm 5.4$  years, where peak age was computed as  $\frac{-\beta_1}{2\beta_2}$ ). At age 85 the average FC of these edges decreases to a magnitude less than the magnitude of FC at age 7, (mean FC at age 85 is  $0.18 \pm 0.13$ ), meaning that on average, these regions exhibit decreased FC over the entire lifespan.

The remaining 63 edges fell between RSN components. Among the models describing these edges 9 were linear-decreasing, 19 were linear-increasing, 19 were quadratic-convex, and 16 were quadratic-concave. These models were more variable in terms of their predictions for FC changes across the lifespan (36 predict increases; 26 predict decreases), though the net change in FC from age 7 to 85 was  $0.07 \pm 0.24$ .

### *2.3.2 RSNs modularity decreases with age*

The results of the previous section addressed questions about how the magnitude of specific functional connections changed over the course of the entire lifespan. We also assessed system-level change by calculating each RSN component's modularity,  $q_{RSN}^*$ , and modeling its change with age. Of the 17 RSN components, five exhibited statistically significant age-related changes ( $q < 0.01$ , FDR-corrected; corresponding to an uncorrected  $p = 1.2 \times 10^{-3}$ ): ContA, ContC, DorAttnA, SalVentAttnA, and VisPeri (Figure 2.5). Of those five, all but SalVentAttnA were linear, and all predicted a net decrease in modularity over the entire lifespan (Figure 2.6).

### *2.3.3 Structural changes across the lifespan*

In addition to quantifying FC changes over the lifespan, we were also interested in assessing whether SC changed as well. As a coarse measure of change, we first measured the total number of connections,  $m$ , the total fiber count,  $nf$ , and the average FA of fibers,  $fa$ , and modeled their trajectories across the lifespan. Both  $m$  and  $nf$  exhibited statistically significant linear decreases with age ( $p < 0.01$ , uncorrected) (Figures 2.7A, 2.7B). The variable  $fa$  exhibited a more complicated trajectory, exhibiting a sharp rise from early childhood into adulthood followed by a protracted decrease (Figure 2.7C). This trajectory could not be modeled accurately using either a linear or quadratic model.

#### *2.3.4 Communication capacity decreases in proportion to “hubness”*

We next identified a set of hub regions according to a composite score based on their degree ( $k_i$ ), strength ( $s_i$ ), nodal efficiency ( $e_i$ ), and betweenness centrality ( $b_i$ ). Hubs were consistent across age and levels of  $\gamma$  (Figure 2.9) and were located bilaterally in extra-striate cortex and in the posterior cingulate, which agree with structural core regions in the posterior-medial cortex reported by Hagmann et al (2008) and the high-centrality regions reported by Zuo et al (2012). Other hub regions included the insula, the primary somatomotor cortex, the lateral/ventral prefrontal, and post-central cortices (Figure 2.8A). See Figure 2.14 for a topographic representation of hub scores mapped to the cortical surface.

An important question was whether SC changes across the lifespan would predict increases or decreases in the capacity for communication between brain regions. To address this question, we computed the efficiency of the shortest weighted path connecting every pair of nodes and modeled its trajectory across the lifespan. We found that path efficiency between a large number



of nodes decreased with age. Interestingly, the distribution of statistically significant decreases in path efficiency was not equally distributed, with a small subset of nodes participating in a disproportionate number of statistically significant models ( $q < 0.01$ , FDR-corrected; corresponding to an uncorrected  $p = 2.8 \times 10^{-3}$ ). Interestingly, the number of statistically significant models that a node participated in was correlated with its “hubness” (Figure 2.8B), a relationship that was consistent across the  $\gamma$  values tested in this paper (Figure 2.10). Because almost all statistically significant models represent decreases in path efficiency, the more statistically significant models a region is involved in, the less efficient that region’s connectivity to the rest of the network becomes. This result suggests that a region’s “hubness” is a good predictor of whether that region’s communication efficiency becomes compromised with age. These findings were robust with respect to alternative edge-weighting schemes such as those that correct edge weights for ROI size (Figures 2.11 and 2.12) and were also independent of whether we use more traditional measures to define hubness (i.e. when defining hubness based on node degree, strength, betweenness, or local efficiency, alone) (Figure 2.13).

### *2.3.5 Magnitude of age×FC correlation is dependent upon topological distance*

The final analysis consisted of assessing whether the numbers of steps separating two nodes in SC was related to the effect of age on FC between those nodes. These results revealed that when nodes are directly connected to one another, their FC is only weakly correlated with age (Figure 2.8C). That is, nodes that maintain direct structural connections, on average, also maintain a relatively constant level of FC across the lifespan. As the number of steps increases, however, the correlation between FC and age increases in magnitude. This suggests that with age, FC along multi-step paths becomes stronger, a trend that continues up to a path length of around 4 or

5 steps, partly dependent upon the exact value of  $\gamma$ . This indicates that nodes that are indirectly connected structurally tend to exhibit functional connections that grow stronger over the human lifespan.

## **2.4 Discussion**

In this study, we examined changes in functional connectivity and structural connectivity within and between resting-state networks across the human lifespan. Our results indicated that FC within RSNs decreased with age, affecting higher order control and attention networks, visual and somatomotor networks, as well as the default mode network. On the other hand, FC tended to increase between RSNs, especially among components of the dorsal attention network, the saliency/ventral attention networks and the somatomotor network. These results were supported by an additional finding suggesting that the modularity of RSN components comprising control, attentional, limbic, and visual networks decreases with age. Other RSNs, including components of the default mode, also exhibited decreased modularity, but failed to pass a statistical threshold for significance. The density of anatomical connections and the total number of fiber tracts decreased with age, which has the effect of increasing the topological distance and thus decreasing the efficiency of paths between pairs of nodes. Hub regions were affected the most by the decreased number of connections, exhibiting statistically significant decreases in path efficiency with many other regions. Finally, we also observed that the relationship between age and FC depended on path length, a measure derived from SC. For directly connected pairs of nodes, the correlation between age and FC was weakly positive. With greater path length, the magnitude of this correlation progressively increased. Our results suggest anatomically specific and inter-related patterns of change in FC and SC both within and between RSNs, with a decline

in the density of structural connections, particularly at hub nodes, that is associated with a loss of RSN component modularity.

#### *2.4.1 Lifespan Changes in Functional Connectivity*

Our first set of results recorded FC changes within and between RSNs. The most consistent observation we made was that FC within RSN components decreased over the lifespan (Figure 2.3). FC of regions within ContA, ContC, DefaultB, and VisPeri exhibited a persistent decline over the entire age range considered in this study. SalVentAttnA, SomMotB, and VisCent initially increased their internal FC, but those increases were offset by larger decreases later in life so that the net change in FC was negative (Figure 2.4). These observations are consistent with other studies that have reported age-related decreases in RSN FC, including the default mode (Andrews-Hanna et al 2007; Tomasi & Volkow 2012; Geerlings et al 2014), saliency (Onada et al 2012), dorsal attention (Andrews-Hanna et al 2007; Tomasi & Volkow 2012), control (Geerligts et al 2014), and visual (Yan et al 2011) networks. A number of studies reported age-related increases in FC within motor cortices (Tomasi & Volkow 2012; Meier et al 2012), which was not observed here. This is likely due to the choice of a conservative statistical threshold; relaxing the critical  $p$ -value to  $p < 0.05$  (uncorrected) reveals that FC between regions in SomMotA increases with age, corroborating these earlier results.

In addition to FC within RSNs, we also observed age-related changes in FC between different RSN components, most of which involved increased FC, including results that were consistent with earlier findings. For example, Geerligts et al (2014) reported increased FC between default mode and control networks, as well as visual and control networks, both of which were observed

here (ContA increased FC with DefaultA, DefaultB; VisPeri increased FC with ContB). We also reported a number of apparently novel age-related, between-RSN changes in FC: including increased FC between dorsal attention components and components from both motor and saliency/ventral attention networks (DorsAttnB increased FC with SomMotA, SomMotB, SalVentAttnA, SalVentAttnB). Additionally, we observed components of the default mode network that both increased and decreased FC with respect to regions in the control network, as well as increasing FC with the saliency/ventral attention network (DefaultB increased FC with ContA and SalVentAttnA but decreased its FC with respect to ContB and DefaultA).

A number of developmental studies have reported that higher-order cognitive systems (e.g. default mode, control, attentional networks) are not yet mature by early childhood (Fair et al 2007; Fair et al 2008; Fair et al 2009; Supekar et al 2009; Jolles et al 2011). These results suggest that over development, we should see increased FC within these networks. In most cases, however, we observe linear decreases within higher-order RSNs (the exception being saliency/ventral attention), possibly due to the fact that the age ranges covering early childhood and adolescence were under-represented in the participant cohort.

The results of the FC analysis can be summarized succinctly by the modularity analysis, revealing modularity changes in ContA, ContC, DorsAttnA, SalVentAttnA, and VisPeri (Figure 2.6). The modularity measurement can fluctuate as a consequence of decreased internal or increased external FC. ContA, ContC, and VsiPeri all exhibit decreased internal FC, which likely causes their modularity to decrease. The decrease in modularity of DorsAttnA, on the other hand, is due primarily to its increased connectivity to other RSNs, for example, SalVentAttnB. The

quadratic trajectory of SalVentAttnA is likely due to a combination of both effects; functional connections within SalVentAttnA exhibit similar convex trajectories across the lifespan, while SalVentAttnA also becomes more strongly coupled to DorsAttnB, DefaultB, and ContB, which increases its external FC and drives its modularity downward. Interestingly, no default mode network components exhibited statistically significant modularity decreases despite the fact that many studies have reported decreases in its internal FC with aging (Andrews-Hanna et al 2007; Bluhm et al 2008; Tomasi & Volkow 2012). This can be explained by the choice of a conservative statistical threshold; with an uncorrected threshold of  $p < 0.05$ , DefaultA, DefaultC, and DefaultD all exhibit statistically significant decreases in modularity.

The cross-sectional nature of this study allowed us to model age-related change in FC and SC as continuous variables, which revealed that certain functional connections were best described by quadratic trajectories. In general, these involved a small subset of RSN components, most notably SalVentAttnA, VisPeri, ContA/B, and SomMotA/B. These connections could then be clustered, with SalVentAttnA and VisPeri in the one cluster and ContA/B and SomMotA/B in the other. This division is notable, and is suggestive of systems associated with visual attention and motor planning that develop, mature, and age in unison. Both clusters also involve insular cortex, which was not only identified as a structural hub region in this study, but has also been described as a key functional hub (Craig 2009). Insular cortex has been implicated in conditions related to awareness and self-reference (Klein et al 2007), and maintains strong functional connections to both cognitive control systems and motor cortex (Menon & Uddin 2010).

#### *2.4.2 Lifespan Changes in Structural Connectivity*

In terms of SC, we observed a linear decrease in the total number of streamlines,  $nf$  (Figure 2.7B), which has also been reported elsewhere (Lim et al 2013). Additionally, average fractional anisotropy,  $fa$ , reflects the integrity of white-matter fiber tracts and exhibited a steep rise from childhood to early adulthood before beginning a protracted decrease across the remainder of the lifespan (Figure 2.7C). This curve is consistent with typical FA maturational trajectories and (Barnea-Goraly et al 2005; Sullivan & Pfefferbaum 2006; Kochunov et al 2011).

Topologically, the most prominent age-related change was a linear decrease in the number of binary connections,  $m$  (Figure 2.7A), an effect that has been previously reported elsewhere (Gong et al 2009; Lim et al 2013). The decrease in connection density and average FA with aging largely agrees with the “disconnection” hypothesis, wherein cognitive decline during healthy aging is attributed to compromised white-matter connectivity (O’Sullivan et al 2001).

Despite the ongoing changes in network sparsity, we observed a consistent set of highly connected, highly central hub regions. The regions comprising the hubs actually changed very little over the course of the lifespan, which is consistent with findings of a consistent set of hub regions in preterm infants (Yap et al 2011), during development (Hagmann et al 2010; Chen et al 2013), adulthood (Hagmann et al 2008), and throughout aging (Gong et al 2009). Despite the relative constancy of hub regions, the decrease in number of connections effectively sparsified the network, leading to decreased path efficiency with age. Hence, later in life many pairs of nodes were anatomically linked by less efficient paths. We examined this effect in detail and determined that a small subset of nodes exhibited decreased path efficiency with respect to a large number of other nodes. Overall, hub regions seemed to be more susceptible to decreases in

path efficiency than non-hubs (Figure 2.8B). This finding does not necessarily indicate that hubs are selectively becoming more disconnected or that their connectivity is altered preferentially. A possible alternative explanation rests on the fact that hub regions form more connections than non-hub regions; if one selects a connection at random, it is more likely that the connection interfaces with a hub region than a non-hub region.

#### *2.4.3 Implications for Lifespan Changes in Communication Patterns*

There is mounting evidence that SC and FC are closely related to one another, with SC thought to exert a causal influence over FC patterns (Honey et al 2009; Hermundstad et al 2013; O'Reilly et al 2013). While the precise causal role is not fully understood, it has been suggested that SC shapes FC by constraining inter-areal communication processes (Honey et al 2009; Deco et al 2012). Indeed, models that incorporate SC have been able to generate synthetic FC patterns that resemble those obtained through empirical brain recordings (Honey et al 2007; Honey et al 2009; Haimovici et al 2013; Goñi et al 2014).

Given that SC topology influences FC, it was important to quantify the effects of age-related changes in SC on FC. In this study, we observed decreases in overall SC across the lifespan, which lead to decreased path efficiency among regions. Decreased path efficiency has implications for how these regions communicate with one another and the extent to which they become functionally connected. Less efficient paths tend to be associated with a decreased likelihood of signal transmission and hence should support weaker functional connectivity. The observed progressive decline in path efficiency with age implies that communication between nodes which early in life occurred via more direct connections or efficient paths requires multi-

step, less efficient paths later in life. If the way SC shapes FC remains unchanged, then age-related decreases in path efficiency should lead to a progressive weakening of FC.

However, our analysis indicates that communication along more direct paths shows a different age-related pattern than communication along more indirect paths. The FC of directly connected nodes changes very little, on average, over the entire lifespan. However, as the length of the shortest weighted paths connecting nodes increases (with a majority of them connecting nodes that belong to different RSNs), we observed a strengthening of the age-related increase in FC in the form of a stronger linear correlation (Figure 2.8C). These findings suggest that early in life inter-areal communication is facilitated predominantly by short, efficient paths but that later in life, multi-step paths become increasingly efficacious in supporting high functional connectivity. A corollary of the observed “thinning” of structural connectivity with age is that there are also fewer edges that are available for transmitting neural signals, which means that the number of shortest paths traversing a given edge is also expected to increase.

An alternative interpretation of these results is based on time-varying FC (Allen et al 2014; Hutchinson et al 2013). Our interpretation of age-related changes in FC is that changes in FC magnitude reflect increased or decreased coupling between brain regions. This view is dependent upon the static characterization of FC, where each pair of regions is assigned a single scalar (correlation) value representing the average FC over the entire scan session. On the other hand, the time-varying approach divides the BOLD time series into overlapping windows and estimates FC for each window independently, yielding for every connection a series of correlation values. In this light, changes in average FC can be accounted for not by changes in



coupling strength, but by dynamic changes in the level FC over the course of a scan session; functional connections that become more variable with age may converge towards lower overall FC strength while connections that become less variable may show the opposite effect. Time-varying FC across the lifespan was not investigated in this report, but is a topic worthy of future investigation.

How age-related changes in functional and structural connectivity within and between RSNs relate to changes in behavior and cognition is another important question for future research. The observed age-related decreases in cohesiveness of RSNs could potentially underlie the increasingly correlated task performance across different domains observed with aging (Li, Lindenberger, & Sikstrom 2001). However, such decreases in RSN coherence could reflect compensatory increases in cortical recruitment associated with relatively preserved performance (Buckner 2004) or cortical de-differentiation linked with cognitive and behavioral decline (e.g. Park et al 2010). Future longitudinal research incorporating neuropsychological measures will be able to evaluate these possibilities and their relative specificity (e.g. whether decreased coherence of attention networks specifically is uniquely positively or negatively correlated with well-documented age-related deficits in attentional mechanisms; Li et al 2001) and the extent to which different aspects of the RSN connectivity changes reported here are linked more directly with changes in age or changes in performance (as in Dosenbach et al 2010). Finally, the current findings are suggestive of changes to structural integrity (including myelin deterioration and vascular insult; Tomasi & Volkow 2012; Buckner 2004 ) leading to increased reliance on polysynaptic structural paths and thus increased functional coordination over them (see also Hawellek et al 2011), but this cross-sectional design cannot disambiguate the direction of that

relationship. Active enrichment (cognitive, social, and physical) is increasingly shown to preserve and even increase cognitive performance in aging (Hertzog et al 2009). Future longitudinal research providing such enrichment both before and after “thinning” of white matter is observed will shed light on the mechanisms underlying this changing relationship between functional and structural connectivity as well as provide critical insights into the general preservation of function in aging.

#### *2.4.4 Limitations of Current Study*

There are a number of limitations to this study, related to MR preprocessing, node definition and parcellation, modeling approach, as well as participant cohort and age range.

The first set of limitations concerns various fMRI and DTI/tractography processing steps. Regarding fMRI, FC between nodes was estimated after regressing out the global BOLD signal. While this is a contentious step because it can induce negative correlations, the interpretation of which is unclear (Murphy et al 2009; Chai et al 2012), it has also been shown that it can effectively reduce non-neural noise (Power et al 2014). A potential confound in developmental fMRI studies is head movement. We addressed this confound in two different ways. First, in our pre-processing of the fMRI data, we used the Friston-24 regression model with an additional motion parameter, which contributes to reduce motion artifacts (Yan et al 2013). Second, in our MLR analysis, we included mean frame-wise displacement as a nuisance parameter, allowing it to compete with age terms to explain variance in FC and other measures (Cao et al 2014). Regarding DTI/tractography, the present study faces several standard challenges, including detection of long-distance connections, resolving crossing fibers, as well as variations in FA

across age. Overall, SC networks reconstructed in the present study exhibit attributes that are consistent with previous work (Mwangi et al 2013), including age-related changes in FA (Barnea-Goraly et al 2005; Sullivan & Pfefferbaum 2006; Kochunov et al 2011) and network density (Gong et al 2009; Lim et al 2013), as well as hub distributions (Hagmann et al 2008; Gong et al 2009; Hagmann et al 2010; Yap et al 2011; Chen et al 2013).

Another set of limitations concerns the important step of node definition. Since we were interested in FC/SC relationships within and between RSNs, we used a parcellation that was based on a standard partition of the cortex into a canonical set of functional systems or RSNs (Yeo et al 2011), which was in line with approaches taken in previous work (Baker et al 2013; Geerligs et al 2014). This parcellation was created based on a cohort of younger participants (~21 years old), which raises the question whether it is equally appropriate for the youngest and oldest subjects in this study. In a recent paper by Cao et al (2014) that used the same dataset as this study, the authors reported that most (but not all) of their results were independent of parcellation choice. In particular, the authors used three parcellations: the Yeo parcellation used here and two other parcellations that divided the cortex into 160 and 1024 regions. Rich-club coefficients, global efficiency, modularity, and connectivity strength all demonstrated consistent age-related changes across the three parcellations. While the debate over the appropriate regional division of the brain is ongoing, future work on data-driven parcellation will allow more sensitive assessments of age-related changes in both FC and SC.

Another possible limitation was the choice to model lifespan trajectories of variables of interest as either linear or quadratic curves. While MLRs of this type have been widely used in the study

of age-related changes in brain networks, they have some inherent limitations (Zuo et al 2010; Cao et al 2014). One of the main limitations is that first and second order polynomial models may not capture higher-order behavior – i.e. variables that exhibit complicated trajectories over the lifespan might be poorly modeled by linear and quadratic curves. In future work it would be useful to explore other modeling options, such as non-parametric locally weighted regression (Cleveland & Devlin, 1988) or sliding boxcar techniques, which has been used before to model age-related changes in functional brain networks (Fair et al 2009). We did not explore such options in this paper, as we were interested in having closed form, analytic expressions for variables of interest as a function of age, which are given by the beta coefficients of MLRs but not by the other methods mentioned here. Other options for analyzing these data include multivariate measures, such as partial least squares, which could be useful for identifying patterns of connections (either functional or structural) that collectively covary with age (McIntosh & Mišić 2013).

A final set of limitations concerns the limited age range covered by the participant cohort which did not cover the early postnatal period (ages 0-7 years) and did not cover all age groups evenly. We would expect that the inclusion of infants and young children would likely impact some of the observed linear or non-linear trends in FC and/or SC as the early years are known to be a period of rapid change in all connectivity-related measures.

All of these limitations could be addressed in future work, as more sensitive data acquisition techniques, new pre-processing approaches, data-driven parcellations and extended participant samples become available.

#### *2.4.5 Conclusions*

In conclusion, this study represents a multi-modal analysis of brain functional and structural systems and the changes they undergo over the course of late development, adulthood, and aging. Our analyses suggest that RSNs corresponding to both cognitive and sensorimotor function undergo significant age-related refinement, in general becoming less functionally cohesive with age. We also demonstrate that the brain's white matter integrity, number of fiber tracts, and network sparsity all follow characteristic trajectories. As a consequence of these global changes, the efficiency with which gray matter regions were connected to one another decreased, which may be indicative of an impaired capacity for inter-areal communication. Finally, we observed that the relationship of functional and structural connectivity changed over the lifespan, so that with age, stronger functional connections are mediated by less efficient, multi-step anatomical paths.

#### *2.4.6 Acknowledgements*

RFB was supported by the National Science Foundation/Integrative Graduate Education and Research Traineeship Training Program in the Dynamics of Brain-Body-Environment Systems at Indiana University. LB was supported by a National Science Foundation Graduate Research Fellowship. JG and OS were supported by the JS McDonnell Foundation. XNZ acknowledges funding support from the Hundred Talents Program, the Key Research Program (KSZD-EW-TZ-002) of the Chinese Academy of Sciences and the Major Joint Fund for International Cooperation and Exchange of the National Natural Science Foundation of China (81220108014).

### **CHAPTER 3: FUNCTIONAL BRAIN MODULES RECONFIGURE AT MULTIPLE SCALES ACROSS THE HUMAN LIFESPAN**

This chapter attempts to address the following questions:

- How do the boundaries of functional systems (modules) change with age?
- Are these changes the same for modules at all scales?

Adapted from the paper:

Betzel RF, Mišić B, He Y, Rumschlag J, Zuo XN, Sporns O (2015 - submitted). Functional brain modules reconfigure at multiple scales across the human lifespan.

Abstract: The human brain is a complex network of interconnected brain regions organized into functional modules with distinct roles in cognition and behavior. An important question concerns the persistence and stability of these modules over the human lifespan. Here we use graph-theoretic analysis to algorithmically uncover the brain's intrinsic modular organization across multiple spatial scales ranging from small communities comprised of only a few brain regions to large communities made up of many regions. We find that at coarse scales modules become progressively more segregated, while at finer scales segregation decreases. Module composition also exhibits scale-specific and age-dependent changes. At coarse scales, the module assignments of regions normally associated with control, default mode, attention, and visual networks are highly flexible. At fine scales the most flexible regions are associated with the default mode network. Finally, we show that, with age, some regions in the default mode network, specifically retrosplenial cortex, maintain a greater proportion of functional connections to their own module, while regions associated with somatomotor and saliency/ventral attention networks distribute their links more evenly across modules.

### 3.1 Introduction

One of the hallmark properties of complex networks is that they can be analyzed at multiple levels, ranging from that of individual nodes and edges to global descriptions of the whole network. Between these two extremes lie intermediate levels at which networks can be characterized based on decompositions of the network into groups of nodes. At these levels a network can be described in terms of its community structure (Porter et al 2009; Fortunato 2010; Newman 2012), where a community (also called a “module”) refers to a densely interconnected set of nodes sparsely connected to the rest of the network (Sporns & Betzel 2015). Communities have different meanings depending upon the class of network one considers. In social networks, for example, they represent work groups (Leskovec et al 2008) or online virtual communities (Traud et al 2011) of individuals or actors, whereas in biological networks communities might correspond to groups of proteins (Guimera & Amaral 2005) or other cellular components (Ravasz et al 2002) that perform similar functions.

The flexibility of the network model has made it appealing to many areas within the biological sciences. In neuroscience recent technological advances have made it possible to represent the anatomical and functional interactions among brain regions as complex networks (Bullmore & Sporns 2009; Rubinov & Sporns 2010). The functional connectivity (FC) between two brain regions expresses the statistical dependence of their neurobiological activity, usually operationalized as a correlation (Friston 2011). The set of all pairwise correlations can be arranged to form a square matrix, which specifies a functional brain network. Like other complex networks, functional brain networks exhibit community structure and can be partitioned into groups of mutually correlated brain regions, which display characteristic topographic patterns at

rest (Yeo et al 2001; Power et al 2011; Doucet et al 2011) and that reconfigure in response to task demands (Cole et al 2014) and with learning (Bassett et al 2015). These communities, often referred to as “intrinsic connectivity networks” (ICNs) have distinct cognitive-behavioral fingerprints (Smith et al 2009; Crossley et al 2013) and have also been implicated in neuropathology and disease (Alexander-Bloch et al 2010; Fornito et al 2015).

Functional brain networks are simultaneously persistent and flexible across the human lifespan. Even in preterm infants, many of the features that typify adult brain networks are already evident, including proto-ICNs for visual, auditory, and somatosensory systems (Fransson et al 2007; Smyser et al 2010). Through early childhood and adolescence, these systems undergo refinement as short-range connections are gradually replaced by longer connections, so that by early adulthood we find recognizable, distributed functional systems (Fair et al 2007; Fair et al 2008; Fair et al 2009; Kelly et al 2009; Supekar et al 2009). Advanced aging, on the other hand, is generally accompanied by a weakening of functional connections, especially long-distance anterior-posterior connections (Ferreira & Busatto 2013). Aging may also disproportionately affect the default mode network, as both local (Tomasi & Volkow 2012) and long-range connections weaken (Andrews-Hanna et al 2007).

An important question is how the brain’s community structure changes with age. Most studies that try to address this question make comparisons between specific age ranges, for example preterm infants and adults (van den Heuvel et al 2014) or adults of different age groups (Meunier et al 2009a; Geerligs et al 2015). More recently, several papers have investigated changes in community structure from childhood to senescence, treating age as a continuous variable (Cao et



al 2014; Betzel et al 2014; Chan et al 2014). Overall, these studies converge in their findings and suggest that communities become less segregated with age, especially with advanced aging. In most of these studies, communities were defined ahead of time based on canonical representations of ICNs or uncovered using community detection methods that deliver a single partition. This entails two important limitations. First, this approach results in a “definitive” description of community structure at a particular scale, where scale refers to the size and number of communities. Such an approach does not address the possibility that communities exist over a range of scales (Betzel et al 2013) (i.e. multi-scale community structure), or are organized hierarchically (Meunier et al 2009b). Second, this approach assumes that community structure remains fixed across age groups, implying that functional communities (subsystems) cannot dissolve, change their boundaries, and that no novel communities emerge across the lifespan.

The aim of the present study is to investigate how the brain’s community structure evolves over the course of the human lifespan. We construct representative functional networks for different age groups from a cohort of 316 participants covering a large portion of the human lifespan, treating each network as a layer in a multi-layer network representation. Using community detection methods, we algorithmically resolve communities across a range of scales. We show that the modularity of functional brain networks, which measures the degree to which communities are segregated from one another, follows a scale-specific trajectory across the lifespan: at coarse scales, communities become more modular (more segregated), while communities defined at finer resolutions become less modular (less segregated). We also show that community structure is not fixed across the lifespan and that brain regions move from one

community to another with the greatest frequency occurring around young adulthood. Finally, we show that brain regions' participation coefficients, which measure the extent to which their links are distributed uniformly across communities, evolve with age. These results suggest that the process of lifespan development is associated with changes in the modular organization of brain functional connectivity at multiple scales.

## **3.2 Methods**

### *3.2.1 Data acquisition and processing*

The NKI-Rockland Sample (NKI-RS) is an ongoing project that aims to generate a large ( $N > 1000$ ) cross-sectional dataset, where the quasi-experimentally-manipulated variable is the participant's age at the time of data collection (Nooner et al 2012). This study was approved by the NKI review board and all participants provided informed consent prior to data collection. As part of the data collection process, each participant completed one anatomical scan, one diffusion structural scan and three resting-state functional MRI (rfMRI) scans that varied in terms of TR time, voxel size, and scan duration: 1) TR = 2,500 ms, voxel size = 3 mm, scan duration = 5 min; 2) TR = 1,400 ms, voxel size = 2 mm, scan duration = 10 min; and 3) TR = 645 ms, voxel size = 3 mm and duration = 10 min. We analyzed the fastest multiband imaging data, which appeared superior to the other acquisitions in terms of both accuracy and reliability of rfMRI (Zuo et al 2014). More details on these data are publicly accessible via the FCP/INDI website ([http://fcon\\_1000.projects.nitrc.org/indi/enhanced/index.html](http://fcon_1000.projects.nitrc.org/indi/enhanced/index.html)). All image data were preprocessed using the Connectome Computation System (CCS) pipeline. The preprocessing strategy included discarding the first several volumes (10 seconds), removing and interpolating spikes that arise from either hardware instability or head motion, slice-time correction, image intensity

normalization, and removing the effect of physiological noise by regressing out twenty-four parameters from a motion model (Yan et al 2013; Satterthwaite et al 2013) as well as nuisance variables such as white matter and cerebrospinal fluid signals, along with both linear and quadratic trends. Details of the image preprocessing steps are described in Xu et al (2015). In total, we processed data from 418 individual participants. The quality control procedure in the CCS excluded 64 participants due to their low-quality multimodal imaging datasets, which met at least one of the following criteria: (1) failed visual inspection of anatomical images and surfaces; (2) mean frame-wise displacement  $> 0.2$  mm; (3) maximum translation  $> 3$  mm; (4) maximum rotation  $> 3^\circ$ ; or (5) minimum cost of boundary-based registration (a measure of image registration quality)  $> 0.6$ . Additionally, thirty-two participants were excluded from subsequent analyses because of clinical diagnoses as defined by DSM-IV or ICD10 or incompleteness of the multimodal imaging datasets. Finally, six participants were excluded, as they also participated in the pilot stage of data collection. This leads to a final lifespan sample of 316 healthy participants. For the age distribution of participants see Figure 3.1.

### 3.2.2 Network construction

For each of the  $N = 316$  participants, we constructed a weighted and signed functional connectivity matrix,  $\mathbf{W} = [W_{ij}]$  whose elements denote the connection weights among pairs of  $n = 113$  cortical regions of interest, represented as nodes in our networks. The weight of the connection between nodes  $i$  and  $j$  was given by  $W_{ij} = \frac{1}{T-1} \sum_{t=1}^T z_i(t) \cdot z_j(t)$ , where  $z_i(t) = \{z_i(1), \dots, z_i(T)\}$  was the standardized (i.e. zero mean, unit variance) fMRI BOLD time series for region  $i$ . To study age-related changes in functional brain networks we constructed representative matrices for different age groups. Briefly, this process entailed assigning each

participant to one of  $K$  non-overlapping age groups. To facilitate statistical comparisons, the boundaries of age groups were chosen so that each group contained approximately the same number of individual participants. For each group,  $r \in \{1, \dots, K\}$ , we generated a composite matrix,  $\mathbf{W}_r$ , by selecting, at random, half the subjects assigned to that group and averaging their connectivity matrices. We then treated each group's composite matrix as a layer in a multi-layer network,  $\mathcal{W} = \{\mathbf{W}_1, \dots, \mathbf{W}_K\}$ . We repeated this process 500 times, thereby generating an ensemble of multi-layer networks from many sub-samples of the  $N = 316$  participants. The analyses described in the main body of the text were carried out over this ensemble of multi-layer networks with  $K = 5$  age groups or layers. The range of ages included in each group was: 8.3-22.4, 22.4-41.0, 41.0-51.4, 51.4-62.8, and 62.8-83.4 years. In the Supplement we explore the robustness of our results across varying the number of age groups, with  $K = \{4, 6, 7\}$ .

### 3.2.3 *Single-scale modularity*

The primary focus of this study was on the concept of communities (or modules) in functional brain networks. In practice, real-world networks are usually too big or too complex to identify modules by simple inspection. Finding communities in complex networks requires algorithmic “community detection” tools (Fortunato 2010). The range of methods available for detecting communities is broad (Palla et al 2005; Rosvall & Bergstrom 2008; Ahn et al 2010; Lancichinetti et al 2011; Zhang & Moore 2014), though the most common approach involves dividing a network's nodes into non-overlapping clusters based on the partition that maximizes the “modularity” quality function (Newman & Girvan 2004):

$$Q = \sum_{ij} B_{ij} \delta(g_i, g_j)$$

where  $B_{ij} = W_{ij} - P_{ij}$  is the actual weight of the connection between nodes  $i$  and  $j$  minus the expected weight,  $P_{ij}$ . The matrix  $\mathbf{B} = [B_{ij}]$  is known as “the modularity matrix.” Thus, modularity maximization aims to assign each node to a cluster,  $g_i \in \{1, \dots, C\}$ , so that the positive elements of  $B_{ij}$  fall within clusters and  $Q$  achieves as large a value as possible. These clusters are then treated as estimates of the network's communities. Clusterings that result in greater modularity scores are generally considered to be of higher quality.

The precise value of the expected weight,  $P_{ij}$ , depends upon the particular research question and is flexible to many alternative definitions. The most common definition is the graphical null model,  $P_{ij} = \frac{k_i k_j}{2m}$ , which gives the expected weight under a null model where each node's strength is preserved exactly but where connections are otherwise formed at random. Here,  $k_i = \sum_j W_{ij}$  is node  $i$ 's strength and  $2m = \sum_i k_i$  is the total weight of the network. Importantly, when a network's connectivity is defined by a correlation matrix, as is the case here, this class of null model may not be appropriate. The connection weights in a correlation matrix represent statistical relationships that are not independent of one another; “rewiring” the weights of a correlation matrix can result in a randomized matrix that violates these dependencies and may therefore not be physically realizable (Zalesky et al 2012). For this reason, several alternative definitions for  $P_{ij}$  have been proposed that are appropriate for use with correlation matrices (Bazzi et al 2014; MacMahon & Garlaschelli 2015). One such method is the uniform null model, where  $P_{ij} = \langle W_{ij} \rangle$ . Here,  $\langle W_{ij} \rangle$  denotes the average over all pairwise correlation coefficients. Implicitly, then, the uniform null model considers a community to be of high quality if its nodes

are more correlated with one another than would be expected given the average level of correlation in the entire network.

#### 3.2.4 Multi-scale modularity maximization

Maximizing modularity,  $Q$ , will return an estimate of a network's community structure. The size and number of these communities defines the *scale* at which a network's community structure is being described. However, the community structure of certain real-world networks may span multiple scales or hierarchical levels, in which case any single-scale community estimate would, at best, miss out on this richness and present an incomplete picture of a network's communities [Figure 1]. At worst, the communities returned could be misleading (Fortunato & Barthélemy 2007; Lancichinetti & Fortunato 2011). In order to detect communities at different scales, the modularity function can be modified by including a tunable resolution parameter (Reichardt & Bornholdt 2006). Changing the value of this parameter effectively shifts the scale at which communities are detected, making it possible to uncover communities of different sizes. In the present study, we incorporate the resolution parameter in the following way. Rather than set  $P_{ij} = \langle W_{ij} \rangle$ , we let  $P_{ij} = \gamma \langle W_{ij} \rangle$ , where  $\gamma$  is the “structural resolution parameter”. By absorbing the constant  $\langle W_{ij} \rangle$  into the resolution parameter, we can write  $P_{ij} = \gamma$ , which is similar to the so-called “constant Potts model” (Traag et al 2011). Thus, when the value of  $\gamma$  is small, many elements of  $W_{ij}$  will exceed  $\gamma$ . At that scale partitions that come close to maximizing  $Q(\gamma)$  will produce relatively large communities. On the other hand, when  $\gamma$  is large, very few elements of  $W_{ij}$  will exceed  $\gamma$  and the resulting partitions will feature more communities but contain fewer nodes.

### 3.2.5 Multi-layer, multi-scale modularity maximization

A further modification of the modularity function makes it compatible with multi-layer networks (Mucha et al 2010). A multi-layer network refers to a network whose nodes are linked across different layers (Kivela et al 2014). Layers may correspond to different connection modalities (e.g. cities connected by air, train, and road travel) or observations of the same network at different instants (e.g. brain networks constructed at different points in a scan session). In the present study, we define multi-layer networks where each layer is the functional connectivity matrix of a different age group [Figure 3.2]. Multi-layer modularity maximization provides a generalization of the traditional single- and multi-scale modularity maximization frameworks, making it useful for handling this type of structure.

Here we briefly discuss the mechanics of multi-layer modularity maximization. Recall that in single-layer modularity maximization the aim was to choose communities so that connections that fall within communities are mostly the positive elements of  $\mathbf{B}$ . Multi-layer modularity maximization works similarly. Let  $\mathbf{B}_r = \mathbf{W}_r - \mathbf{P}_r$  be the modularity matrix for layer  $r$ . We can define a new matrix:

$$\mathbf{B} = \begin{bmatrix} \mathbf{B}_1 & \cdots & \omega \mathbf{I} \\ \vdots & \ddots & \vdots \\ \omega \mathbf{I} & \cdots & \mathbf{B}_r \end{bmatrix}$$

The matrix  $\mathbf{B}$  has dimensions  $[n \times K, n \times K]$ , where  $n$  is the number of nodes in a single layer and  $K$  is the total number of layers. The diagonal of  $\mathbf{B}$  contains the single-layer modularity matrices for each of the  $K$  layers and each off-diagonal block contains the matrix,  $\omega \mathbf{I}$ , which is the

identity matrix whose diagonal elements are equal to the inter-layer coupling parameter,  $\omega$ . Multi-layer modularity maximization, then, tries to choose communities so that as many positive elements of  $\mathcal{B}$  fall within communities. The associated modularity function is:

$$Q_{multi} = \sum_{ijsr} [(W_{ijs} - \gamma P_{ijs})\delta(g_{is}, g_{js}) + \delta(i, j) \cdot \omega] \delta(g_{is}, g_{jr})$$

where the community assignment of node  $i$  in layer  $r$  is given by  $g_{ir}$ . In the case of the constant null model, we replace  $\gamma P_{ijs}$  with  $\gamma$ . In addition to the resolution parameter,  $\gamma$ , multi-layer modularity depends upon the value of the inter-layer coupling parameter,  $\omega$ . When  $\omega = 0$ , nodes are uncoupled across slices and maximizing  $Q_{multi}$  is equivalent to maximizing the modularity of each layer independently. When  $\omega > 0$ , nodes become coupled and can be assigned to the same community, even across layers. Thus the value of  $\omega$  determines the uniformity of community assignments across layers: when  $\omega$  is close to zero the community structure of layer  $r$  can vary considerably from that of layer  $s$ ; increasing  $\omega$  will lead to more homogeneous community structure across slices.

We used a freely available MATLAB software package (Jutla et al 2011) to perform multi-layer modularity maximization. This software uses an algorithm similar to the method of Blondel et al (2008) to maximize  $Q_{multi}$ . Rather than focusing on a single set of parameters, we explored a range of possible values. Specifically, we explored 31 logarithmically spaced values of  $\gamma \in [10^{-2}, 10^0]$  and  $\omega \in [10^{-3}, 10^0]$ , resulting in  $31 \times 31 = 961$  total parameter combinations. For each pair of parameters, we maximized  $Q_{multi}$  once for each multi-layer network in the



ensemble of networks (a total of 500 runs). We focused on this partition ensemble and characterized its statistical properties rather than treat any single run as representative.

### 3.2.6 Network measurements

Maximizing  $Q_{multi}$  returns an ensemble of multilayer partitions. From these partitions we made several measurements.

1. *Single-layer modularity*: For a single layer  $r$  associated with connectivity matrix  $\mathbf{W}_r$ , we calculated the single-layer modularity:  $Q_r = \frac{1}{2m_r} \sum_{ij} [W_{ijr} - \gamma] \gamma(g_{ir}, g_{jr})$ , where  $2m_r = \sum_{ij} |W_{ijr}|$  and  $g_{ir}$  was the community to which node  $i$  in layer  $r$  was assigned.

2. *Node flexibility*: Following Bassett et al (2011), we calculated a flexibility score as the fraction of all partitions in which node  $i$ 's community assignment changed from layer  $r$  to  $s$ , which we denote as  $f_{ir}$ . We also calculated the average flexibility of each layer as  $f_r = \sum_i f_{ir}$ . We contextualized these scores by comparing them against a permutation-based null model (see Methods, Null models) and expressing them as z-scores,  $z_{ir}$  and  $z_r$ . The z-scores indicate how much more or less flexible nodes or layers were than chance.

3. *Association matrix*: We also calculated the association matrix  $\mathbf{T} = [T_{ij}]$ , where  $T_{ij} = \sum_r \delta(g_{ir}, g_{jr})$  for each partition in the ensemble. Each element of the association matrix measures the fraction of times that nodes  $i$  and  $j$  were assigned to the same community across layers. We expressed the association matrix as the average across all partitions in the partition ensemble.

4. *Participation coefficient*: Given a partition, one can calculate how a node's connections are distributed across modules using the participation coefficient (Guimera & Amaral 2005):

$$p_i = 1 - \sum_g \left( \frac{\kappa_{ig}}{\kappa_g} \right)^2, \text{ where } \kappa_{ig} \text{ is the total weight of all connections node } i \text{ makes to module } g.$$

For a signed network (e.g. a correlation matrix), we calculate the participation coefficient of

$$\text{positive and negative links separately: } p_i^\pm = 1 - \sum_g \left( \frac{\kappa_{ig}^\pm}{\kappa_g^\pm} \right)^2.$$

### 3.2.7 Null models

We used two different null models against which we compared the results presented in the main text. To test the robustness of flexibility scores, we constructed null multi-layer partitions as part of the *permutation null model*. Let  $\mathbf{G}$  be a multi-layer partition such that  $\mathbf{G} = \{\mathbf{g}_1, \dots, \mathbf{g}_K\}$ , where  $\mathbf{g}_r = \{g_{1r}, \dots, g_{nr}\}$  is the partition of nodes in layer  $r$ . In other words,  $\mathbf{g}_r$  maps node  $i$  in layer  $r$  to one of  $C$  communities. The permutation null model leaves these node-level mappings intact, but permutes the order of the layers. For example, if  $\mathbf{G} = \{\mathbf{g}_1, \mathbf{g}_2, \mathbf{g}_3, \mathbf{g}_4\}$ , then a partition generated by the permutation null model might look like  $\mathbf{G} = \{\mathbf{g}_3, \mathbf{g}_1, \mathbf{g}_4, \mathbf{g}_2\}$ . We used this model to test the null hypothesis that, given the observed multi-layer partitions, the flexibility scores we obtained could be explained by a reordering of the single-layer partitions.

The second null model that we tested was the *network null model*. This model involved constructing random multi-layer networks,  $\mathcal{W}' = \{\mathbf{W}'_1, \dots, \mathbf{W}'_K\}$ . Whereas  $\mathbf{W}_r$  was a composite matrix that is representative of a subset of participants of roughly the same age,  $\mathbf{W}'_r$  was a composite of randomly selected subjects. The number of subjects used to construct  $\mathbf{W}'_r$  was

exactly equal to that of  $\mathbf{W}_r$ . We constructed 500 realizations of  $\mathcal{W}'$  and optimized their multi-layer modularity using precisely the same approach as applied to the empirical multi-layer networks. The output of these procedures, then, was used to test the dependence of our results on the age composition of the multilayer networks. These models were used in two instances: first, we tested whether the correlation magnitude of age and single-layer modularity,  $Q_r$ , could have been obtained by chance; secondly, we tested whether the flexibility of partitions obtained from  $\mathcal{W}'$  was comparable to the flexibility of partitions obtained from  $\mathcal{W}$ .

### 3.3 Results

The aim of this study was to characterize age-related changes in the community structure of functional brain networks at multiple scales [Figure 3.2]. We constructed representative connectivity matrices,  $\mathbf{W} = [W_{ij}]$ , for  $K$  different age groups. These matrices were then rearranged to form multi-layer networks,  $\mathcal{W} = \{\mathbf{W}_1, \dots, \mathbf{W}_K\}$ , with each age group represented as a layer [Figure 3.3]. Using a resampling procedure, this process was repeated 500 times, thereby generating 500 estimates of  $\mathcal{W}$ . The analyses described herein were carried out over this ensemble of multi-layer networks with  $K = 5$  age groups. The resulting age ranges for each group were 8.3-22.4, 22.4-41.0, 41.0-51.4, 51.4-62.8, and 62.8-83.4 years. For each network in the ensemble we maximized a multi-layer modularity function in order to obtain community assignments for brain regions across layers. This procedure allowed us to track the formation, evolution, and dissolution of communities with age. The modularity maximization process was dependent upon two parameters,  $\gamma$  and  $\omega$ , sometimes referred to as the “structural” and “interlayer” resolution parameters, respectively. By tuning these parameters we were able to examine communities of different size and number [Figure 3.4].

### *3.3.1 Multi-layer/multi-scale modularity maximization uncovers known ICNs*

We first tested whether the communities uncovered with multi-layer modularity maximization were similar to those reported in an earlier large-scale study (Yeo et al 2011). In that study, the cerebral cortex was clustered into seventeen ICNs. We compared multi-layer communities to the ICN partition by decomposing each multi-layer partition into a set of  $K$  single-layer partitions and calculating the similarity of each single-layer partition to the ICN partition as the z-score of the Rand coefficient (Traud et al 2011), where positive z-scores indicated greater-than-expected similarity. For each set of parameters,  $\{\gamma, \omega\}$ , we calculated the mean similarity over all partitions and layers (age groups) [Figure 3.5A]. We found that similarity peaked within the range  $10^{-0.6} < \gamma < 10^{-0.4}$  (approximately  $0.25 < \gamma < 0.4$ ). When we examined the single-layer partitions within this range, we found that many of the communities corresponded closely to those defined by the canonical ICN partition. To help visualize this correspondence, we constructed the association matrix,  $\mathbf{T}$ , whose element  $T_{ij}$  was equal to the number of times that nodes  $i$  and  $j$  were assigned to the same community in any layer across the partition ensemble. We then reordered the rows and columns of  $\mathbf{T}$  so that nodes belonging to the same ICN appeared next to each other [Figure 3.5B]. The block diagonal structure of the matrix indicates that nodes assigned to the same ICN in Yeo et al (2011) were also usually assigned to the same algorithmically-detected community in our study.

### *3.3.2 Age-dependent changes in community structure are scale dependent*

Next, we explored the modularity of functional brain networks across multiple scales. In order to assess age-related changes in modularity, we decomposed multi-layer partitions into single-layer

partitions, as described earlier, and calculated for each layer,  $r$ , its single-layer modularity score,  $Q_r$ , which provides an estimate of the extent to which communities in layer  $r$  are well-defined and segregated from one another. We found that  $Q_r$  varied systematically with age, though whether it increased or decreased depended on the value of  $\gamma$  (i.e. the scale of communities). Here, we focus on results at two different scales: A “coarse” scale ( $\gamma = 10^{-1.73} \approx 0.0185$ ) at which the network was divided into a small number of communities ( $3.2 \pm 0.5$  communities per layer) and a “fine” scale ( $\gamma = 10^{-0.67} \approx 0.22$ ) which resulted in divisions of the network into many small communities ( $15.4 \pm 1.0$  communities per layer). In both cases we set  $\omega = 10^{-1.5} \approx 0.032$ . By fixing the settings of  $\gamma$  and  $\omega$ , we limit our analysis to a small, but representative, subset of parameter space.

At the coarse scale, we found that  $Q_r$  increased with age [Figure 3.6A], suggesting that large communities become more segregated across the lifespan (median correlation of  $\hat{r} = +0.84$  and inter-quartile range of  $[+0.73, +0.92]$  [Figure 3.6B]). We also found that the observed correlation coefficients were statistically greater than those obtained under a network null model (t-test,  $df = 998$ ,  $t = 32.37$ ,  $p \approx 0$ ). Conversely, at the fine scale, we found that  $Q_r$  decreased with age [Figure 3.6C] (median correlation of  $\hat{r} = -0.75$  and inter-quartile range of  $[-0.88, -0.58]$  [Figure 3.6D]). In this case the observed correlation coefficients were statistically smaller than those obtained under a network null model (t-test,  $df = 998$ ,  $t = -27.46$ ,  $p \approx 0$ ). We repeated these analyses using different numbers of age groups ( $K = \{4, 6, 7\}$ ) [Figures 3.7-3.9], a different cortical parcellation (Destrieux et al 2010) [Figure 3.10], and after applying an additional motion-correction step (regressing frame-wise displacement from single-layer modularity scores) [Figure 3.11], and found consistent results.

In order to uncover the origin of this apparent interaction of modularity and age with scale, we examined the distribution of connection weights in each layer. The magnitude of  $Q_r$  depends largely on the number of connections whose observed weight exceeds that expected according to a null connectivity model (here, the expected weight was a constant and is equal to  $\gamma$ ). In general, if layer  $r$  contains many within-community connections that satisfy the condition  $W_{ijr} - \gamma > 0$ , then that layer will achieve a large modularity score,  $Q_r$ . We examined each layer (age group) at every value of  $\gamma$  and counted the number of connections that exceeded  $\gamma$ . We found that when  $\gamma \approx 0$ , the oldest age group contained the greatest number of supra- $\gamma$  connections while the youngest age group contained the fewest. As  $\gamma$  was increased, however, this relationship reversed [Figure 3.6E]. These results suggest that whether  $Q_r$  increased or decreased with age was a consequence of the shape of the connection weight distribution and its relation to the resolution parameter,  $\gamma$ .

Finally, we wanted to determine which communities were most responsible for driving the age-related increases and decreases in  $Q_r$ . To this end, we obtained consensus communities (See Figure 3.12) for both coarse and fine scales and calculated the modularity contribution,  $q_{rg}$ , that each consensus community,  $g$ , made to the total single-layer modularity  $Q_r$  (these measures are related to one another by  $Q_r = \sum_g q_{rg}$  where  $q_{rg} = \sum_{\{ij\} \in g} [W_{ijr} - \gamma]$ ). We found that at a coarse scale, a single community accounted for 70% of the total modularity and that this community's modularity was positively correlated with age, suggesting that it was the primary driver of the age-dependent evolution of the single-layer modularity score [Figure 3.6F]. This community was spatially distributed and aligned closely with the brain's task-positive system. At

finer scales, the larger communities fragmented into smaller communities whose modularity displayed distinct age-related trajectories. Several communities exhibited decreased modularity, including two communities that both contributed positive modularity ( $q_{rg} > 0$ ) in the youngest age groups but went on to contribute zero or negative modularity ( $q_{rg} < 0$ ) with increased age [Figures 3.6G and 3.6H]. The first community was comprised of retrosplenial and parahippocampal cortex and parts of the intraparietal lobule associated with the default mode network (Buckner 2004) while the second community was comprised of portions of the posterior cingulate and precuneus reported in Yeo et al (2011) as part of the control network, but more often associated with the default mode network as hub or core regions (Fransson & Marrelec 2008; Utevsky et al 2014).

### *3.3.3 Community structure varies with age*

Another important aim of this paper was to quantify the extent to which brain regions' community assignments changed with age. The inter-layer resolution parameter,  $\omega$ , played an important role in this regard. When  $\omega = 0$  communities do not span layers; i.e. communities in layer  $r$  will not appear in any other layer. However, when  $\omega > 0$ , layers become coupled to one another and communities in one layer can appear in others. In this section we choose not to focus on a single  $\omega$  value, demonstrating the robustness of our results by reporting a range of values.

In order to determine whether brain regions change communities with age, we calculated the standardized flexibility  $z_{ir}$  of each region, which indicates the number of times that node  $i$  changed its community assignment from layer  $r$  to  $r + 1$  across the partition ensemble. From the node-level flexibility scores we also calculated the standardized average flexibility of each layer,

$z_r$ . We found that average flexibility was consistently greatest between the first (8.3-22.4 years) and second (22.4-41.0 years) age groups, while flexibility was near or below chance levels for all other age groups [Figure 3.13A and Figure 3.13E].

We also examined the flexibility profiles of individual brain regions. As expected, individual nodes were also most flexible between the first and second layers [Figure 3.13B and Figure 3.13F]. From layer one to two and at coarse scales, we found that brain regions associated with control (dorsal precuneus and dorsal pre-frontal cortex), default mode (parahippocampal and retrosplenial cortex), dorsal attention (superior parietal lobule, parieto-occipital, and temporo-occipital cortex), and visual systems (striate and extra-striate cortex) were most flexible [Figure 3.13C and Figure 3.13D]. At finer scales, the flexibility pattern was different; the most flexible regions were associated almost exclusively with the default mode network (parts of temporal, posterior cingulate, and both dorsal and medial pre-frontal cortex, along with the inferior parietal lobule) [Figure 3.13G and Figure 3.13H]. At this scale, a small number of regions were far less flexible than expected, including retrosplenial cortex. We reproduced the results in this section using an alternative null model [Figure 3.14] and for different numbers of age groups [Figures 3.15-3.17]. Increasing the number of age groups allowed us to characterize, more precisely, when the brain's community structure is most flexible. Indeed, with a greater number of age groups, we found that the flexibility between the first two age groups approached chance levels. Instead, community structure appeared most flexible between age groups two (22.4-40.9 years) and three (40.9-51.4 years) for  $K = 6$  [Figure 3.17] and layers three (30.3-47.3 years) and four (47.3-54.7) for  $K = 7$  [Figure 3.17].



### 3.3.4 *Functional roles change with age*

A final focus of our study was to characterize brain regions' functional roles with respect to modules, which we assessed using the participation coefficient (Guimera & Amaral 2005). The participation coefficient measures how uniformly distributed a node's connections are across modules, with values close to one indicating greater uniformity (See Methods). The participation coefficient depends not only on the distribution of a node's connections, but also on the network's modular structure, which makes it difficult to disentangle the effect of one from the other. For this reason, we restricted our analysis to partitions obtained with  $\omega = 1$ , for which single-layer community structure was consistent across all layers. Doing so allowed us to attribute any age-related changes in nodes' participation coefficients to alterations in the distribution of nodes' connections rather than fluctuations in community structure. We also restricted our analysis to the participation coefficient of positive connections, though an analogous score can be calculated for negative connections (Rubinov & Sporns 2011).

To identify regions whose participation coefficients changed with age, we calculated the Pearson's correlation of each region's participation coefficient across layers (age). We repeated this for each partition in the ensemble, which generated a distribution of correlation coefficients. We focused on regions with distributions whose interquartile range excluded the value of zero and, for these regions, calculated the mean change in participation coefficient from the first to the final layer.

At coarse scales the regions whose participation coefficient increased most consistently and by the greatest amount were portions of the insula associated with the somato-motor network, pre-

frontal regions associated with saliency/ventral attention and control networks, and temporal regions associated with control and default mode networks [Figure 3.18A]. Other regions consistently decreased their participation coefficient, including parietal-occipital, retrosplenial, and striate/extra-striate cortices in dorsal attention, default mode, and visual networks, respectively.

At fine scales a different pattern of change emerged. The participation coefficient of regions associated with the somatomotor network continue to increase but are joined by striate/extra-striate, posterior cingulate, and medial-frontal cortex in the visual, control and saliency/ventral attention networks, respectively [Figure 3.18B]. At this scale, the regions that exhibit the biggest decreases in participation coefficient are associated with the default mode network and include retrosplenial cortex along with lateral/dorsal pre-frontal cortex and inferior parietal lobule as well as control regions in temporal cortex.

### **3.4 Discussion**

This study describes the multi-scale evolution of communities in the brain's functional connectivity across a large fraction of the human lifespan. We demonstrated that multi-layer/multi-scale community detection delivers communities that are highly consistent with known ICNs. We then show that the evolution of communities with age cannot be fully characterized at a single scale. Rather, we found that communities of different sizes and compositions allow us to uncover different (though complementary) descriptions of age-related change. At a coarse scale, we found that community structure becomes more modular and less functionally integrated with age. At fine scales this relationship reversed, and communities

became less segregated. To determine which regions change their affiliation with communities and at what point in the lifespan these changes occur, we leveraged the concept of node flexibility. We found that the pattern of change was scale-specific and that most changes in community structure occurred between the first two layers (age ranges of 8.3-22.4 and 22.4-41.0 years, respectively). Finally, we quantified the extent to which a region's connections were distributed across modules using the participation coefficient. We showed that participation coefficients follow age-related trajectories, with somato-motor and retrosplenial cortex forming proportionally more and less positive connections to other modules, respectively.

#### *3.4.1 Age-related change in community structure varies with scale*

Most previous studies of functional communities have characterized their organization at a single scale without explicitly examining community structure at other potentially biologically meaningful scales. Though there have been some efforts to study multi-scale or hierarchical modularity in brain networks, their focus has been on the advancement of theory (Betzel et al 2013) or methods, e.g. cortical parcellations (Doucet et al 2011). Using a multi-scale approach, we recapitulated some important results from the extant literature. In particular, we demonstrated that at fine scales communities grow less segregated with age (Meunier et al 2009a; Betzel et al 2014; Chan et al 2014; Cao et al 2014; Geerligs et al 2015). Exemplifying this decreased segregation were two communities that became less modular with age. The first community was comprised of parahippocampal and retrosplenial cortex while the second community contained areas in the posterior cingulate associated with cognitive control. These same regions were also among the least flexible (maintained allegiance to the same community) and exhibited the greatest decrease in participation coefficient (a larger proportion of their connections were made

to regions in the same module). Interestingly these regions have overlapping cognitive-behavioral profiles, and have been implicated in episodic memory, navigation, and orientation (Vann et al 2009). Of particular relevance to the present study is the relationship of these regions to memory and aging, where disruptions to subnetworks involving the retrosplenial and posterior cingulate cortices have been posited as neurobiological underpinnings of age-related declines in memory (Buckner 2004; Sambataro et al 2010).

The multi-scale approach also allowed us to examine community structure at a coarse scale typified by few large communities. At this scale we found communities that corresponded closely to a division of the cortex into task-positive/negative systems (Golland et al 2008). These communities become more segregated with age, a relationship driven by an increase in the modularity (segregation) of task-positive regions. Together with the concurrent decrease in the segregation of communities at finer scales, these results suggest that the brain's task-positive system becomes more integrated but in a non-specific way. This finding supports the de-differentiation hypothesis wherein brain regions lose the specificity of their functional partners with age (Grady 2012). As a possible consequence, older adults can exhibit broader spatial patterns of activity across task-positive regions compared to performance-matched younger adults, possibly as compensation for declining cognitive ability or due to impaired recruitment mechanisms (Cabeza et al 2002).

We also assessed community temporal stability across the lifespan by calculating regions' flexibility scores. We found that flexibility was greatest, on average, early in life, though individual regions exhibited greater-than-expected flexibility across all stages, suggesting that

the brain's functional systems undergo continuous refinement. These findings align with theories of the plastic brain (Pascual-Leone et al 2005), wherein subjective experience in all stages of life (Li et al 2006) promotes cortical reorganization. If we interpret these results from a practical perspective, they suggest that divisions of the cortex into canonical ICNs may not completely characterize the cognitive architecture of individuals that fall outside of the age range of young adults.

### *3.4.2 Possible mechanisms*

The nature of our data and the structure of our analyses make it difficult to directly identify neurobiological mechanisms that drive changes in community structure with age. There are several possible scenarios. One possibility is that the observed changes in community structure are driven by changes in the underlying anatomy. Across the lifespan, the brain's white and gray matter architecture undergoes continuous developmental refinement (Sowell et al 2003; Barneal-Goraly et al 2005; Douaud et al 2014). These refinements, which are region-specific and include changes in volume and myelination status, contribute to defining the brain's anatomical network. A substantial amount of variation in the magnitude of functional connectivity can be explained by the pattern in which anatomical connections, reflecting white matter fascicles, are configured (Honey et al 2009; Hermundstad et al 2013; Mišić et al 2015), and there is evidence that the strength of this relationship varies with age (Hagmann et al 2010). Thus, by influencing functional connectivity patterns, it is possible that age-related changes in anatomical connectivity ultimately underpin the observed variation in functional communities. The NKI-Rockland lifespan sample includes diffusion imaging scans, which makes it possible to construct

anatomical networks for each participant. Future work should investigate further the relationship between these two classes of networks.

### *3.4.3 Community detection for functional brain networks*

In this study we utilize a set of multi-scale and multi-layer methods for studying brain networks, which provide additional depth to the methods currently being used in the field. The multi-layer approach, for instance, confers obvious advantages, especially in the context of community detection. Most community detection approaches partition the nodes of single-layer networks into communities but leave it up to the user to match the communities detected in one layer to those in another. The multi-layer method used here partitions all layers simultaneously, maintaining a consistent set of community labels across layers and thereby automating the matching process (Mucha et al 2010). This has implications for studies that examine differences in community structure as the result of experimental manipulation or disease (Alexander-Bloch et al 2012). A multi-layer approach to community detection makes the comparison of communities between groups straightforward. The multi-layer approach also makes it easier to analyze networks whose layers are ordinally related to one another (e.g. layers that correspond to particular ages or time points). As noted in earlier studies (Cole et al 2014; Bassett et al 2015), nodes' community assignments can be tracked across layers, making it possible to quantify the instant at which a node moves to a new community, or to find frustrated nodes with no consistent community assignment.

The present study proposes several methodological innovations. First we introduce a sub-sampling procedure for constructing composite brain networks. Because resting-state scans are

of finite length and may thus provide an incomplete sample of the brain's “dynamic repertoire” in each participant, it is often considered advantageous to aggregate connectivity matrices from multiple participants into a composite matrix, thereby generating a more accurate estimate of temporally stable functional connectivity (Varoquaux et al 2010; Zuo et al 2014). A disadvantage of the approach is that the derivation of a single composite matrix precludes an assessment of outcome variability. Here, we propose to assess outcome variability with respect to different instantiations of the composite matrix. We generated multiple estimates of the composite matrices for different age groups using a sub-sampling procedure, which allowed us to quantify the variability in our results and ultimately determine the robustness of our conclusions. This procedure is only possible due to the large number of participants. As neuroscience moves into the “big data” era this type of robustness testing will likely become more feasible and desirable (Zuo et al 2014).

Second, we deal with community structure in a non-standard way. In many applications, a functional network's communities are considered to be the partition that optimizes some quality function (e.g. the  $Q$  measure). However, it has been shown that the number of near-optimal solutions grows exponentially with the size of a network (Good et al 2010), making it unlikely that any modularity-maximization heuristic will uncover the globally optimal partition. It is unclear, then, why any single near-optimal solution should be preferred over any other near-optimal solution. The strategy we adopted here was to describe the statistics of an ensemble of near-optimal solutions. This approach is, in some ways, less satisfying in that it fails to resolve a single “best” community structure, but it allows assessing the robustness of communities across a

distribution of near-optimal partitions, an approach that is less prone to error than one that depends upon a single instance of community structure.

#### *3.4.4 Methodological Considerations*

As with any MRI study, there are a number of methodological considerations that one should take into account in interpreting these results. The first issue is related to subject head motion, which has been shown to produce artifactual correlation patterns in human fMRI analyses (Power et al 2012), and is especially problematic when motion amplitude is correlated with a dependent variable, such as participant age (Satterthwaite et al 2012). We attempted to mitigate this concern by including pre-processing steps for reducing motion artifacts (Xu et al 2015) as well as regressing out motion parameters from variables of interest, such as modularity scores, and analyzing residuals (Figure 3.11). While these steps help address issues related to head motion, it is also probable that they do not completely eliminate motion as a potential confound. Future development in pre-processing strategies for MRI data will likely help address this issue.

Another concern is related to our choice of node definition. It is well known that one's choice of nodes can have an influence on the properties of the resulting networks (Fornito et al 2010). In the main text, we presented results wherein nodes were defined according to a so-called “functional atlas” (Yeo et al 2011). We also replicated our main findings by using a second parcellation, where nodes were defined according to anatomical landmarks (Destrieux et al 2010) (Figure 3.10).



A final concern is that the hemodynamic response (i.e. changes in blood volume, flow, and oxygen level) to neural activity varies across age groups (D'Esposito et al 1999; D'Esposito et al 2003). In principle, such unwanted variation makes it difficult to ascribe changes in functional connectivity and community structure solely to changes in coordination between brain regions. Future work will undoubtedly help address this issue, as better, subject- and region-specific models of neurovascular coupling become available (Handwerker et al 2012).

#### *3.4.5 Conclusion*

The findings of our study support the conclusion that the community structure of the cerebral cortex undergoes age-related changes that unfold in characteristic patterns on multiple scales. The age-dependent evolution of functional communities in the brain is incompletely captured by describing changes on a single, coarse or fine, scale. The methods and approaches underpinning our analyses are likely to provide important additional information in uncovering variations in structural and functional networks across healthy and clinical populations.

## Chapter 4: GENERATIVE MODELS OF THE HUMAN CONNECTOME

This chapter attempts to address the following questions:

- How “compressible” is the topology of the human connectome?
- Can we identify wiring rules (generative models) and parameters that produce maximally compressed connectomes while minimizing loss of information?
- Are changes in model parameters indicative of individual differences and can we use these models to identify changes in global network topology across the lifespan?

Adapted from the paper:

Betzel RF, Avena-Koenigsberger, Goñi J, He Y, de Reus MA, Griffa A, Vértés PE, Mišić B, Thiran JP, Hagmann P, van den Heuvel MP, Zuo XN, Bullmore ET, Sporns O (2015). Generative models of the human connectome. *Neuroimage*.

Abstract: The human connectome represents a network map of the brain's wiring diagram and the pattern into which its connections are organized is thought to play an important role in cognitive function. The generative rules that shape the topology of the human connectome remain incompletely understood. Earlier work in model organisms had shown that wiring rules based on geometric relationships (distance) cannot account for all topological features. Here we systematically explore a family of generative models of the human connectome that yield synthetic networks designed according to different wiring rules combining geometric and a broad range of topological factors. We find that a combination of geometric constraints with a homophilic attachment mechanism can create synthetic networks that closely match many topological characteristics of individual human connectomes, including features that were not included in the optimization of the generative model itself. We use these models to investigate a lifespan dataset and show that, with age, the model parameters undergo progressive changes, suggesting a rebalancing of the generative factors underlying the connectome across the lifespan.

## 4.1 Introduction

The human connectome represents a network map of the brain in which regions and inter-regional connections are rendered into the nodes and edges of a graph. In this format, the connectome can be analyzed using tools from network science and graph theory (Bullmore & Sporns 2009; Sporns 2014). Network analyses of the connectome have revealed a host of attributes that are likely essential for healthy brain function, including hierarchical and multi-scale modules (Bassett et al 2010; Betzel et al 2013), highly connected, highly central hubs (Hagmann 2008; van den Heuvel & Sporns 2013), and a rich club of mutually connected, high-degree regions (van den Heuvel & Sporns 2011). Additionally, the connectome's topology (the pattern in which its connections are configured) is thought to play an important role in shaping task-evoked and spontaneous brain activity (Hermundstad et al 2013; Goñi et al 2014; Mišić et al 2015).

The connectome is an example of a physical network whose nodes and edges are embedded in Euclidean space (Barthelemy 2011). Consequently, the formation of connections carries a material and metabolic cost that increases with connection length (Bullmore & Sporns 2012). To remain within the limits of viability, the human connectome maintains disproportionately many short-range (i.e. low cost) connections. Despite the importance of conserving connection cost, previous work in model organisms has shown that wiring minimization alone cannot account for all the connectome's topological features (Kaiser & Hilgetag 2006; da F Costa et al 2007). Rather, connectome networks strike a balance wherein the formation of costly features like hubs and rich clubs trades off with a drive to reduce the total cost of wiring.

The conditions that allow this tradeoff to emerge are the central topic of this paper, and one that we explore using generative models applied to human connectome data obtained from individual participants. In the context of complex networks, generative modeling refers to a set of approaches for creating synthetic networks with properties similar to those of real-world networks. One example among many (Watts & Strogatz 1998; Kumar et al 2000; Solé et al 2002; Vázquez et al 2001; Dall & Christensen 2002; Middendorf et al 2005) is the preferential attachment model (Barabási & Albert 1999), which generates synthetic networks with heavy-tailed degree distributions similar to those observed in many real-world socio-technical networks.

In this report we build upon and expand the tradition of generative models for brain networks by fitting many different generative models to single-subject human connectome data and comparing models in terms of their overall performance. The models we investigate combine two distinct mechanisms for network growth: 1) geometric wiring rules which influence connection formation by favoring either shorter or longer connections and 2) non-geometric rules that ignore the distance between two regions and, instead, form connections on the basis of some shared topological relationship. Some of the models we consider implement rules that mimic well-established growth mechanisms like geometric random graphs, preferential attachment, degree assortativity, and homophilic attraction. In all cases, our aim is to discover wiring rules that produce synthetic networks with properties similar to those of observed connectomes.

To this end, we tuned our models' parameters to generate realistic synthetic networks. We found that the best-fitting model was one that penalized the formation of longer connections while

increasing the likelihood of forming connections between brain regions with similar connectivity profiles (homophily). We cross-validated this result, comparing synthetic and observed connectomes along measures other than those used in the optimization process and using three different datasets. Finally, we fit the optimal generative model to data from a lifespan study (with ages ranging from 7-85 years) and found that the penalty on long-distance connections weakened monotonically with age. Older subjects' connectomes were fit poorly compared to those of younger individuals, a result driven primarily by an inability to match edge length and clustering coefficient distributions. This suggests that the human connectome undergoes a characteristic reorganization across the lifespan.

## 4.2 Results

We fit generative models to the connectomes of individual participants. In the main text, we focus on 40 adults (ages 18-40 years) scanned at the Department of Radiology, University Hospital Center and University of Lausanne (CHUV), Lausanne, Switzerland. The supplementary text contains results from replication cohorts of 214 and 126 participants from the Human Connectome Project (HCP) (Van Essen et al 2012; Glasser et al 2013) and the Nathan Kline Institute, Rockland, New York (NKI) cohort (Nooner et al 2012), respectively. In the same supplement we also investigate the sensitivity of our results to alternative processing streams. For details regarding MRI image acquisition and pre-processing see Methods.

In general, all the models we considered were of the same form. Starting with a sparse seed network (62 bi-directional edges that were common across all 40 participants), edges were added one at a time over a series of steps until  $M$  total connections were placed (where  $M = 576 \pm 57$

connections across subjects). The relative probability of connecting nodes  $u$  and  $v$  at any step was given by:

$$P(u, v) \approx E(u, v)^\eta \times K(u, v)^\gamma$$

In this expression  $E(u, v)$  denotes the Euclidean distance between brain regions  $u$  and  $v$ . The exponent  $\eta$  controls the characteristic connection length. When  $\eta < 0$ , short-range connections are favored, while  $\eta > 0$  increases the probability of forming longer connections. The other term,  $K(u, v)$ , represents an arbitrary non-geometric relationship between nodes  $u$  and  $v$  and the value of  $\gamma$  scales its relative importance. The precise definition of  $K(u, v)$  is flexible and can be varied to realize different wiring rules. For instance, setting  $K(u, v) = k_u k_v$  and  $\gamma > 0$  implements a variant of preferential attachment, wherein higher degree nodes are more likely to become connected. Alternative definitions can be used to implement rules such as degree assortativity (e.g.  $K(u, v) = |k_u - k_v|$ , where nodes with similar/dissimilar numbers of connections preferentially connect to one another) or homophily (e.g.  $K(u, v) = \sum_w a_{uw} a_{wv}$  where connections form between nodes with more or fewer common neighbors). In Table 4.1 we show a complete list of all non-geometric wiring rules.

To assess the fitness of a synthetic network we calculated its energy, which measures how dissimilar a synthetic network is to the observed connectome. Intuitively, if the two networks have many properties in common, then the synthetic network's energy is small. Specifically, a synthetic network's energy was defined as:

$$E = \max(KS_k, KS_c, KS_b, KS_e)$$

where the arguments are Kolmogorov-Smirnov statistics which quantify the discrepancy between the synthetic and observed connectomes in terms of their degree ( $k$ ), clustering ( $c$ ), betweenness centrality ( $b$ ), and edge length ( $e$ ) distributions. By taking the maximum of the four statistics we consider a synthetic network to be only as fit as its greatest discrepancy.

#### 4.2.1 Geometric models cannot generate clustered networks with long connections

It is well known that the connectome's physical embedding shapes its topology by promoting the formation of low-cost connections (Bullmore & Sporns 2012). On the other hand, forming only the shortest connections produces a skewed edge length distribution lacking long-distance connections (Kaiser & Hilgetag 2006), resulting in increased characteristic path length, thereby reducing the efficiency with which information can flow between distant brain regions. We first sought to test the extent to which cost conservation shapes the topology of the human connectome by implementing a pure geometric model (i.e.  $K(u, v) = 1$ ).

For each participant we tuned the free parameter,  $\eta$ , to a range where the geometric model consistently produced synthetic networks with near-minimal energies (Figure 4.1B) and analyzed the top 1% lowest-energy synthetic networks (100 networks/participant). At this point in parameter space ( $\eta = -4.01 \pm 0.31$  sample mean  $\pm$  standard error; see Figure 4.1C), synthetic networks achieved an average energy of  $E = 0.29 \pm 0.02$  with KS statistics  $KS_k = 0.15 \pm 0.03$ ,  $KS_b = 0.18 \pm 0.04$ ,  $KS_e = 0.27 \pm 0.03$ , and  $KS_c = 0.29 \pm 0.02$  (Figure 4.1B). To

contextualize these scores, we compared them to KS statistics obtained from a null generative model where connections were formed with uniform probability. We found that, with the exception of  $KS_e$  ( $p \approx 0.4$ ; Wilcoxon signed-rank test; Wilcoxon 1945), the geometric model produced significantly lower energy and smaller KS statistics (maximum  $p \approx 10^{-5}$ ).

Interestingly, the point at which energy is minimized deviates from the respective minima of  $KS_e$  and  $KS_c$ , demonstrating that even the-best fitting synthetic networks generated by the geometric model cannot simultaneously match observed connectomes in terms of clustering and edge length distributions. The reason for this is intuitive: A strong distance penalty is required to generate highly clustered networks, which inadvertently penalizes the formation of long-distance connections. Conversely, realistic edge length distributions arise when the distance penalty is relatively weak, at which point synthetic networks become vastly under-clustered. The energy minimum occurs at a point situated between these two extremes, trading off accuracy along one dimension with the other though never simultaneously minimizing both (Figure 4.1D).

#### *4.2.2 Models driven by geometry and topology outperform pure geometric models*

The failure of the pure geometric model to generate synthetic networks that were as clustered and contained as many long-distance connections as observed connectomes suggests that additional factors are needed as part of a realistic generative mechanism. To determine which factors were most capable in this regard we compared twelve different generative models where topological features such as degree, clustering, and homophily influenced the connection formation probabilities. As expected, due to the additional free parameter,  $\gamma$ , we find that all dual-factor models outperformed the pure geometric model, generating synthetic networks with



significantly lower energies ( $p \approx 0$ , see Figure 4.2). Importantly, dual-factor models were stratified, with clustering-based models outperforming degree-based models, which in turn were outperformed by homophily-based models. The absolute best model incorporated a homophilic attraction mechanism in the form of the matching index (MI), which is a normalized measure of overlap in two nodes' neighborhoods. If  $\Gamma_u = \{v: a_{uv} = 1\}$  represents the set of node  $u$ 's neighbors, then the matching index is equal to:

$$M_{uv} = \frac{|\Gamma_{u \setminus v} \cap \Gamma_{v \setminus u}|}{|\Gamma_{u \setminus v} \cup \Gamma_{v \setminus u}|}$$

where  $\Gamma_{u \setminus v}$  is simply  $\Gamma_u$  but with  $v$  excluded from the set. In the event that  $u$  and  $v$  have perfect overlap in their neighborhoods, then  $M_{uv} = 1$ . If the neighborhoods contain no common elements then  $M_{uv} = 0$ .

Applied to the CHUV dataset, the MI model achieved an average energy of  $E = 0.12 \pm 0.02$  with parameters  $\eta = 0.98 \pm 0.37$  and  $\gamma = 0.42 \pm 0.04$  (Figure 4.3C). Together, these parameter values indicated that, like the pure geometric model, the MI model exercised a penalty against long distance connections (albeit markedly weaker than the geometric model), while increasing the probability that nodes with similar connectivity profiles would connect to one another. Interestingly, the parameters  $\eta$  and  $\gamma$  appear to trade off with one another (Figure 4.3D), suggesting that the more an individual's connectome is shaped by geometry (large amplitude of  $\eta$ ) the less it is shaped by non-geometric constraints and vice versa. On average, the MI model outperformed the geometric model in reducing discrepancies along all four components of the

energy function:  $KS_k = 0.10 \pm 0.03$ ,  $KS_b = 0.10 \pm 0.02$ ,  $KS_e = 0.10 \pm 0.03$ , and  $KS_c = 0.11 \pm 0.02$  (maximum  $p$ -value for all KS statistics and energy was  $p \approx 10^{-7}$ , Wilcoxon signed-rank test). Whereas the geometric model's performance was limited primarily by mismatches in clustering and edge length, the MI model's performance was more evenly limited. The best-fitting synthetic networks had energies equal to  $KS_k$ ,  $KS_b$ ,  $KS_c$ , and  $KS_e$  around 21%, 25%, 29%, and 25% of the time, respectively.

#### 4.2.3 Evaluating synthetic networks using additional measures

Our analyses to this point consisted of tuning the parameters of generative models to ranges where the synthetic networks achieved low energy, which identified the MI model as the best fitting model. The form of the energy function, however, may be considered *ad hoc*; it represents only one of many alternative ways to evaluate a synthetic network's fitness. For this reason it was important to establish that the best-fitting synthetic networks generated by the MI model matched observed connectomes across additional dimensions that were not part of the energy function used for optimization. To that end, we subjected the lowest-energy synthetic networks to a series of additional tests to determine whether they could also reproduce other properties of the human connectome.

#### 4.2.4 Graph theoretic measures

The first test involved evaluating the best-fitting synthetic networks in terms of how well they matched graph-theoretical properties of observed connectomes, focusing on the measures: mean clustering ( $C$ ), global efficiency ( $E$ ), degree assortativity ( $R_k$ ), modularity ( $Q$ ), characteristic path length ( $L$ ), and network diameter ( $\max D$ ) (see Supplement for descriptions of these measures).

We estimated the magnitude of correlation between graph measures made on synthetic networks generated by the MI model and the same measures made on empirical networks. We found that the MI model did an excellent job reproducing the rank order of individual participants' mean clustering ( $r = 0.90, p \approx 0$ ), modularity ( $r = 0.69, p \approx 10^{-6}$ ), characteristic path length ( $r = 0.86, p \approx 10^{-12}$ ), and efficiency ( $r = 0.64, p \approx 10^{-5}$ ). Network diameter ( $r = 0.23, p = 0.15$ ) and degree assortativity ( $r = 0.05, p = 0.74$ ) were not well matched (Figure 4.4A). It should be noted that, in general, most graph measures are not completely orthogonal to one another.

While the MI model generally reproduced the rank order of participant-level graph measures, it nonetheless systematically over-/under-estimated the values of certain measures. For instance, efficiency was, on average, smaller for synthetic networks than for empirical networks (points falling above the diagonal in Figure 4.4A, third panel). The same is true for characteristic path length (over-estimated). Despite these biases, the discrepancy between empirical and synthetic networks for any of these measures was, on average, small - across participants, the mean clustering, modularity, path length, and efficiency scores of synthetic networks were always within 5.5% of the same measure made on the corresponding observed network.

#### *4.2.5 Distance-dependent degree assortativity*

The human connectome features hub regions linked by long distance connections, forming rich clubs and cores. This propensity for higher-degree nodes to be linked by longer connections should be reproducible by a good generative model. To assess whether this were the case, we extracted and pooled across participants the list of all connections, the degrees of their stubs ( $k_u$

and  $k_v$ ), and length ( $E(u, v)$ ). From these data, we estimated the three-dimensional cumulative distribution function,  $F(k_\alpha, k_\beta, E(\alpha, \beta))$ . At any point  $\{k_\alpha, k_\beta, E(\alpha, \beta)\}$ , the value of  $F$  corresponded to the fraction of all connections satisfying  $k_u \leq k_\alpha$ ,  $k_v \leq k_\beta$ , and  $E(u, v) \leq E(\alpha, \beta)$  ( $k_u$  and  $k_v$  were ordered so that  $k_u \leq k_v$ ). We constructed similar distributions for the best-fitting synthetic networks generated by each model and quantified the discrepancy between distributions with a KS statistic. In general, the rank order of models scored by this KS statistic was similar to the rank order of their energies (Figure 4.4B). The MI model achieved the smallest KS statistic ( $KS = 0.12 \pm 0.01$ ) while the pure geometric model, on the other hand, performed the worst ( $KS = 0.37 \pm 0.01$ ).

#### 4.2.6 Local statistics

Finally, we tested whether the best-fitting synthetic networks generated by the MI model were capable of predicting the degree and clustering coefficient sequences of the connectome. We expressed each node's empirical degree,  $k_u$ , and clustering coefficient,  $c_u$ , as z-scores by standardizing the empirical values against the distributions obtained from the best-fitting synthetic networks. Z-scores were averaged across subjects and used to quantify the discrepancy in those measures (larger scores indicated poorer fit). We compared these z-scores against scores obtained from the best-fitting synthetic networks generated by the pure geometric model in order to ascertain whether they represented an improvement in fitting local network measures (Figure 4.4C). We found that, on average, the MI model produced smaller discrepancies (points below the diagonal) compared to the geometric model. Typically, the largest improvements were for nodes whose degree or clustering coefficient was mismatched the greatest by the geometric

model. For some nodes, however, the geometric model actually outperformed the MI model, though the standardized scores for these nodes were, generally, rather small for both models.

#### 4.2.7 Application to human lifespan data

In addition to quantifying models' performances, we asked whether the parameters of the generative models captured meaningful information about individual differences in network organization. To demonstrate the utility of the network modeling approach for characterizing individual variation, we extended our analysis to the NKI dataset's  $N = 126$  participants, spanning a range of ages from 7-85 years. We hypothesized that age-related changes in network organization may be captured by the parameters of the generative models,  $\eta$  and  $\gamma$ . We tested this hypothesis by first regressing out participants' intracranial volumes and mean framewise displacement from parameter values obtained from the best-fitting MI models and correlating the residuals with participant age. We also expressed energies and KS statistics as z-scores relative to a generative model in which connections were formed randomly to correct for variations in network density with age (Betzel et al 2014; Lim et al 2015). The results of these analyses indicated that the value of  $\eta$  decreased in magnitude with age ( $\hat{r}_{age,\eta} = 0.39, p \approx 10^{-5.3}$ ), while  $\gamma$  did not exhibit any significant age-related changes ( $\hat{r}_{age,\gamma} = 0.39, p \approx 0.45$ ), which implied that the penalty on long-distance connections weakened with age. We also found that  $E$ ,  $KS_e$ , and  $KS_c$  all increased with age (max  $p \approx 10^{-4.7}$ ) (Figure 4.5), indicating that the MI model does an increasingly poor job capturing the organization of older connectomes compared to younger connectomes.

### 4.3 Discussion

In this report, we tested different classes of generative models for the human connectome. Our study makes several novel contributions, by quantitatively comparing different sets of generative models, by applying these models to human connectome data, and by fitting models to networks of individual participants. We confirmed that pure geometric models cannot create synthetic networks that were both as clustered and also contained the same proportion of long-distance connections as the observed human connectome. To identify which additional factors were most capable of creating realistic networks we incorporated non-geometric information into our generative models' wiring rules. With this additional degree of freedom, the synthetic networks generated by these more complex models more accurately reproduced the connectome's clustering and edge length distributions. The best-fitting model formed connections on the basis of homophilic attraction (matching index) combined with geometric constraints. Importantly, synthetic networks generated by this model not only reproduced degree, betweenness centrality, clustering coefficient, and edge length distributions (all measures that contributed to the energy function used for optimization), but they also reproduced additional graph theoretic properties such as characteristic path length, mean clustering, global efficiency, modularity, the propensity for high-degree nodes to be connected via long-distance edges, and local node statistics such as degree and clustering coefficient sequences. We also demonstrated robustness of the matching index model, comparing it across three separate datasets totaling  $N = 380$  participants and finding consistent results in all cases (See Supplement). As a final demonstration of the utility of generative models, we fit the MI model to connectomes of individuals whose ages ranged from 7-85 years, showing that the distance penalty weakened with age while energy increased, an effect driven by growing discrepancies in clustering and edge length distributions.

Generative models for brain networks have been investigated before, serving as proofs of concept (Kaiser & Hilgetag 2004a; Kaiser et al 2009; Lim et al 2015) or as investigative tools for non-human connectome data (Kaiser & Hilgetag 2004b; Kaiser & Hilgetag 2007; da F Costa et al 2007; Nicosia et al 2013). One limitation of earlier studies was the use of composite connectivity matrices as empirical benchmarks. For example, Ercsey-Ravasz et al (2013) and Song et al (2014) proposed geometric models of an incomplete macaque connectome, where connections were based on composite tract-tracing data compiled across multiple subjects and only a subset of cortical areas. Another limitation of earlier work was the lack of model comparison. In many cases proposed generative models were only compared against random generative models (Ercsey-Ravasz et al 2013; Song et al 2014) where connections were formed with uniform probability, as opposed to models incorporating more plausible generative mechanisms.

The first model we examined was the pure geometric model, which was the simplest but also, in accordance with earlier studies, performed the worst. The observation that geometry only partly explains the topology of brain networks is in line with in a large literature on wiring minimization (Mitchison 1999; Laughlin & Sejnowski 2003; Cherniak et al 2004; Samu et al 2014), and has been appreciated in modeling studies of both human brain networks (Henderson & Robinson 2013; Kaiser & Hilgetag 2004b; Vértes et al 2012; Klimm et al 2014) and those of non-human primates (da F Costa et al 2007). Our findings also support the view that strong spatial constraints alone are insufficient for explaining all topological aspects of brain networks (Kaiser et al 2006; Bullmore & Sporns 2012). This conclusion stands in contrast to other reports (Ercsey-Ravasz et al 2013; Song et al 2014) suggesting that geometric models are the sole

generative mechanism underlying the connectome's formation and evolution. Instead, we find that in order to accurately reproduce the connectome's topology our models required information about node's pairwise similarity (homophily), which agrees with earlier modeling studies of the primate connectome (da F Costa et al 2007) and human functional brain networks (Vértes et al 2012).

The final component of this report was an application of network modeling to human lifespan data, which revealed that geometric constraints weakened while energy and the mismatch of clustering and edge length distributions all increased with age. Collectively, these results indicate that the MI model is becoming an increasingly poor model of the connectome as participants become older. There are a number of possible explanations. For example, connectome patterns may become increasingly random with age, making it impossible for any wiring rule to model the connectome precisely. Alternatively, connectomes may exhibit different types of topology in younger versus older subjects (perhaps as a consequence of selective pruning). To accurately model these connectomes would require more complicated models and the introduction of additional growth mechanisms.

The aim of this study was not to model the growth and development of the human connectome. Doing so would have required a more complicated model that included more system-specific detail. Instead, our models were designed to reduce a network's description length. Naively, we can reconstruct a network exactly from a list of its nodes and edges. However, such a precise reconstruction may not be necessary or even desirable. Oftentimes we are more interested in a network's high-level properties (e.g. modularity, degree distribution, etc.), than the exact



configuration of its connections. In such a case, a mechanism that generates synthetic networks with the approximately the same set of properties represents a much more economical (compressed) description of the network. Our models are in line with this approach, seeking a parsimonious description of the human connectome, wherein its overt complexity gets compressed into a model's wiring rule and parameters. This type of compressed description can be used toward any number of ends, including investigation of differences in individual participants. For instance, we found that some participants' connectomes were compressible (low energy) while others were not (high energy). An important question, moving forward, is whether these differences become meaningful when examining individual differences or comparing clinical and control populations, or whether they can be related to some behavioral measures across both individual and group levels.

There are a number of methodological considerations that should be discussed. First, the class of dual-term models left the definition of  $K(u, v)$  up to the user. For practical reasons, we explored only twelve such rules. Even with this limited exploration, we found a great deal of stratification in terms of model performance. This leaves open the possibility that wiring rules not explored in this report could produce superior results. While enumerating of all possible wiring rules is impractical, a number of methods have been proposed that aim to discover wiring rules by evolving models themselves (Bailey et al 2012; Menezes & Roth 2014), as opposed to proposing a model and fitting its parameters, as we did here. These approaches, we believe, warrant further attention.

Another methodological consideration concerns the evaluation of a synthetic network's fitness. The synthetic networks are mapped into a morphospace (Goñi et al 2013) according to their geometric and topological properties and compared to the observed connectome along the same dimensions. Whether these properties are the most appropriate measures for network comparison is unclear. In principle, one could define alternative energy functions whose minima may not coincide with those reported here, and for which the MI model is not the best performer. Though the exploration of alternative energy functions is beyond the scope of this report, we attempted to mitigate the concern that our choice of energy function biased our results by performing a series of additional tests, the results of which indicated that the MI model consistently outperformed other models.

Another consideration relates to the combination of diffusion imaging and tractography for inferring the connectome's organization. Though diffusion imaging/tractography represents the state of the art for in vivo reconstruction of the brain's anatomical connections, these technologies are nonetheless prone to false positives and negatives (Thomas et al 2014), which could potentially affect our results. While the use of multiple atlases, independent datasets, and alternative processing streams help reduce the bias of any single processing strategy they do not completely address the issue. The shortcomings of diffusion imaging and tractography, while presently limiting, also serve to highlight the need to develop new non-invasive methods for mapping the human brain.

A final consideration is related to the size of networks, the definition of nodes, and the scalability of our models. In general, how one defines a network's nodes has implications for the network

properties of the resulting graph (Zalesky et al 2010). It is likely that the size and number of nodes factor into the performance of the models studied here. The networks analyzed in this report consisted of either  $n = 74$  or  $n = 108$  nodes, representing two different parcellations of the cortex. However, it is becoming increasingly common to model brain networks with up to thousands of nodes. Because the number of possible positions to place an edge grows as  $O(n^2)$ , the space of all networks that the model could generate becomes much larger as  $n$  increases. Models with  $n \gg 10^2$  may require stronger parametric constraints (e.g. larger magnitudes for  $\eta$  or  $\gamma$ ) or incorporating additional topological information (and an additional parameter) into a model's wiring rule. In general, the choice of how to define a network's nodes and at what scale the human connectome is best described is unclear, though future work on data-driven parcellations will surely help address this issue.

## 4.4 Methods

### 4.4.1 Generative algorithm

The algorithm for producing synthetic networks is simple. Starting with a seed network comprised of connections common to all subjects, connections are added in sequence until a pre-specified number (equal to the number of edges in the observed network) have been placed. At each step, the relative probability that nodes  $u$  and  $v$  will become connected is given by  $P(u, v) = E(u, v)^\eta \times K(u, v)^\gamma$ , where  $E(u, v)$  and  $K(u, v)$  are the Euclidean distance and an arbitrary topological relationship, respectively, between nodes  $u$  and  $v$ . To prevent cases where  $P(u, v)$  is undefined (e.g. if  $K(u, v) = 0$  and  $\gamma < 0$  then  $P(u, v) = \infty$ ), we add  $\epsilon = 10^{-6}$  to each  $K(u, v)$  before raising it to the power,  $\gamma$ . Over the course of the generative process new edges are added to the synthetic network which necessarily changes the value of  $K(u, v)$ . Accordingly, at

each step we update  $K(u, v)$  and the corresponding changes to  $P(u, v)$ . If, at any step, the edge  $\{u, v\}$  is added to the synthetic network, then  $P(u, v) = 0$  for all subsequent steps.

#### 4.4.2 Model optimization

Given the generative rule and the energy measure for evaluating a model network's goodness of fit, it was important to find the parameters  $\{\eta, \gamma\}$  that produced networks with the lowest possible energy values. To solve this optimization problem, we developed a simple procedure based on classical Monte Carlo methods. The procedure consisted of three stages that were repeated:

1. A sampling stage in which points in parameter space are selected
2. An evaluation stage, where synthetic networks are generated with the previously-selected parameter values and their energies calculated.
3. A partitioning stage, in which the entire parameter space is partitioned according to a Voronoi tessellation.

The procedure is initialized in stage 1 by randomly sampling  $N_{samp} = 2000$  points from parameter space. After evaluating the energy at each point and partitioning the entire parameter space into Voronoi cells, the algorithm returns to stage 1. Rather than sample points randomly, points are now sampled from within the boundaries of Voronoi cells, where the probability of drawing a point from within any given cell is inversely proportional to that cell's energy ( $P_C \propto E_C^{-\alpha}$ , where  $E_C$  is the energy of Voronoi cell,  $C$ , and  $P(C)$  is the relative probability of sampling from within that cell). This procedure ensures that points are sampled preferentially from low-energy regions of parameter space. We repeated stages 1, 2, and 3 a total of five times

and varied  $\alpha$  with each repetition, going from  $\alpha = \{0.0, 0.5, 1.0, 1.5, 2.0\}$ . Early on, the low values of  $\alpha$  meant that we searched the parameter space randomly, while the larger values at later repetitions allowed us to focus in on the low energy regions. We emphasize that alternative optimization schemes could be used to minimize  $E$  (e.g. simulated annealing); the approach used here was chosen because it allowed us to not only converge to good solutions, but also to explore the energy landscape.

#### *4.4.3 Data acquisition and processing*

Whole-brain tractography was performed on diffusion spectrum imaging (DSI) data acquired from  $N = 40$  participants. The cortex was parcellated into the  $n = 219$  regions according to a subdivision of FreeSurfer's Desikan-Killiany atlas (Cammoun et al 2012), of which we retained the 108 regions comprising the right hemisphere. The processing of these data have been described in greater detail elsewhere (Avena-Koenigsberger et al 2014; Goñi et al 2014; Betzel et al 2013). We enforced an average connectome density of  $\rho \approx 10\%$ , resulting in a streamline threshold of 27 streamlines (i.e. a minimum of 27 streamlines must have connected two regions for us to consider the presence of an anatomical connection).

### **4.5 Supplement**

The main text describes the results of generative models applied to a dataset of 40 participants scanned at CHUV. In this supplement we demonstrate the robustness of those results by reproducing the principal findings using alternative datasets. The additional datasets are described, briefly, below and in more detail later in this supplement. Figures 4.6-4.14 shows model energies for each of the additional datasets, reproducing Figure 4.2 from the main text.

1. Two replication datasets (HCP and NKI) of  $N = 214$  and  $N = 126$  participants, respectively.
2. The same CHUV dataset with different levels of network density (5% and 15%) and defined using an alternative weighting.
3. CHUV dataset including both left/right cerebral hemispheres.
4. Composite (i.e. group averaged) CHUV, HCP, and NKI connectomes.

In addition to describing these datasets, we discuss whether Euclidean distance is an appropriate substitute for the actual length of white matter fibers. At the end of this supplement we have also included, as an appendix to the supplement, a glossary of graph theoretic terms that appear throughout the main text.

#### *4.5.1 Additional Datasets*

##### *Human connectome project (HCP) - See Figure 4.6*

The HCP data were drawn from the 215 participants made available as part of the Q3 release of the human connectome project (Van Essen et al 2012; Glasser et al 2013). From each participant's diffusion-weighted MR images (diffusion tensor imaging; DTI), white matter fibers were reconstructed from generalized q-sampling (Yeh et al 2010) (GQI: allowing for the reconstruction of crossing fibers) and streamline tractography and the cortex was parcellated into 219 parcels based on a subdivision of FreeSurfer's Desikan-Killiany atlas (Cammoun et al 2012). More details on the processing of these data can be found elsewhere<sup>5</sup>. We focused on the right hemisphere only, which consisted of  $n = 108$  regions. We imposed a threshold on

streamline counts of (de Reus & van den Heuvel 2014) (i.e. a minimum of five streamlines must be present for us to consider two regions linked by a binary connection) in order to maintain an average connectome density of  $\rho \approx 10\%$  across subjects. We excluded a single subject on the grounds that their total streamline count was greater than two standard deviations from the group mean, leading to a final dataset of  $N = 214$  participants.

*Nathan Kline Institute, Rockland, NY (NKI) - See Figure 4.7*

The NKI dataset consists of  $N = 126$  participants whose ages ranged from 7-85 years (Nooner et al 2012). Tractography was performed using the Connectome Computation System (CCS: <http://lfc.d.umn.edu/ccs.html>). A more detailed description of the processing pipeline was included in other reports (Betzel et al 2014; Cao et al 2014; Yang et al 2014). Unlike the HCP and CHUV datasets, the cortex was parcellated into 148 regions according to the Destrieux atlas (Destrieux et al 2010). We analyzed a single hemisphere ( $n = 74$  regions), but instead of focusing on either the right or left, we formed a composite matrix by combining the streamline counts between homotopic pairs of regions. We, again, enforced a mean density of  $\rho \approx 10\%$  by selecting a streamline threshold of 30 streamlines.

*Alternative CHUV datasets - See Figures 4.8-4.11*

We investigated four variants of the CHUV dataset. In the main text we analyzed binary connectivity matrices (average density of  $\rho \approx 10\%$ ) by applying a threshold to streamline counts. The first two variants were constructed in the same manner but with the threshold level chosen to maintain average densities of  $\rho \approx 5\%$  and  $\rho \approx 15\%$ . The third variant retained a threshold of  $\rho \approx 10\%$  but instead of thresholding streamline counts we thresholded "fiber

density" matrices. The fiber density between nodes  $u$  and  $v$  is a common choice for edge weights in weighted anatomical brain networks, and is defined as the number of streamlines divided by the sum of  $u$  and  $v$ 's surface areas (Hagmann et al 2008; Betzel et al 2013; Goñi et al 2014). The fourth variant was constructed by thresholding streamline counts to  $\rho \approx 10\%$  but included both left and right cerebral hemispheres.

*Group-average matrices - See Figures 4.12-4.14*

In addition to single-participant modeling, we analyzed group-average connectivity matrices for all three datasets (CHUV, HCP, and NKI). Group-average matrices boost the ratio of signal to noise by emphasizing connections that are consistently expressed across subjects, thereby rendering the human connectome more clearly. The *de facto* method for generating group-average matrices is to retain the supra-threshold elements of the  $[n \times n]$  consistency matrix,  $\mathbf{C}$ , whose element  $c_{uv}$  indicates the fraction of all participants in which a connection was present between nodes  $u$  and  $v$ . The resulting matrix, however, over-expresses short-range connections, as short-range connections are more easily reconstructed and are hence the most consistent connections across subjects whereas long-range connections are more prone to error. Also, this method forces a user to choose, somewhat ad hoc, the threshold for including a connection in the group-average matrix. Instead, we use an alternative method for generating a group-average connectomes whose edge-length distribution matches that of the typical single-participant distribution (Mišić et al 2015). Briefly, this method begins by first estimating the average number of connections of a given length in a typical participant's connectome. Next, all pairs of nodes separated by a comparable distance are identified and, from among this subset, the most consistent connections are added to the group-average connectivity matrix. Repeating this



process for all distances yields a representative connectome that matches, almost exactly, the typical edge length distribution, but features only the most consistently expressed edges at each connection length.

#### *4.5.2 Fiber length versus Euclidean distance*

In this report, we test the hypothesis that the human connectome emerges as a consequence of both topological and spatial constraints, which we model as power-law functions. In doing so, we assume that the material/metabolic cost of fiber tracts can be equated to Euclidean distance separating its endpoints, rather than the actual integrated length of the curved tract. The argument for doing so is twofold. First, estimates of fiber length can only be obtained for completed streamlines, meaning that no estimates exist for connections that were absent in the observed tractography data. In order to fill in the missing fiber lengths, one can resort to fiber interpolation (i.e. using the distance/fiber length relationship of existing connections to determine the fiber length of missing connections), which necessarily introduces an additional source of uncertainty. Second, the relationship of fiber length and Euclidean distance is rather strong across our datasets: the amount of variance in fiber length accounted for by Euclidean distance was 66%, 32%, and 79% for the CHUV, NKI, and HCP datasets, respectively. For these reasons, we assert that Euclidean distance, though imperfect, is a reasonable proxy for the cost of forming a connection.

## **CHAPTER 5: CONCLUSION**

### **5.1 Dissertation summary**

In this dissertation I presented three related studies that examined brain networks and how they change over the course of the human lifespan. In Chapter 2 we used mass-univariate testing to identify functional connections that exhibited either linear or quadratic trajectories across the human lifespan. These connections were distributed non-randomly within and between ICNs, suggesting that a more appropriate unit of description was the ICNs, themselves, rather than the individual brain regions. To this end, we calculated each ICN's modularity contribution to the network's total modularity, which measures how segregated an ICN is from the rest of the brain, and followed this variable across the lifespan. We found that the modularity of most ICNs decreased with age, suggesting a breakdown of functional specialization. We also characterized changes in brain structural networks, noting that with age hub regions became less efficiently connected to the rest of the brain. Finally, we showed that functional connections between regions separated by many steps (in terms of their structural connectivity) increased with age, while the weight of functional connections between directly connected pairs of regions stayed the same.

In Chapter 3 we investigated changes in the community structure of functional brain networks across the lifespan. We found that, in general, the composition and quality of communities changed with age and that the nature of these changes varied depending upon the scale at which communities were detected. In particular, communities at a coarse scale become more modular (segregated) with age, an effect that was driven mostly by increased modularity of the task-positive system. At this scale, brain regions associated with default mode, control, visual, and

attention networks were highly flexible, especially early in life, and maintain inconsistent allegiances to any single module. Communities defined at a finer scale, on the other hand, become less modular with age, which agrees with the extant literature on age-related changes in community structure. This effect was driven by many communities, but exemplified by communities that included retrosplenial and parahippocampal cortex, which showed large reductions in their overall modularity. Importantly, these areas are related to memory, suggested that age-related changes in memory may be related to their decreased modularity. Collectively, this study highlights the benefits of analyses that examine different organizational scales, demonstrating that lifespan development, from a functional imaging point of view, is an inherently multi-scale process. Furthermore, this study suggests that templates of the brain's functional systems, like those of Power et al (2011) or Yeo et al (2011) that are based on data from healthy adults, may not be a good description of the functional systems from younger or older participants.

Finally, in Chapter 4 we explored the human connectome's tradeoff between geometry and topology using network generative models. Our aim was to identify wiring rules that give rise to synthetic networks that have many properties in common with the human connectome. We found, in agreement with earlier models of non-human connectome data (da F Costa et al 2007) that geometry has a massive influence on the organization of brain networks. Also in agreement with earlier work, however, we found that geometry alone is not sufficient for explaining brain network organization (Kaiser & Hilgetag 2006; Vértes et al 2012). We then set about searching for the wiring rule that incorporates a combination of geometric and non-geometric constraints that was able to produce the most realistic synthetic networks. This exploration showed that by

incorporating a homophilic attraction component (i.e. a propensity for similar nodes to become connected) along with geometric constraints we were able to reproduce a large number of the connectome's properties. Additionally, we fit these models to a lifespan dataset and demonstrated that the parameter governing the strength of the geometric constraints weakened with age, suggesting that later in life, the connectome's links are configured less along the lines of geometric relationships and, possibly, more along the lines of some unknown non-geometric relationships. This final component highlighted the utility of generative models for investigating individual differences between participants.

## **5.2 Limitations**

The studies described in this thesis used processing strategies and analysis tools in line with the current state of the art. Despite this, there are a number of limitations that should be discussed.

The first limitation is related to the subject motion. Virtually all of the data analyzed in this thesis was in the form of MRI data. MRI is ubiquitous to cognitive neuroscience as it allows for non-invasive imaging of human brain activity and structure. In network neuroscience we use these measurements to reconstruct brain functional and structural networks which we then analyze. The process of reconstructing brain networks from MRI data is inherently complicated and can be biased in many ways. Head motion plays a particularly insidious role in the reconstruction of functional brain networks, giving rise to systematic artifactual correlation patterns (Power et al 2012). The effect of motion on structural brain networks is not as well understood, but it surely plays an important role, as well (Tournier et al 2011). This is an especially troublesome problem for studies involving populations where motion is one of the symptoms (e.g. Parkinson's

disease). Motion, of course, also varies across the human lifespan. In the case of all the studies described in this dissertation, we dealt with motion using fairly standard procedures, which included regressing out the translational and rotational parameters (and their derivatives) from a head motion model as well as tracking and controlling for frame-wise displacement patterns (Xu et al 2014). In addition to addressing motion-related issues in the processing our MRI data, we also tried to reduce its effect at subsequent stages of analysis by including estimates of mean framewise displacement (a measure of head motion amplitude) as a nuisance variable in linear regression analysis. While these steps may not completely eliminate the possibility that our conclusions are biased by participants' head motion, they are in line with the soundest approaches available to the field.

In addition to variations in motion amplitude, aging is associated with differential changes in brain structure and volume (Sowell et al 2003). Such changes can be problematic in that the parcellation templates used to divide the cortex into regions of interest are usually developed with a specific age group in mind. For example, the template presented by Yeo et al (2011), which was used in all three middle chapters, was constructed based on functional connectivity data from a massive cohort of 1000 college-aged participants. Consequently, it is unclear whether the same template can be applied to older or younger individuals with the expectation that it still represents a “good” parcellation. While generating a set of own age-specifics template was beyond the scope of this thesis (though some already exist; see Richards et al 2015), we attempted to mitigate concern over the appropriateness of the Yeo template for our data by reproducing our main findings using a different parcellation (Chapter 3).

A final concern is related to the reliability of diffusion imaging and tractography for the reconstruction of anatomical/structural brain networks. These processes are non-invasive, which make them suitable for use with human participants, but for the same reason are also prone to errors. Recent work has raised questions regarding the efficacy of tractography algorithms in detecting known white-matter fiber tracts, concluding that no single tractography algorithm is capable of detecting all classes of connections (Thomas et al 2014). Most tractography algorithms also track streamlines from superficial grey matter sources through deep white matter to gray matter targets. A recent study demonstrated the presence of thin white matter tracts running parallel to the cortical surface that are never taken into account during tractography (Reveley et al 2015). Future work in the area of brain network construction will surely address these and other, perhaps unanticipated, shortcomings.

### **5.3 Future work**

The work presented in this dissertation lays the ground for potential future work. In Chapter 2, for instance, we used mass univariate-testing to identify functional connections and ICNs that exhibited change with age. Such an approach necessarily ignores multivariate changes – i.e. groups of connections that collectively vary with age. Technique like partial least squares (PLS) (McIntosh and Mišić 2013), on the other hand, can naturally extract such groups and represents an extension of the work presented in that chapter. Indeed, there are many reasons why multivariate approaches should be preferred over the mass-univariate approach initially used in Betzel et al (2014). Perhaps the most striking is that the mass-univariate approach, which models the lifespan trajectory of each functional connection, assumes that the connections are independent of one another. Of course, this is not the case; the connection weights are estimated

using correlation coefficients. For any three nodes, A, B, and C, the correlations of A with B and B with C places a bound on the extent to which A and C are correlated, meaning that the coefficients are not independent of one another and should probably not be modeled as if they were. Multivariate methods, on the other hand, usually do not make this same assumption, and future work should investigate to what extent such methods can reproduce the results of Betzel et al (2014).

In Chapter 4 we focus on generative models of the human connectome. This topic represents the most extendable work presented in this thesis. The generative model in this chapter was, by design, probabilistic, and the probability of forming any connection was governed by spatial proximity and some additional information about the topology of the network. We explored thirteen possible definitions for what this additional information could represent, though there are many more alternative possibilities that we did not explore (e.g. length of shortest path or communicability (Estrada & Hatano 2008) between two regions, etc.). It may be the case that one or more of these alternative definitions outperforms those explored in that chapter. Our models also did not functional developmental models of the human connectome – we looked for wiring rules that compressed the connectome’s description length. It would be interesting to incorporate neurobiological parameters into the model (see Nicosia et al 2013 for an example with *C. elegans*) to determine the extent to which a more realistic model improves the overall fit.

Another interesting extension of the generative models is related to discovering individual differences in connectome organization. We showed that, across the lifespan, the parameter governing spatial constraints weakened monotonically; it may be informative to use these

generative models to explore neuro-psychiatric disorders, such as schizophrenia, in which network organization appears to be disrupted (van den Heuvel & Fornito 2014). Similar approaches have been taking using models of brain functional networks (Vértes et al 2012).

In this same chapter we showed that, given the embedding of brain regions in Euclidean space, geometric (spatial) models failed to reproduce many of the human connectome's properties. An interesting theoretical exercise would be to determine a new embedding of brain regions (choose new coordinates for each node), thereby enabling a spatial model to reproduce the observed network. The embedding need not be in Euclidean space; recent work has explored embedding networks in hyperbolic spaces and using their distance relationships in this non-Euclidean space to determine the connection probabilities of a generative model (Krioukov et al 2010; Papadopoulos et al 2012).

#### **5.4 Concluding remarks**

The human lifespan is accompanied by profound changes in cognitive ability, characterized by frailty both early and later in life but also by robustness throughout much of the middle. In this dissertation we show that, in parallel with cognitive change, functional and structural brain networks undergo reorganization. Sometimes these changes are subtle, and include minute (yet systematic) tuning of the connection weights between specific brain regions. Other times these changes appear more overt and obvious, involving entire communities and enveloping whole sub-systems. This dissertation does not explain *why* or *how* such changes occur. Instead, it functions more as an inventory, describing *what* changes and *when*. Further inquiry, perhaps with better imaging technology, is necessary to help address these other questions. Nonetheless, we



outline a number of avenues for future work while being forthright about the limitations of our work. The hope is that the findings presented here can serve as guides for subsequent studies into the effects of age on the organization of brain networks, highlighting research areas of potential interest.

## Figures

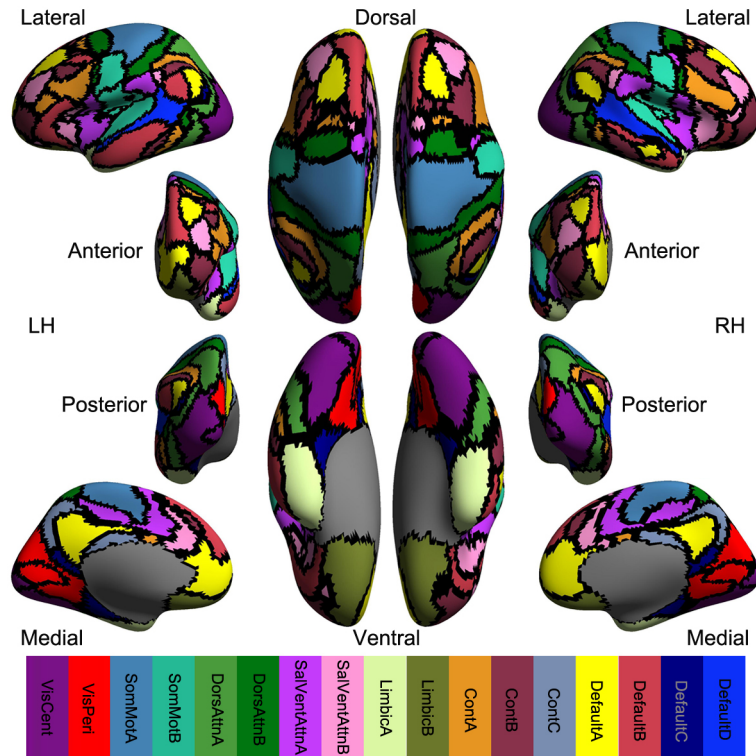


Figure 2.1. Surface rendering of all 17 RSN sub-networks comprising 114 brain regions in total onto both left hemisphere (LH) and right hemisphere (RH). The inflated surfaces are provided by FreeSurfer (*fsaverage*). The cortex is divided into 17 components derived from a total of 7 RSNs (Yeo et al., 2011): control components A, B, and C (ContA, ContB, ContC); default mode components A, B, C, and D (DefaultA, DefaultB, DefaultC, DefaultD); dorsal attention components A, B (DorsAttnA, DorsAttnB); limbic components A, B (LimbicA, LimbicB); saliency/ventral attention components A, B (SalVentAttnA, SalVentAttnB); somatomotor components A, B (SomMotA, SomMotB); visual central (VisCent) and peripheral (VisPeri) components. The colormap indicates colors picturing each of the 17 components and their regions on the surfaces.

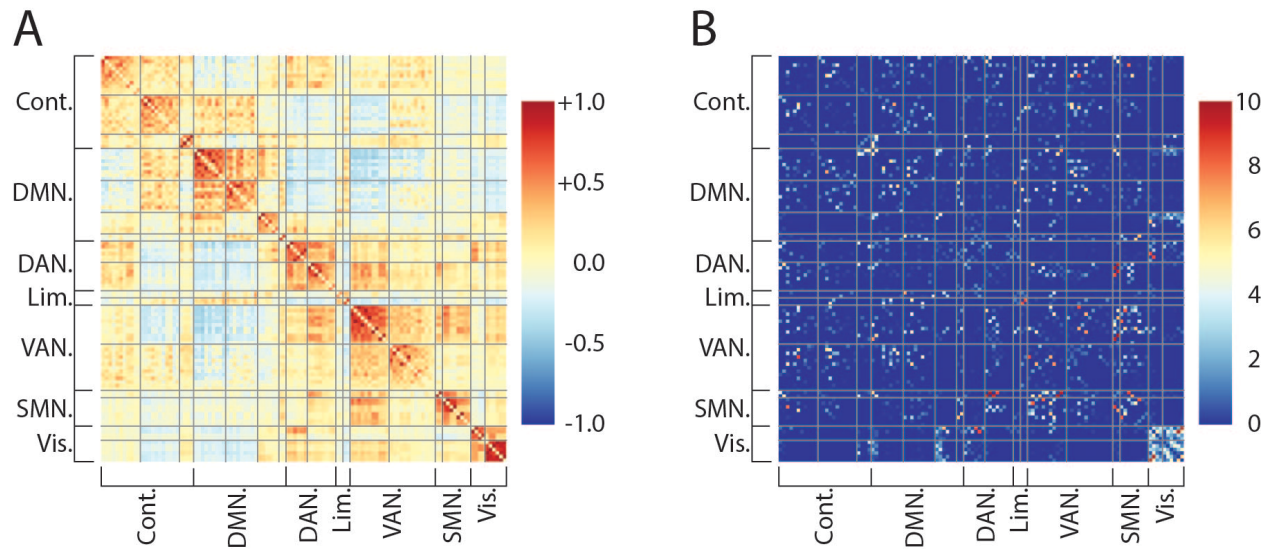


Figure 2.2. Group-averaged (all ages) FC (A) and SC (B) organized according to RSN components. This particular SC matrix was generated by setting  $\gamma = 0.6$ . In panel B, the SC matrix, a connection is shown only if it was present in at least one quarter (32) of all participants.

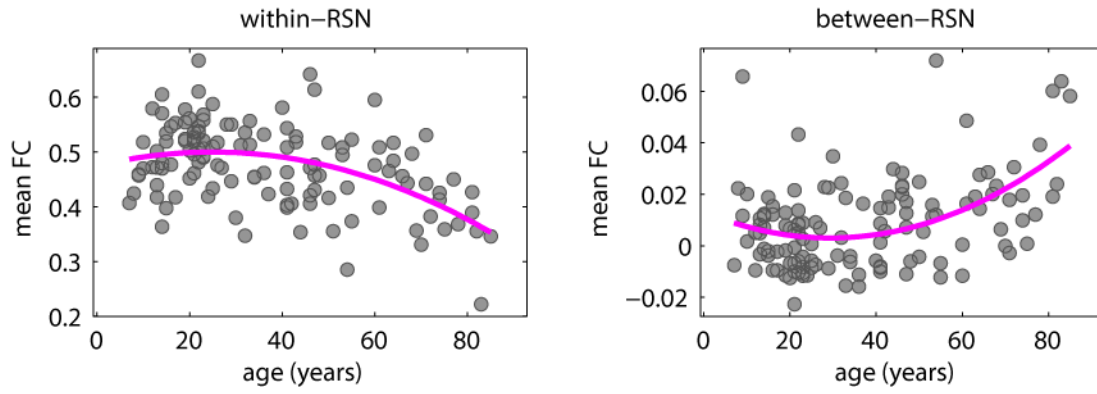


Figure 2.3. Age-related changes in average FC within (left) and between (right) RSN components. Both trajectories are statistically significant at  $p < 0.01$ .

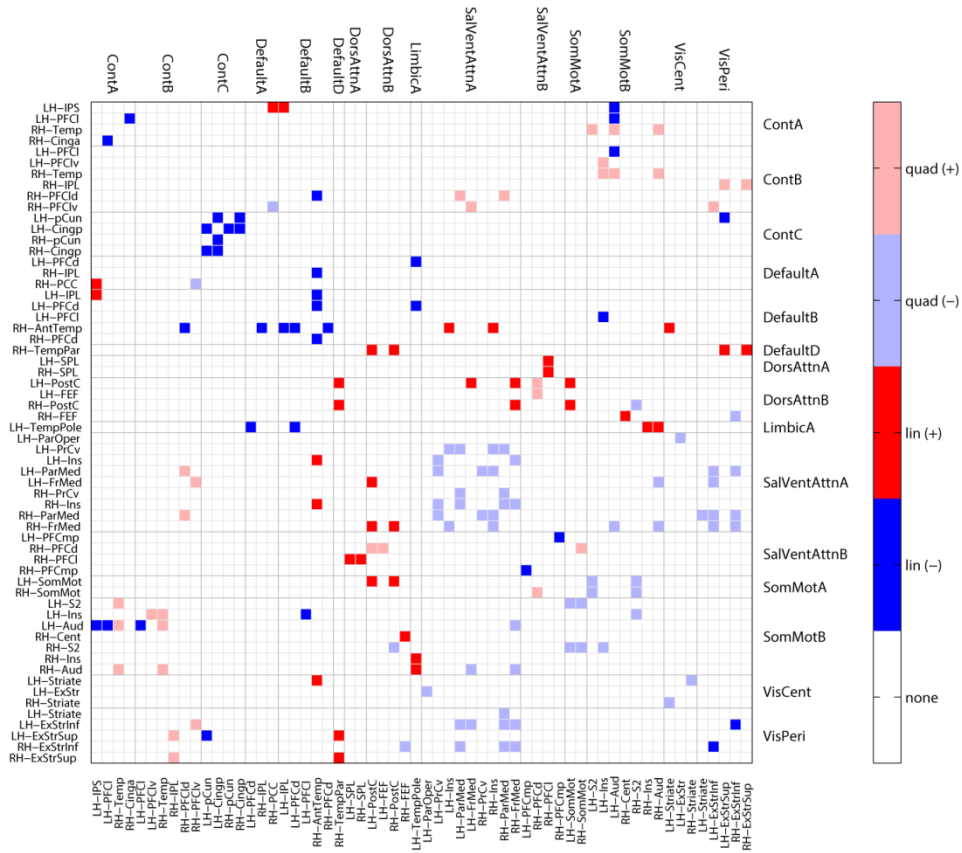


Figure 2.4. Statistically significant MLRs ( $q < 0.01$ , FDR-corrected) fit to individual functional connections. Cell color denotes model order and type: linear increasing (red), linear decreasing (blue), quadratic concave (pink), and quadratic convex (pale blue). See SI Table 1 for MLRs parameters and other details.

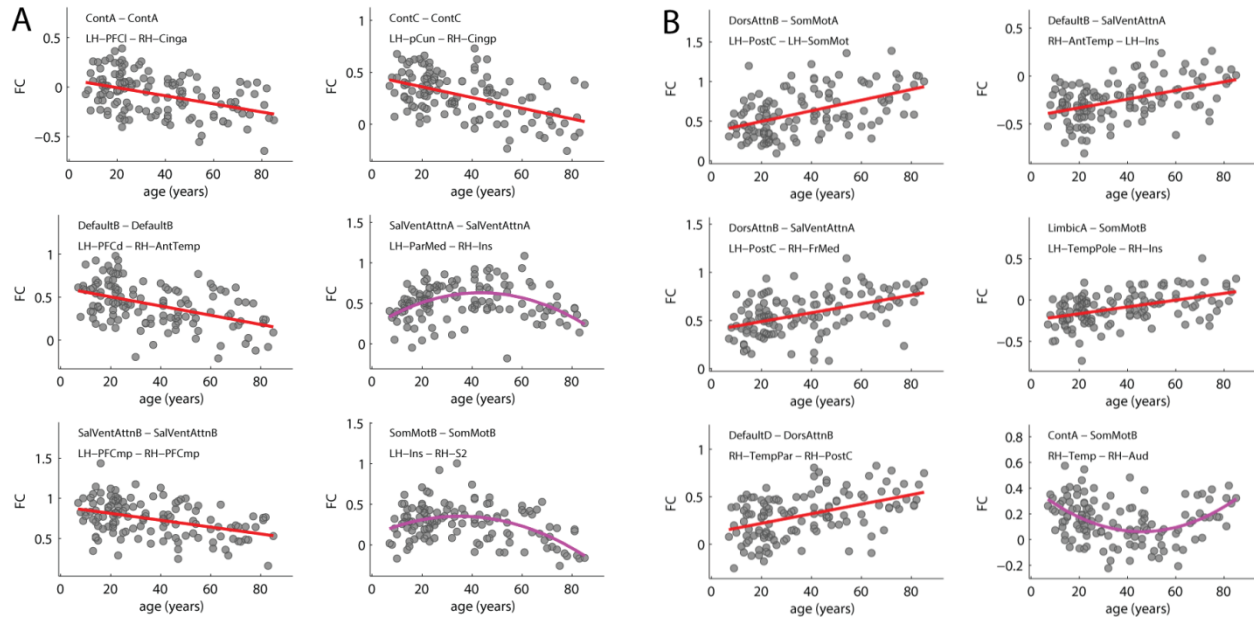


Figure 2.5. Representative examples of age-related changes in within-component FC (A) and between-component FC (B). Gray dots indicate empirical estimates of FC while red lines represent the best-fit line derived from the MLRs. All MLRs passed a statistical threshold of  $q < 0.01$ , FDR-corrected.

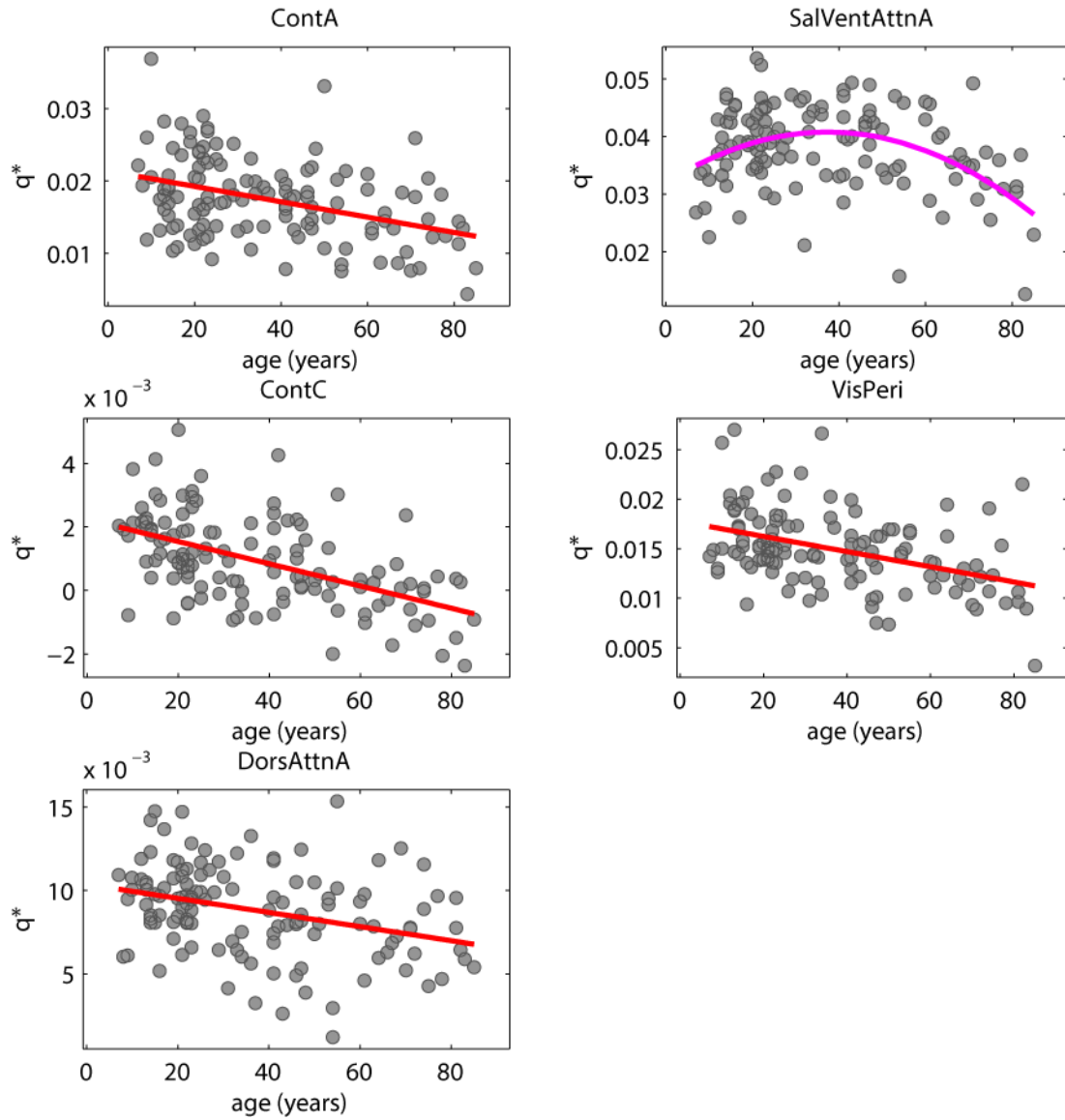


Figure 2.6. Statistically significant MLRs ( $q < 0.01$ , FDR-corrected) fit to individual RSN component modularity,  $q^*_{RSN}$ . See SI Table 2 for MLRs parameters and other details

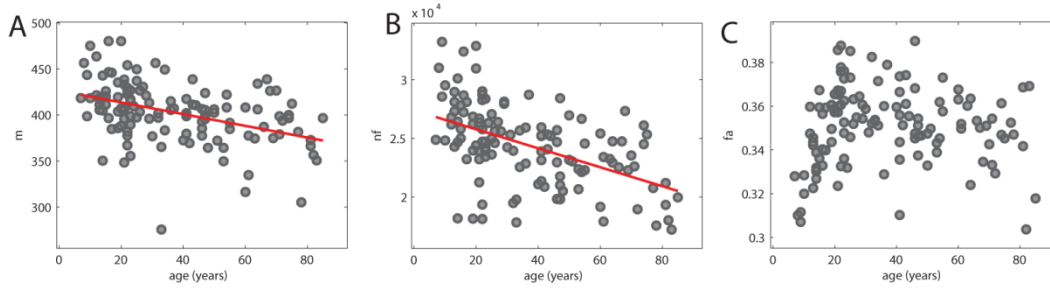


Figure 2.7. Change in global SC parameters as a function of age. (A) number of binary connections,  $m$ ; (B) total fiber count,  $nf$ ; (C) average fractional anisotropy,  $fa$ .



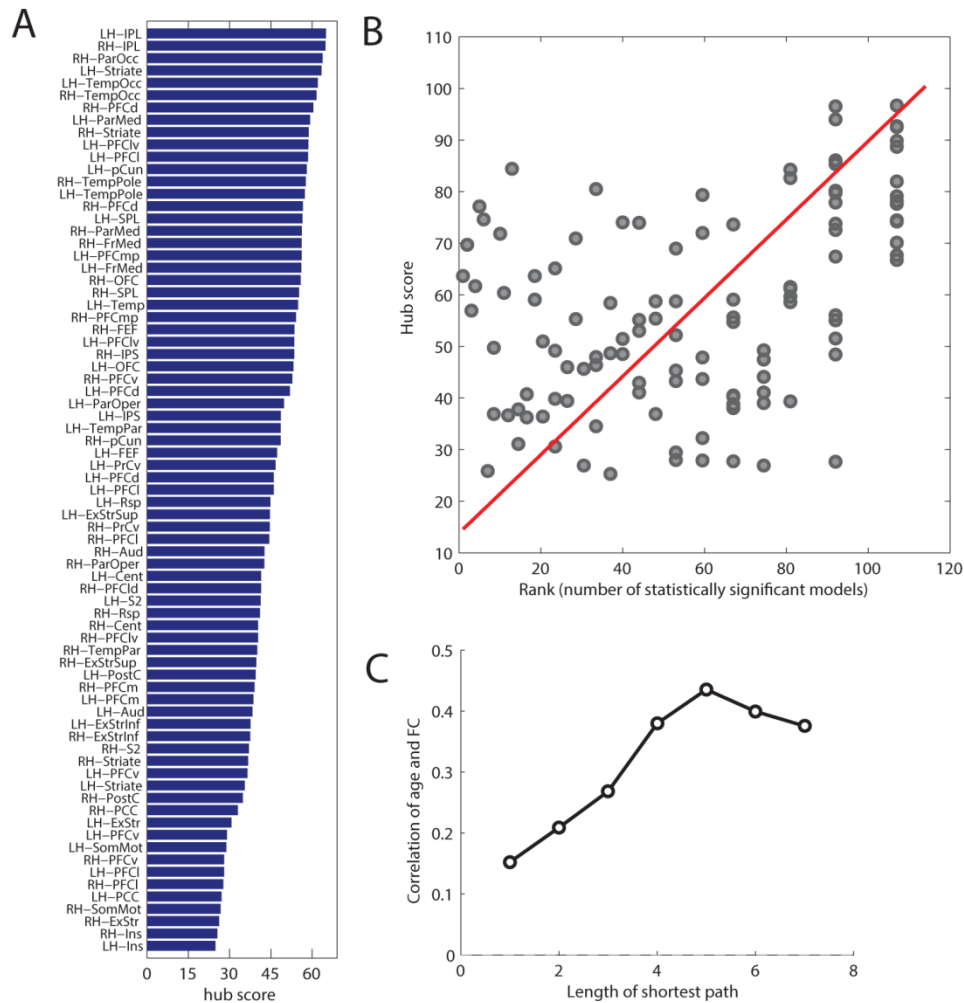


Figure 2.8. (A) The average hub scores of the 75 most hub-like regions; (B) A rank-wise scatterplot of hubness as a function of the number of statistically significant models a region participates in; (C) The black line indicates the magnitude of the age by FC correlation of all edges at a given topological distance; the red bars indicate the cumulative percent of all paths less than or equal to a given topological distance. The fraction of all paths with length less than or equal to 7 is 86.6%.

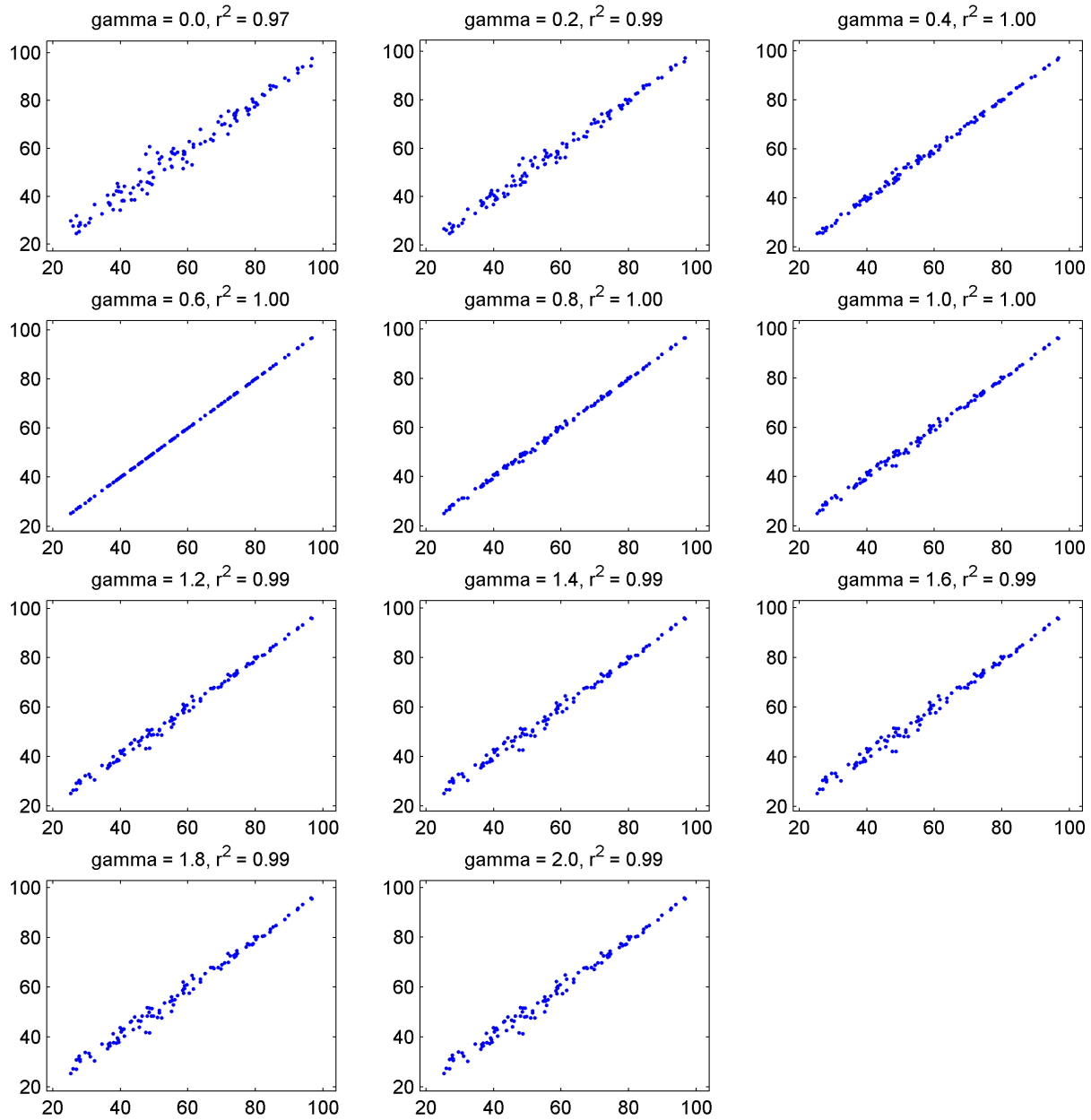


Figure 2.9 (SI Figure 1). Scatter plots of hub scores at all values of  $\gamma$  with hub scores when  $\gamma = 0.6$ . The smallest  $r^2$  was equal to 0.97, strongly suggesting that a region's “hubness” was consistent across the range of  $\gamma$  tested in this paper.

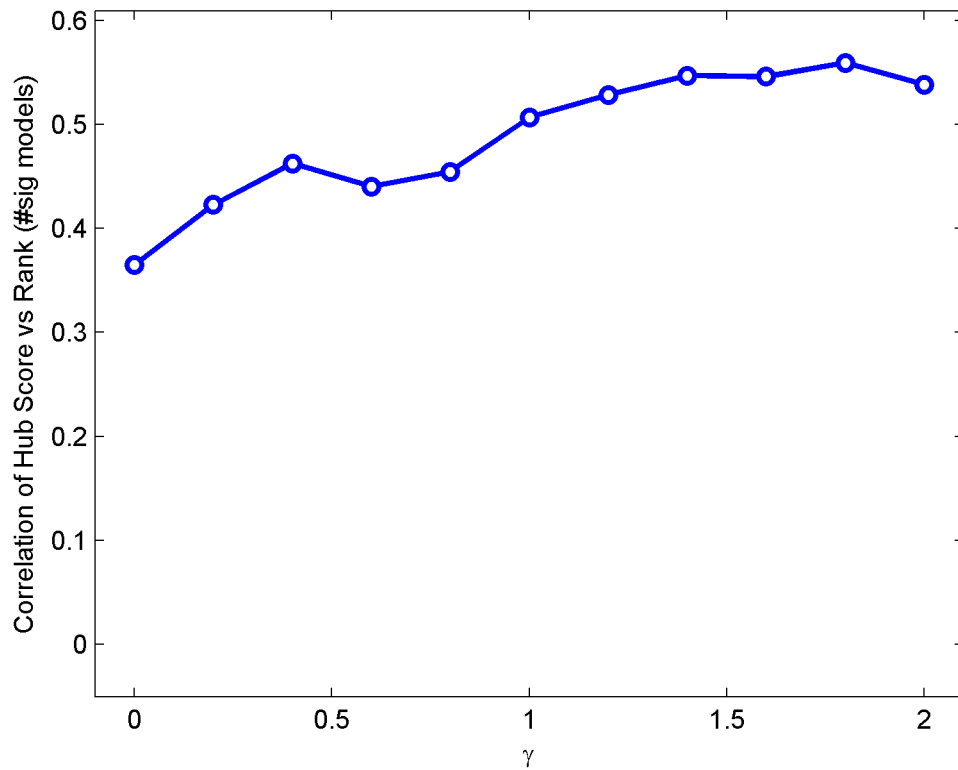


Figure 2.10 (SI Figure 2). Correlation coefficient of regional “hub score” with the “number of statistically significant models that a region participates in” calculated across the full range of  $\gamma$ . All correlations are statistically significant after FDR corrections (maximum  $p$ -value across all  $\gamma$  values was  $p \sim 10^{-4}$ ).

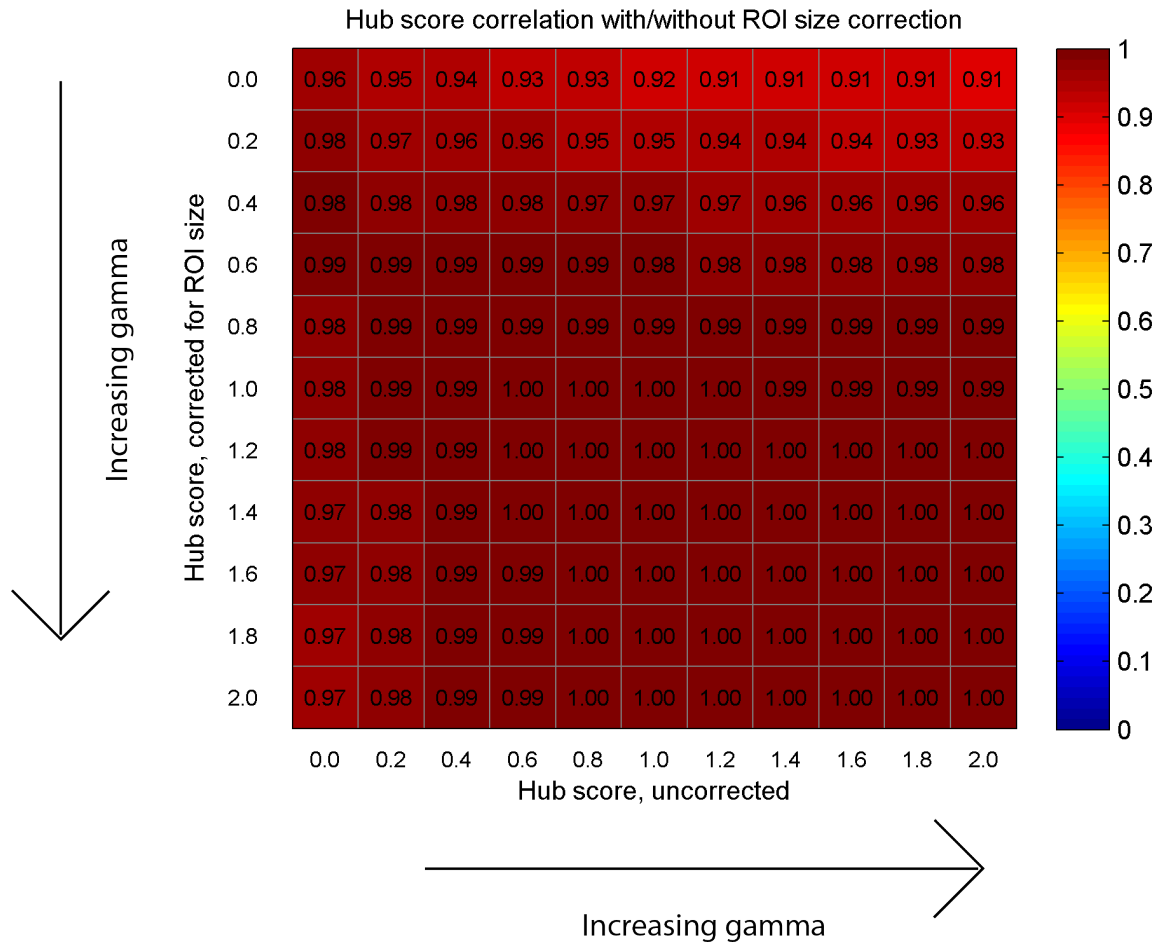


Figure 2.11 (SI Figures 3). Hub scores are consistent irrespective of whether edge weights are corrected for ROI size. Hub scores were calculated for SC networks where edge weights were corrected for ROI size, i.e.  $a_{ij}^{wei} = (FA_{ij} \times NF_{ij}^{\gamma}) / (V_i + V_j)$ , and also without the ROI size correction. Shown here is the Pearson correlation for every pair of corrected/uncorrected hub scores. Note that the minimum correlation coefficient is  $r = 0.91$ , suggesting that hub scores are consistent across different weighting schemes.

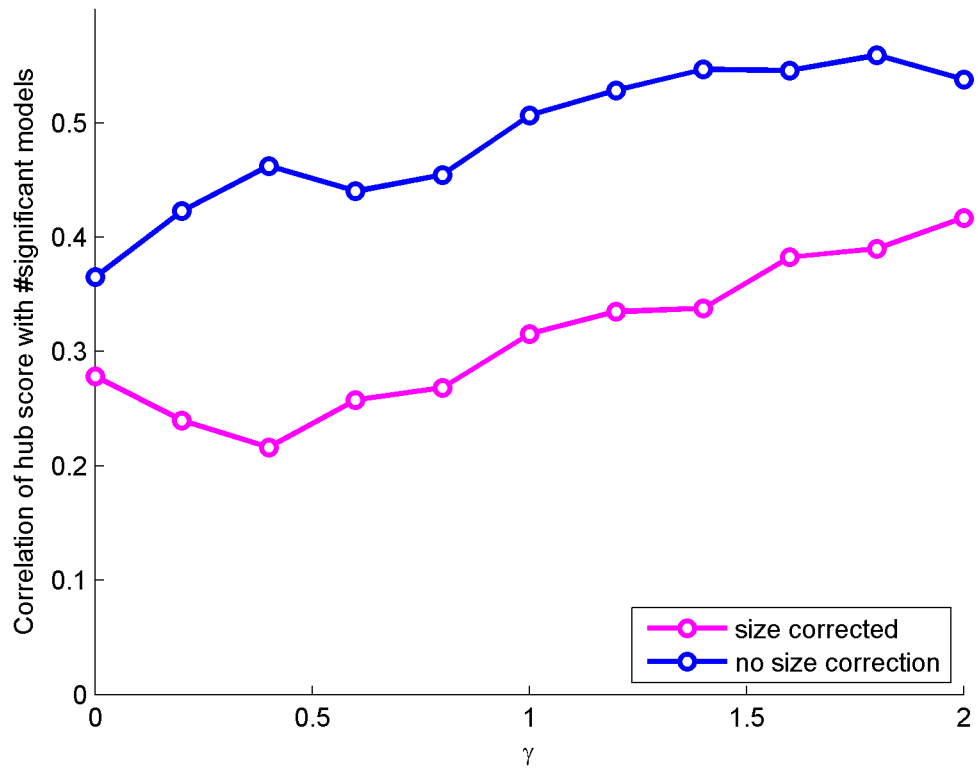


Figure 2.12 (SI Figure 4). Correlation coefficient of regional “hub score” with the “number of statistically significant models that a region participates in” calculated across the full range of  $\gamma$  both with/without ROI size correction. Note that the correlation magnitude weakens as a results of correcting for ROI size, but the overall positive correlation of these two variables is preserved.

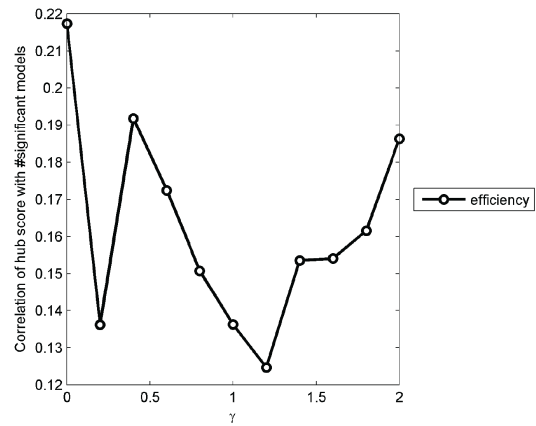
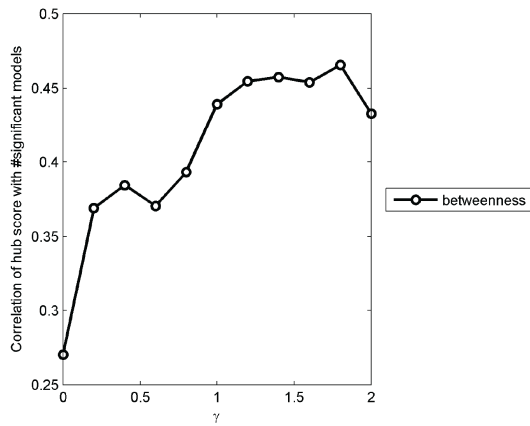
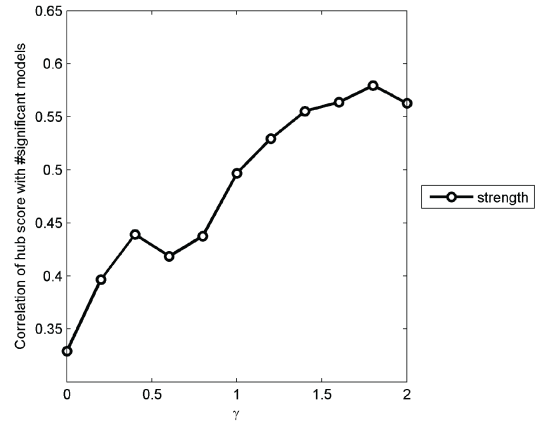
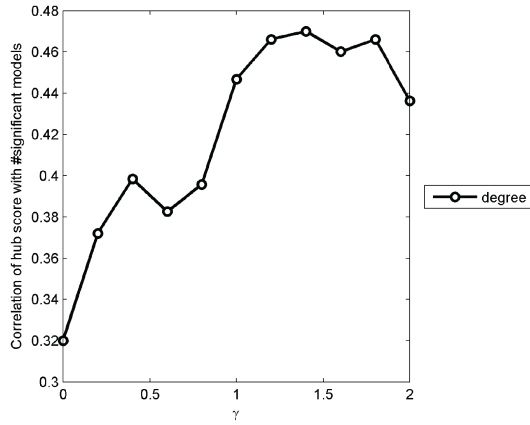


Figure 2.13 (SI Figure 5). Effect of alternative hub definitions on “hub score” and “number of statistically significant models that a region participates in” correlation. The correlation is preserved when hubs are defined based on degree, strength, or betweenness but not when they are defined based on local efficiency alone.

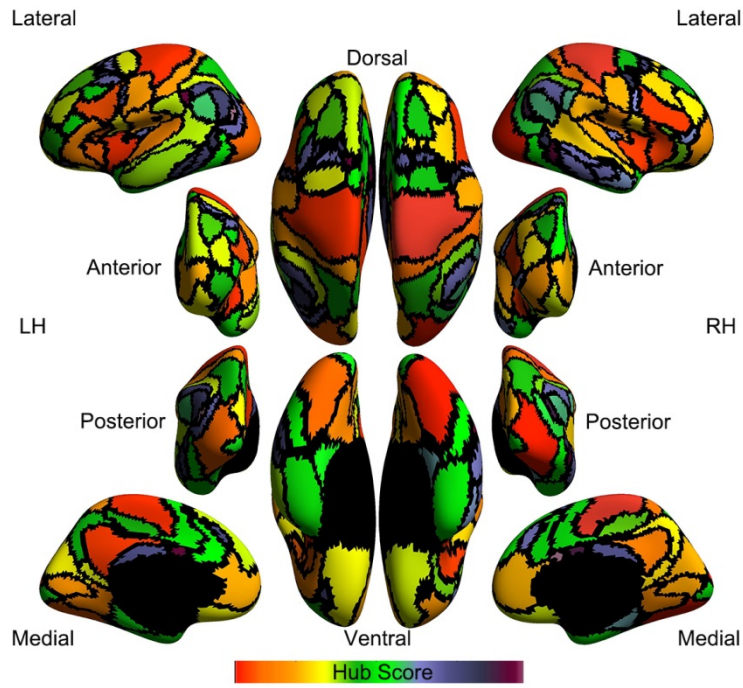


Figure 2.14 (SI Figure 7). Topographic map of cortical surface colored according to hub score. Small hub scores (red) indicate that a node was more hub-like in that it had high node degree, node strength, local efficiency, and betweenness centrality. Large hub scores (purple) indicate less hub-like nodes.

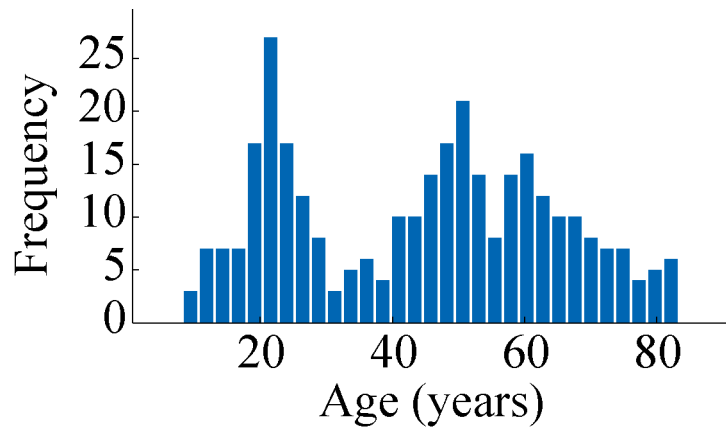


Figure 3.1. Distribution of participant ages for NKI-Rockland sample.



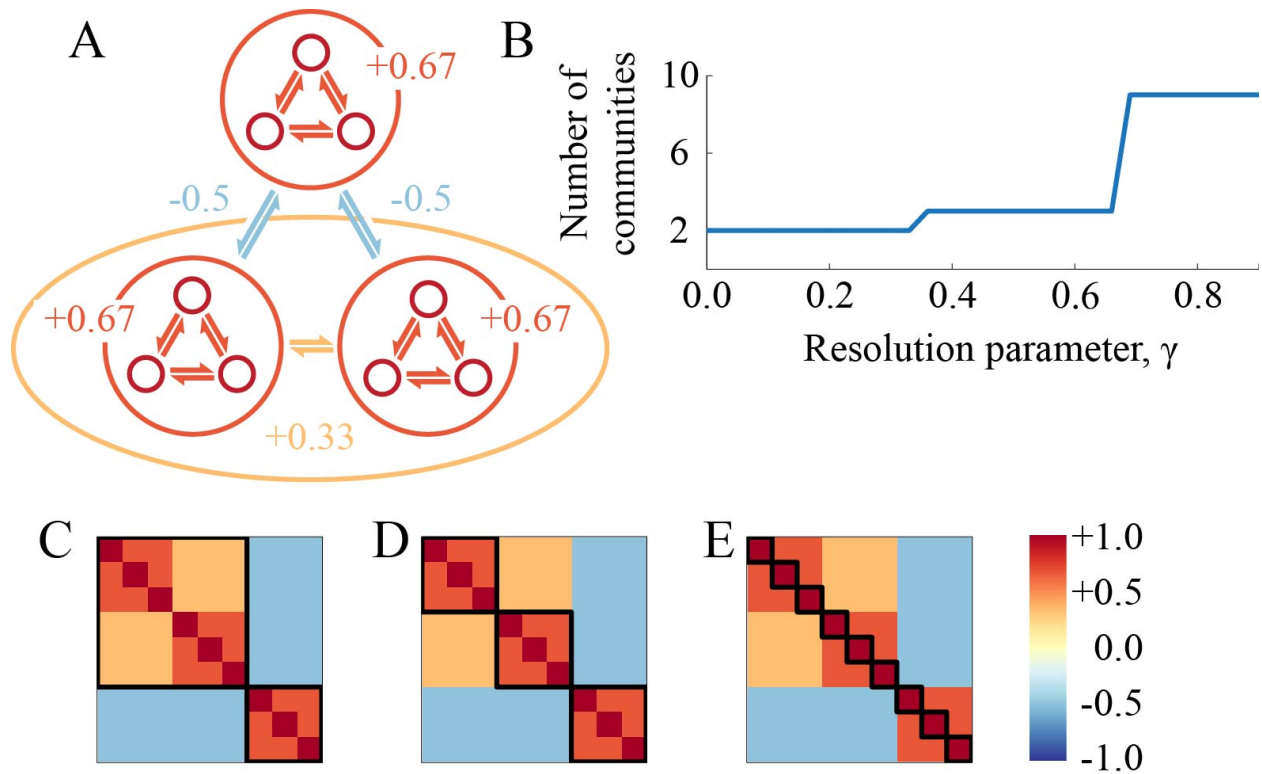


Figure 3.2. Illustration of multi-scale community structure using a toy correlation matrix. (A) Schematic showing three distinct scales of communities. There are nine small communities (red circles), which can be aggregated into three medium-sized communities (orange circles), two of which can be further aggregated into a larger community (beige ellipse). We used modularity maximization and varied the resolution parameter,  $\gamma$ , to identify communities. Panel (B) shows the number of communities detected over the range  $\gamma \in [0.0, 0.9]$ . Over this range we find three sets distinct partitions, corresponding to the two-, three-, and nine-community divisions. Panels (C-E) show these divisions superimposed on the toy correlation matrix.

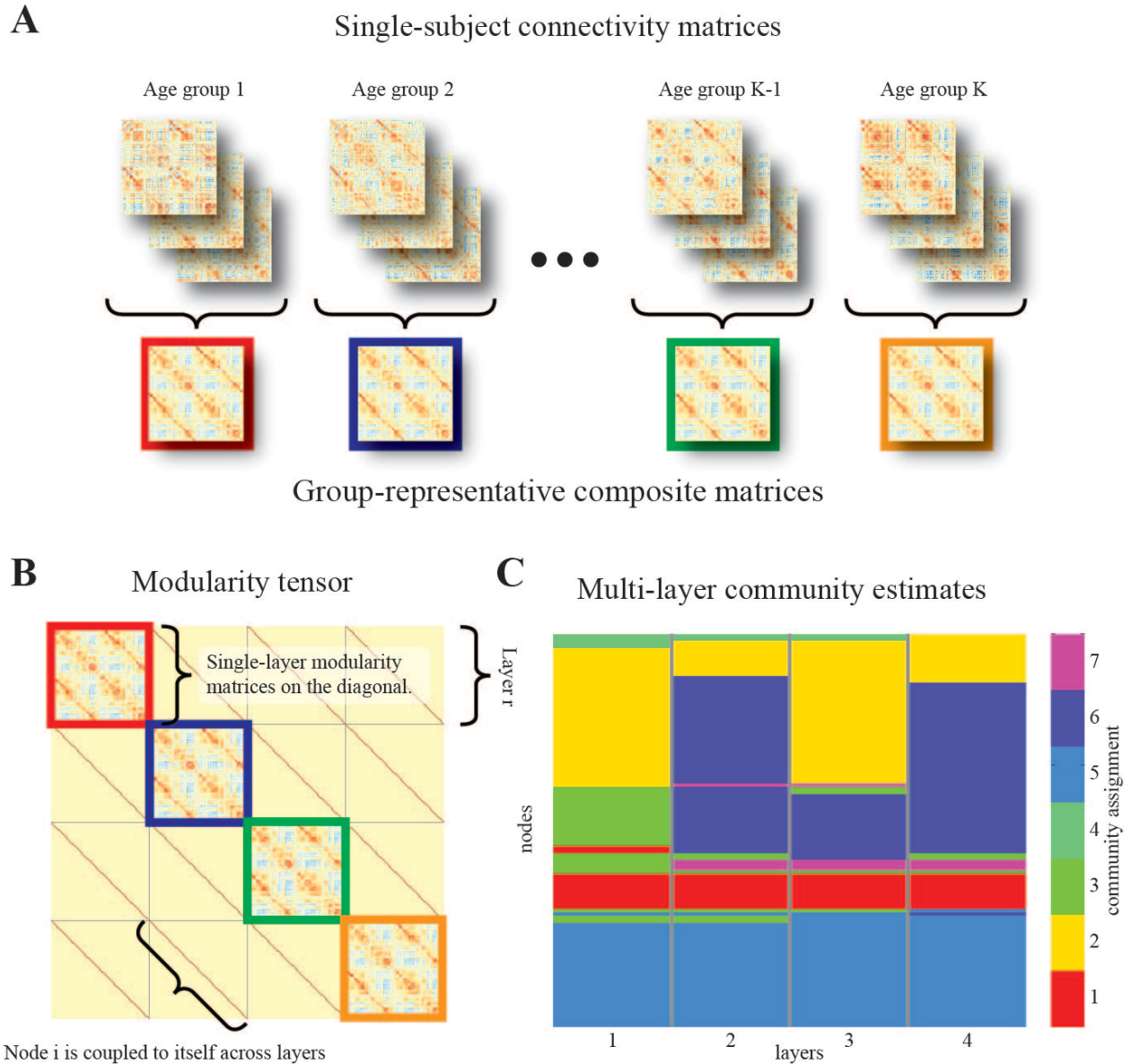


Figure 3.3. Schematic diagram illustrating workflow. (A) Individual participants are assigned to one of  $K$  age groups where membership is determined by percentiles. Based on sub-samples of the subjects assigned to any group, a representative connectivity matrix is constructed. Representative matrices are shown here outlined in red, purple, green, and orange. (B) The representative matrices are modeled as the layers of multi-layer network whose modularity is maximized using a community detection algorithm. (C) The community detection algorithm

returns a community assignment for nodes in each layer, where the community labels are consistent across layers.

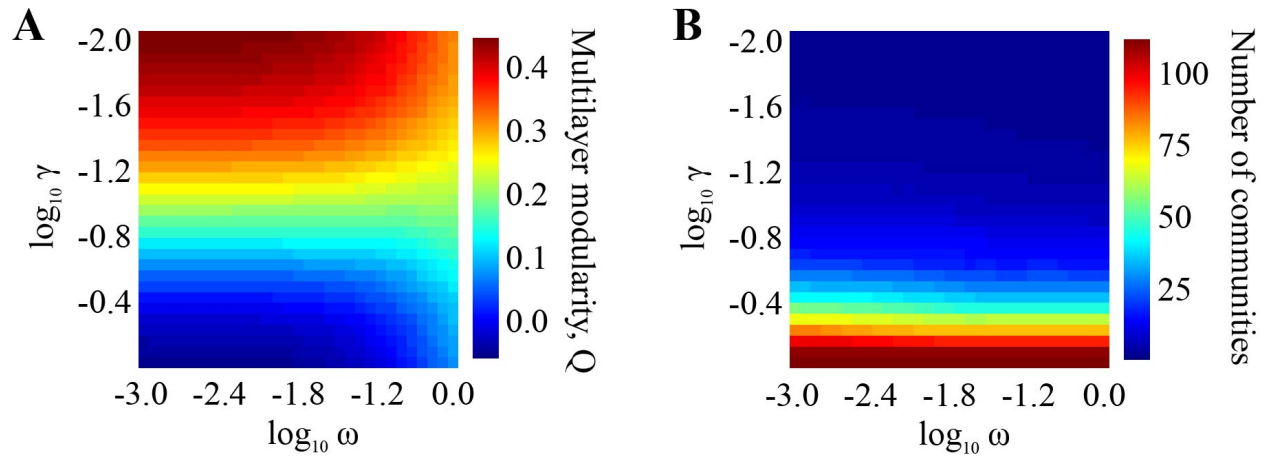


Figure 3.4. Outputs from the multilayer modularity maximization procedure. (A) Modularity landscape as a function of  $\gamma$  and  $\omega$ . (B) Number of communities obtained from partitions. Note that in both panels the axes are log transformed.

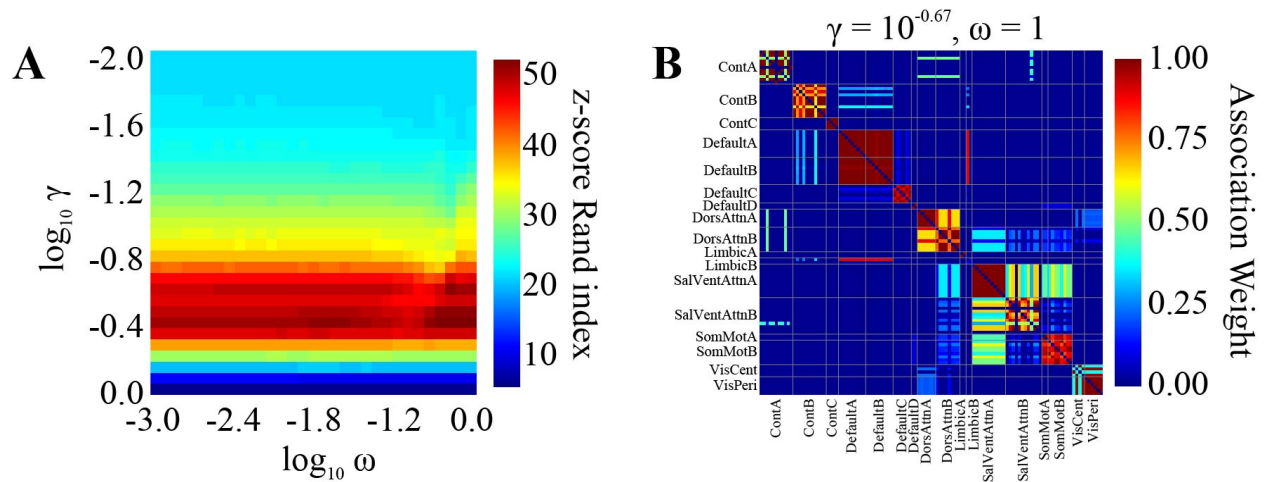


Figure 3.5. Comparison of detected communities to Yeo2011 ICNs. (A) Z-score Rand indices as a function of  $\omega$  and  $\gamma$ . Each multilayer partition was decomposed into a set of single-layer partitions in order to compare community assignments with the Yeo partition. (B) Association matrix comparing single-layer communities and Yeo ICN assignments.

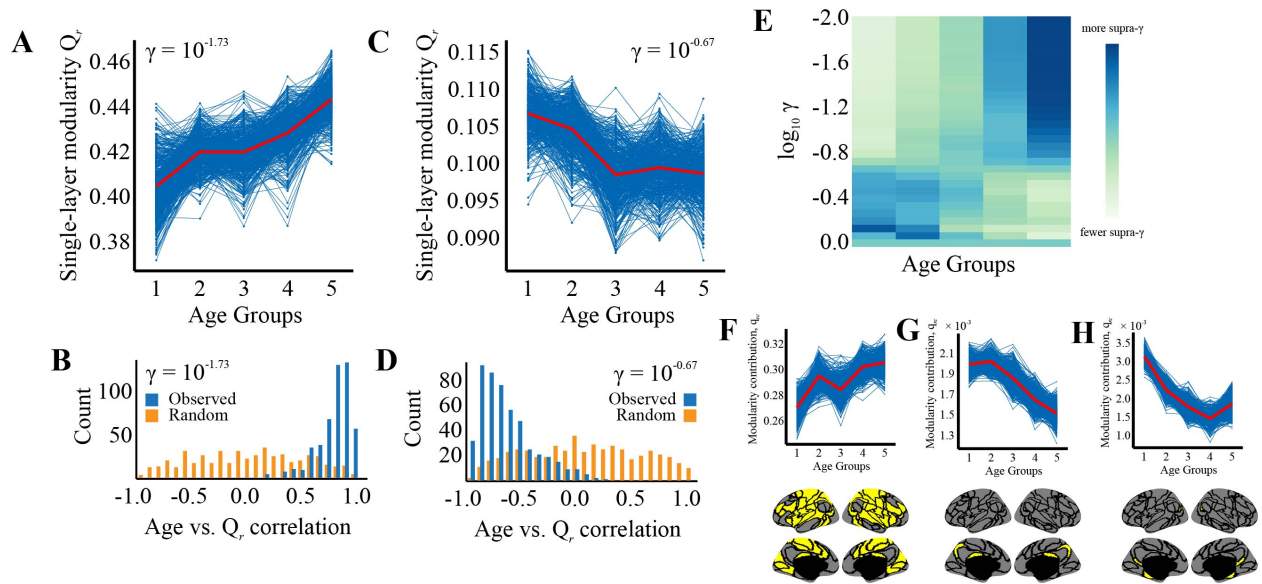


Figure 3.6. Single-layer modularity,  $Q_r$ , follows distinct age-related trajectories at different levels of  $\gamma$ . All panels in this figure are plotted with  $\omega = 10^{-1.5}$ . (A) When  $\gamma = 10^{-1.73}$  the value of  $Q_r$  increases linearly with age. Trajectories corresponding to individual samples are shown in blue while the mean trajectory is shown in red. (B) The correlation of age and  $Q_r$  was calculated for each sample and the distribution of those coefficients (shown here in blue) was compared against a null model (shown in orange). (C) Increasing the resolution parameter to  $\gamma = 10^{-0.67}$  leads to a regime where  $Q_r$  decreases with age. (D) Distribution of correlation coefficients compared to null model. (E) As a function of  $\gamma$  we calculated the number of connections that exceed  $\gamma$  and ranked each layer. When  $\gamma$  is small, older layers contain the greatest number of supra connections. Increasing  $\gamma$  reverses this relationship. (F) Modularity contribution of the community that drives the relationship in panel (A) and the topographic boundary of that community. (G-H) Modularity contribution of the communities that drive the relationship in panel C and their topographic boundaries.

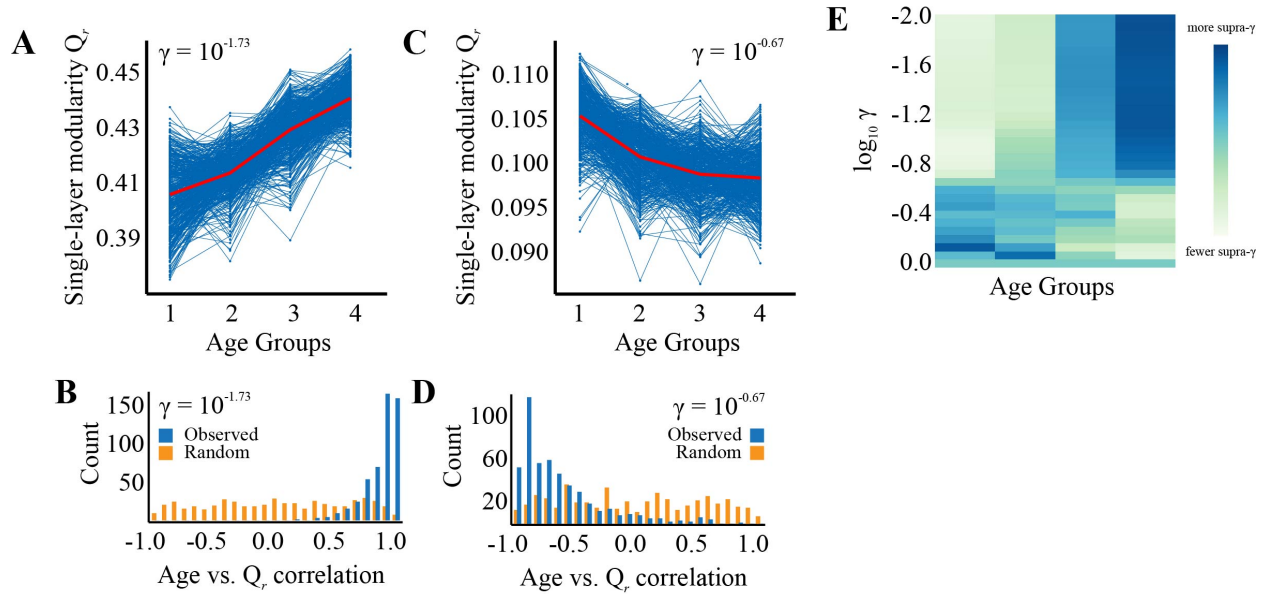


Figure 3.7. In the main text, we focused on a division of the lifespan into  $K = 5$  age groups, though we also repeated our analyses for  $K = 4$ ,  $K = 6$ , and  $K = 7$ . In general, these results were in line with those presented in the main text. In Figures 3.7-3.9, we reproduce the main finding of this paper, namely that the relationship of age and the modularity of functional brain networks is scale-dependent. In Figures 3.15-3.17 we also show that the flexibility analysis presented in the main text can be reproduced with  $K = 4$ ,  $K = 6$ , and  $K = 7$  age groups.

While the results of analyses based on these age groups are largely the same as those obtained when  $K = 5$ , there are some notable differences. For example, as we increase the number of groups, we can resolve age-related flexibility in greater detail. When  $K = 6$  or  $K = 7$  and when communities are defined at a fine level ( $\gamma = 10^{-0.67}$ ), the first transitions are actually less flexible than expected, contrary to the greater-than-expected flexibility when  $K = 4$  or when  $K = 5$ .

Single-layer modularity,  $Q_r$ , follows distinct age-related trajectories at different levels of  $\gamma$  with  $K = 4$  (sample mean $\pm$ standard deviation age of groups are  $18.9\pm 4.0$ ,  $36.2\pm 7.8$ ,  $53.1\pm 3.8$ , and  $69.4\pm 6.8$  years). (A) When  $\gamma = 10^{-1.73}$  the value of  $Q_r$  increases linearly with age. Trajectories corresponding to individual samples are shown in blue while the mean trajectory is shown in red. (B) The correlation of age and  $Q_r$  was calculated sample and the distribution of those coefficients (shown here in blue) was compared against a null model (shown in orange) (t-test,  $df = 998$ ,  $t = 32.46$ ). (C) Increasing the resolution parameter to  $\gamma = 10^{-0.67}$  leads to a regime where  $Q_r$  decreases with age. (D) Distribution of correlation coefficients compared to null model (t-test,  $df = 998$ ,  $t = -20.46$ ). (E) As a function of  $\gamma$  we calculated the number of connections that exceed  $\gamma$  and ranked each layer. When  $\gamma$  is small, older layers contain the greatest number of supra- $\gamma$  connections. Increasing  $\gamma$  reverses this relationship.



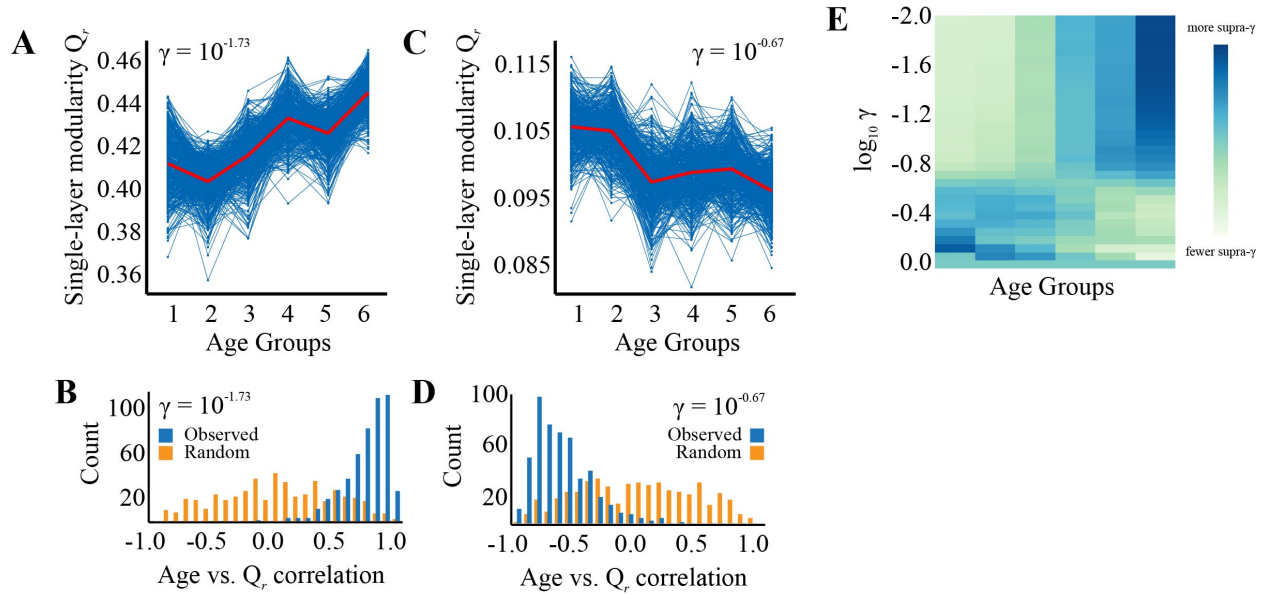


Figure 3.8. Single-layer modularity,  $Q_r$ , follows distinct age-related trajectories at different levels of  $\gamma$  with  $K = 6$  (sample mean $\pm$ standard deviation age of groups are  $17.1\pm 3.7$ ,  $24.7\pm 2.4$ ,  $40.9\pm 4.7$ ,  $50.7\pm 2.0$ ,  $60.0\pm 2.7$ , and  $72.9\pm 5.4$  years). (A) When  $\gamma = 10^{-1.73}$  the value of  $Q_r$  increases linearly with age. Trajectories corresponding to individual samples are shown in blue while the mean trajectory is shown in red. (B) The correlation of age and  $Q_r$  was calculated sample and the distribution of those coefficients (shown here in blue) was compared against a null model (shown in orange) (t-test,  $df = 998$ ,  $t = 32.92$ ). (C) Increasing the resolution parameter to  $\gamma = 10^{-0.67}$  leads to a regime where  $Q_r$  decreases with age. (D) Distribution of correlation coefficients compared to null model (t-test,  $df = 998$ ,  $t = -26.73$ ). (E) As a function of  $\gamma$  we calculated the number of connections that exceed  $\gamma$  and ranked each layer. When  $\gamma$  is small, older layers contain the greatest number of supra- $\gamma$  connections. Increasing  $\gamma$  reverses this relationship.

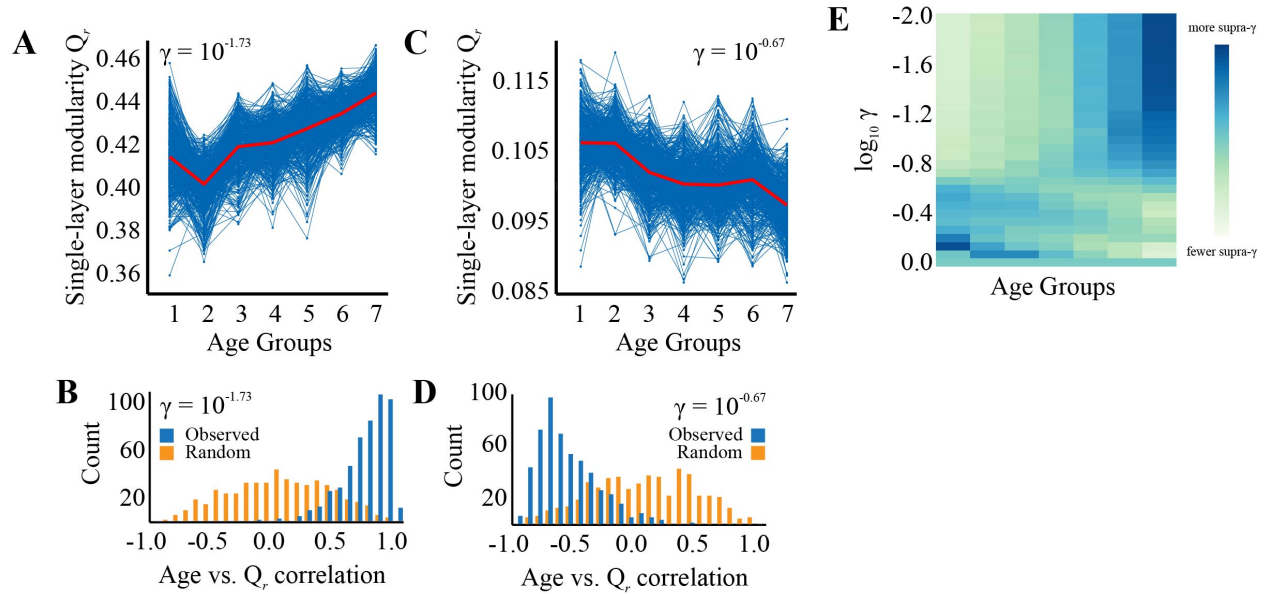


Figure 3.9. Single-layer modularity,  $Q_r$ , follows distinct age-related trajectories at different levels of  $\gamma$  with  $K = 7$  (sample mean $\pm$ standard deviation age of groups are  $16.4\pm 3.6$ ,  $23.0\pm 1.6$ ,  $34.4\pm 5.7$ ,  $46.9\pm 2.2$ ,  $53.7\pm 2.6$ ,  $62.1\pm 2.6$ , and  $74.1\pm 5.0$  years). (A) When  $\gamma = 10^{-1.73}$  the value of  $Q_r$  increases linearly with age. Trajectories corresponding to individual samples are shown in blue while the mean trajectory is shown in red. (B) The correlation of age and  $Q_r$  was calculated sample and the distribution of those coefficients (shown here in blue) was compared against a null model (shown in orange) (t-test,  $df = 998$ ,  $t = 34.60$ ). (C) Increasing the resolution parameter to  $\gamma = 10^{-0.67}$  leads to a regime where  $Q_r$  decreases with age. (D) Distribution of correlation coefficients compared to null model (t-test,  $df = 998$ ,  $t = -29.52$ ). (E) As a function of  $\gamma$  we calculated the number of connections that exceed  $\gamma$  and ranked each layer. When  $\gamma$  is small, older layers contain the greatest number of supra- $\gamma$  connections. Increasing  $\gamma$  reverses this relationship.

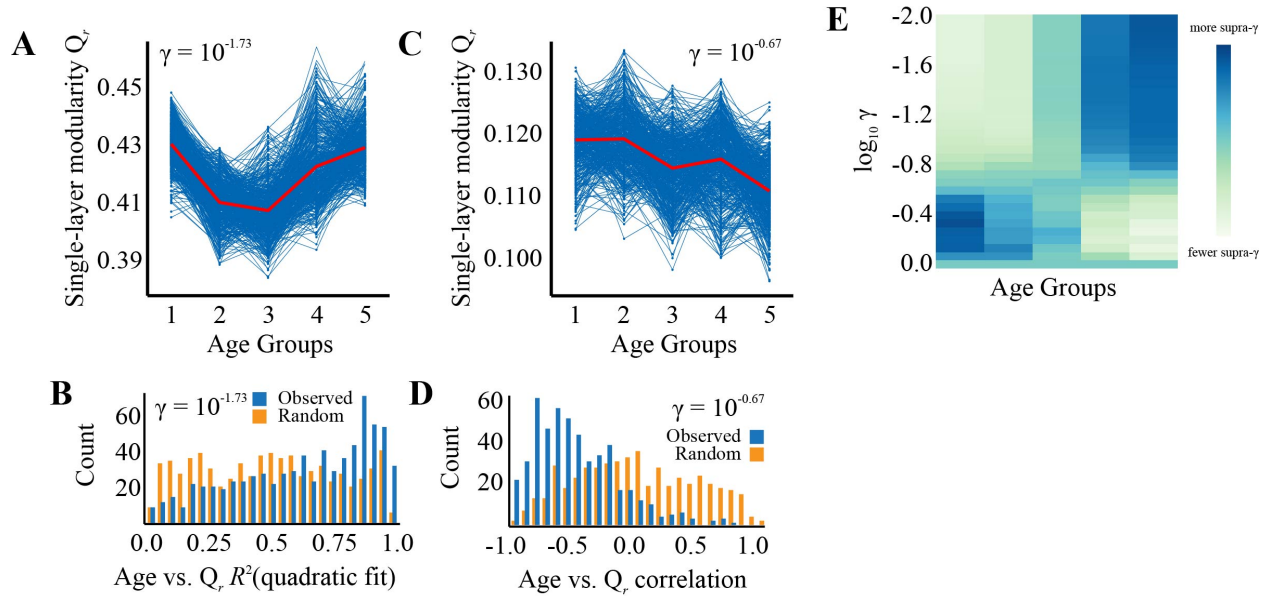


Figure 3.10. In the main text we present results based on analyses of connectivity matrices where nodes were defined according to a functional parcellation (Yeo et al 2011). The use of a functional parcellation in a functional connectivity analysis is sometimes preferred over convolution-based parcellations, as the regions tend to be more functionally homogeneous (Gordon et al 2014). However, to demonstrate the robustness of our findings, we replicated our analyses using a convolution-based atlas (Destrieux et al 2010). In Figure 3.10 we show a figure analogous to Figure 3.6 in the main text. In line with the results presented in the main text, we find that modularity exhibits scale-dependent age-related changes. With this parcellation, however, modularity exhibits a u-shaped trajectory when  $\gamma$  was small (the  $R^2$  of a quadratic model fit to the observed data is statistically greater than a similar model fit to randomized data; t-test with  $df = 998$ ,  $t = 7.83$ ,  $p \approx 10^{-14}$ ); modularity still decreases approximately linearly with age at larger values of  $\gamma$  and the strength of this linear correlation is greater than that of a null model (t-test,  $df = 998$ ,  $t = -18.4661$ ,  $p \approx 0$ ). It is unclear why the shape of the age-related change differs from one parcellation to another. We speculate that this difference may arise from the aggregation of voxels with opposite age-related trajectories into the same

parcel/ROI by the Destrieux atlas. Nonetheless, this replication supports the finding that functional modules undergo scale-specific changes.

In the accompanying figure we show that single-layer modularity,  $Q_r$ , follows distinct age-related trajectories at different levels of  $\gamma$  when using the Destrieux atlas to parcel the cortex. All panels in this figure are plotted with  $\omega = 10^{-1.5}$ . (A) When  $\gamma = 10^{-1.73}$  the value of  $Q_r$  increases linearly with age. Trajectories corresponding to individual samples are shown in blue while the mean trajectory is shown in red. (B) The variance accounted for ( $R^2$ ) by a quadratic fit of age and  $Q_r$  was calculated and the distribution of those coefficients (shown here in blue) was compared against a null model (shown in orange). (C) Increasing the resolution parameter to  $\gamma = 10^{-0.67}$  leads to a regime where  $Q_r$  decreases with age. (D) Distribution of correlation coefficients compared to null model. (E) As a function of  $\gamma$  we calculated the number of connections that exceed  $\gamma$  and ranked each layer. When  $\gamma$  is small, older layers contain the greatest number of supra- $\gamma$  connections. Increasing  $\gamma$  reverses this relationship.

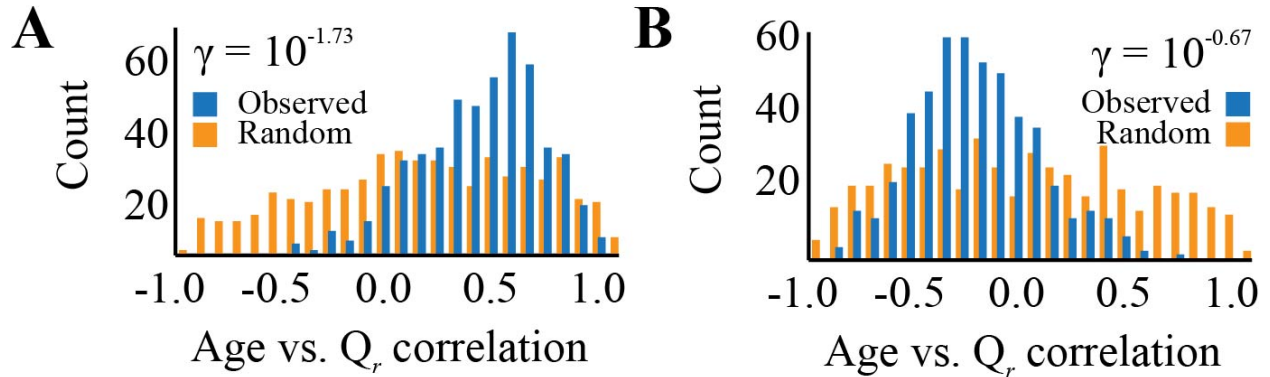


Figure 3.11. It is widely appreciated that head motion can introduce artifactual patterns of functional connectivity in fMRI studies (Power et al 2012). To reduce such biases, we employed a state-of-the-art processing pipeline that included a cluster of measures derived from the QCP module for correcting head motion at both individual and group levels measures (see description of data acquisition in earlier section) (Xu et al 2015). One of the main findings reported here is that functional brain networks become more or less modular with age depending upon how one defines modules. In the main text, this result was presented as distributions of correlation coefficients (see Figures 3.6B and 3.6D). An alternative interpretation is that the modularity of functional networks is correlated with head motion and that apparent age-related changes in modularity, in reality, reflect changes in head motion with age. Indeed, across the NKI cohort head motion (maximum frame-wise displacement) and age are modestly correlated ( $\hat{r} = 0.13$ ,  $p = 0.015$ ). To alleviate this concern, we generated motion estimates,  $d_r$  for each layer in our multi-layer network representation. The value of  $d_r$  was calculated as the mean of the maximum frame-wise displace over all participants used to construct the connectivity matrix for that layer. We then used linear regression to orthogonalize the single-layer modularity scores,  $Q_r$ , with respect to motion,  $d_r$ . The residual scores from this regression were then correlated with age and used to generate figures analogous to 3.6B and 3.6D (panels (A) and (B) of the accompanying figure). As a result of this motion-correction step the size of the effect is attenuated, though we

still find that  $Q_r$  increases when  $\gamma$  is small (median correlation of  $\hat{r} = 0.41$ , interquartile range of  $[+0.18, +0.57]$ ) and the opposite when  $\gamma$  is large (median correlation of  $\hat{r} = -0.31$ , interquartile range of  $[-0.47, -0.09]$ ). We also find that the observed distributions of correlation coefficients are still significantly greater and less than those obtained with a null model ( $df = 998$ ,  $t = 10.13$  and  $t = -8.20$ ).

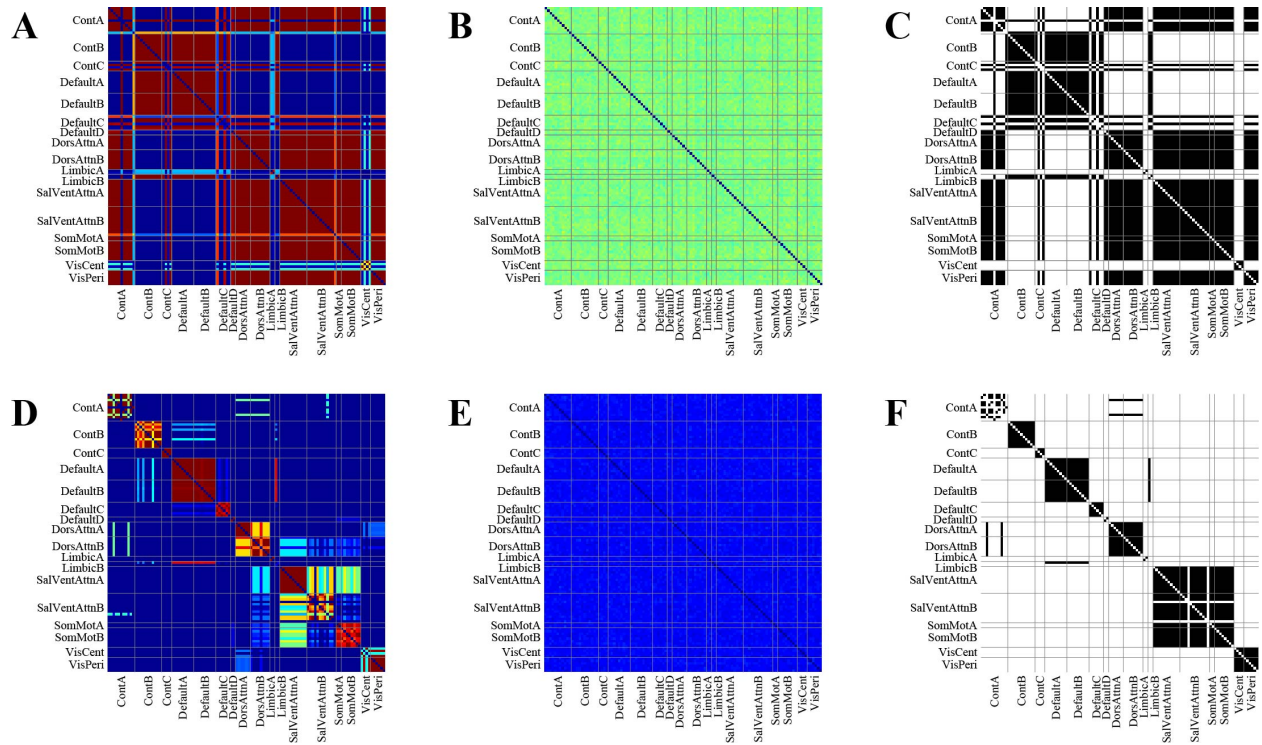


Figure 3.12. Modularity-maximization may produce many near-optimal partitions (Good et al 2010). In this report, we focused on the statistical properties of an ensemble of near-optimal partitions rather than treat a single partition as representative. However, at times it was advantageous to generate such a partition that is, in some way, representative of the ensemble. This process is known as consensus clustering (Strehl & Ghosh 2003) and when applied to partitions of a network, involves iteratively clustering an association matrix (Lancichinetti & Fortunato 2012). For the partition ensemble we generate the association matrix,  $T$ . (Figure 3.12A and Figure 3.12D), whose element,  $T_{ij}$ , represents the number of times that nodes  $i$  and  $j$  were assigned to the same community across the partition ensemble. To obtain consensus clusters from this partition, we re-cluster  $T$  by finding the partition that maximizes the modularity  $Q^{cons} = \sum_{ij}[T_{ij} - P_{ij}]\delta(g_i, g_j)$ . Here,  $P_{ij}$  is the number of times one would expect to find nodes  $i$  and  $j$  in the same community by chance. To obtain an estimate of  $P_{ij}$ , we randomly permute node assignments for each partition in the partition ensemble while preserving the number and

size of communities in each partition (Figure 3.12B and Figure 3.12E). We maximized  $Q^{cons}$  500 times resulting in 500 estimates of consensus communities. Typically, the 500 consensus community estimates are nearly identical, in which case the clustering algorithm stops, having reached consensus. Otherwise, a new association matrix is generated from the consensus community estimates and the algorithm repeats until convergence. Figures 3.12C and 3.12F show consensus communities for  $\gamma = 10^{-1.73}$  and  $\gamma = 10^{-0.67}$ .



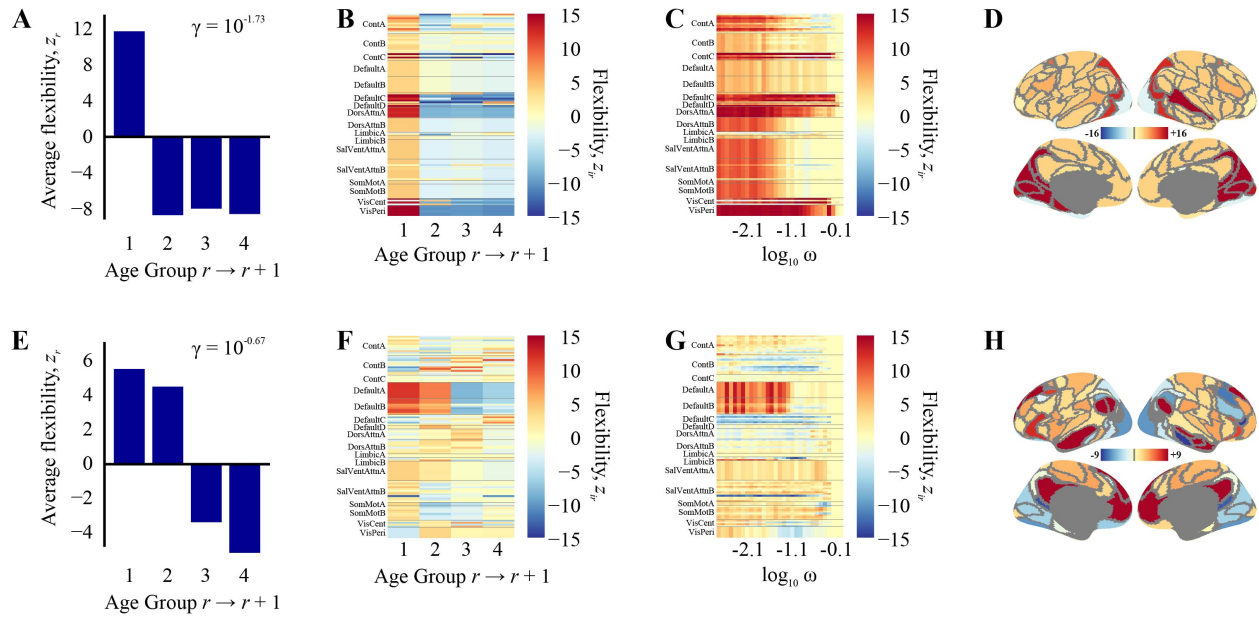


Figure 3.13. Flexibility showing age-related change in community composition. (A) When  $\gamma = 10^{-1.73}$  a greater than expected number of brain regions switch communities between the first two layers. Subsequent layers show community assignments that are more stable than expected. (B) A depiction of node-wise flexibility scores across layers. (C) A depiction of the flexibility between layers 1 and 2 across the full range of  $\omega$ , illustrating that control regions, default mode, dorsal attention, and visual networks change their community assignments most consistently. (D) Topographic representation of flexibility scores between layers 1 and 2. In panels (E-H) we reproduce the same figures as (A-D) but with  $\gamma = 10^{-0.67}$ . Plots (A-B) and (E-F) are shown with  $\omega = 10^{-1.5}$ .

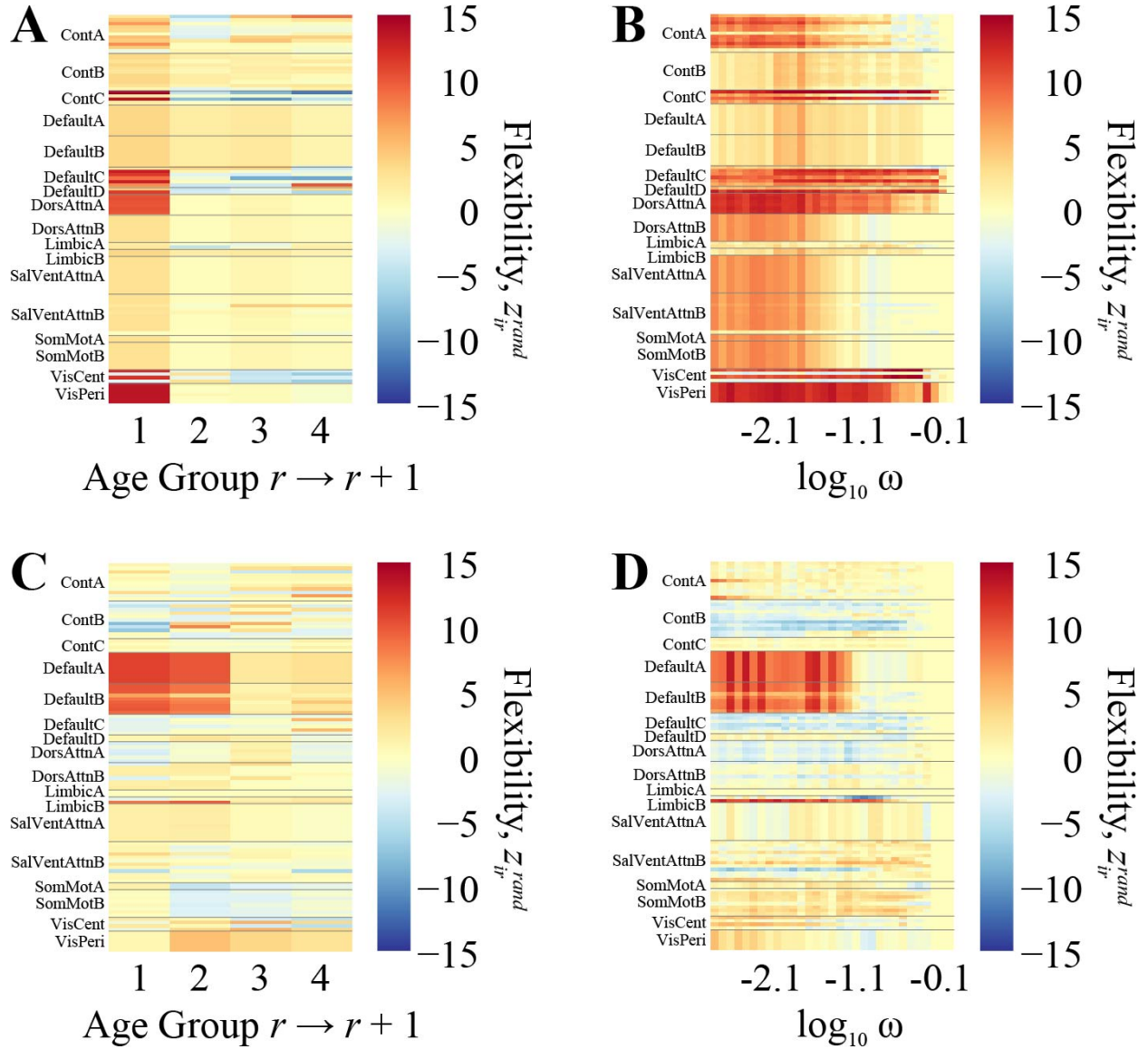


Figure 3.14. In the main text we presented node-level and average flexibility scores, which were compared to the expected flexibility under a null model in which the community assignments of single-layer partitions was fixed but where the order of layers was randomized. We also compared the raw flexibility scores to additional null model whose construction is described earlier in this supplement. The *network null model* yielded null flexibility scores for each region  $i$  between layers  $r$  and  $r + 1$ . We denote these scores as  $f_{ir}^{rad}$ . Because the network null model produced a single estimate of flexibility scores rather than a distribution of null scores, we

decided to treat each node-level flexibility score as a Bernoulli variable and tested the null hypothesis that  $f_{ir} = f_{ir}^{rand}$ . The test statistic is given as:

$$z_{ir}^{rand} = \frac{f_{ir} - f_{ir}^{rand}}{\sqrt{p(1-p)(2/N_{reps})}}$$

where  $p = \frac{(f_{ir} + f_{ir}^{rand})}{2}$  and  $N_{reps} = 500$  was the number of partitions in the partition ensemble.

In general, we found that these results were similar to those obtained using the permutation null *model*. In particular, the randomized null model highlights control, default mode, dorsal attention, and visual systems as being particularly flexible at coarse scales (Figure 3.14A) and default mode components as being flexible at fine scales (Figure 3.14B).

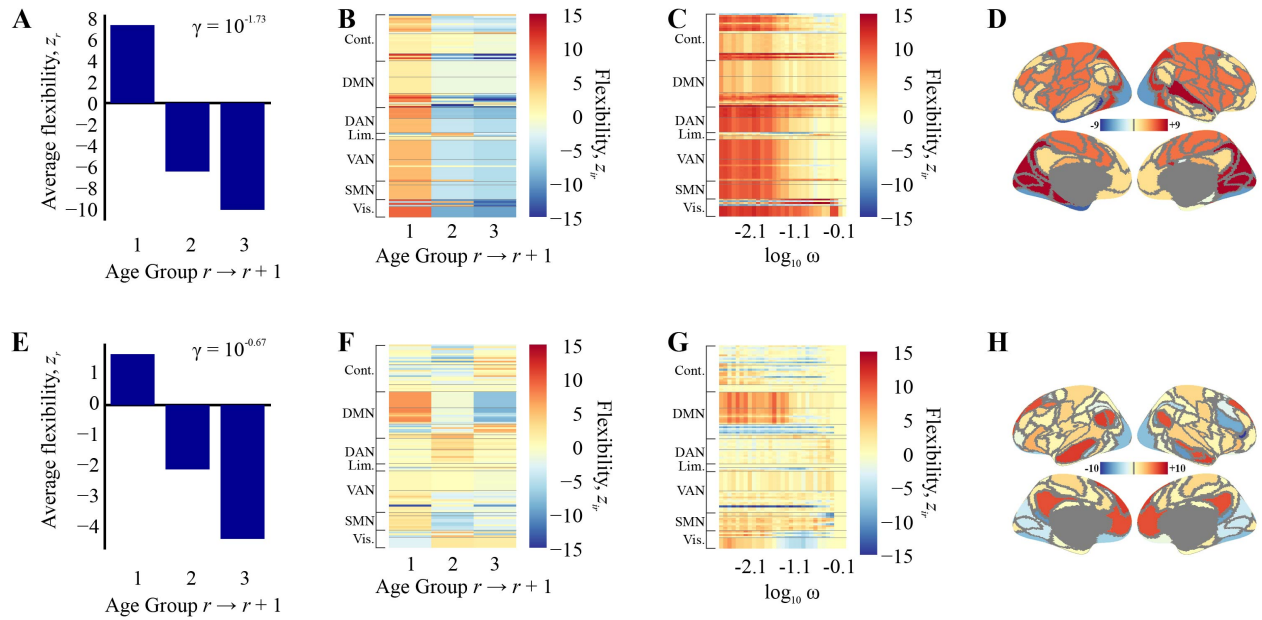


Figure 3.15. We reproduce Figure 3.13 from the main text for  $K = 4$ . Flexibility showing age-related change in community composition. (A) When  $\gamma = 10^{-1.73}$  a greater than expected number of brain regions switch communities between the first two layers. Subsequent layers show community assignments that are more stable than expected. (B) A depiction of node-wise flexibility scores across layers. (C) A depiction of the flexibility between layers 1 and 2 across the full range of  $\omega$ , illustrating that control regions, default mode, dorsal attention, and visual networks change their community assignments most consistently. (D) Topographic representation of flexibility scores between layers 1 and 2. In panels (E-H) we reproduce the same figures as (A-D) but with  $\gamma = 10^{-0.67}$ . Plots (A-B) and (E-F) are shown with  $\omega = 10^{-1.5}$ .

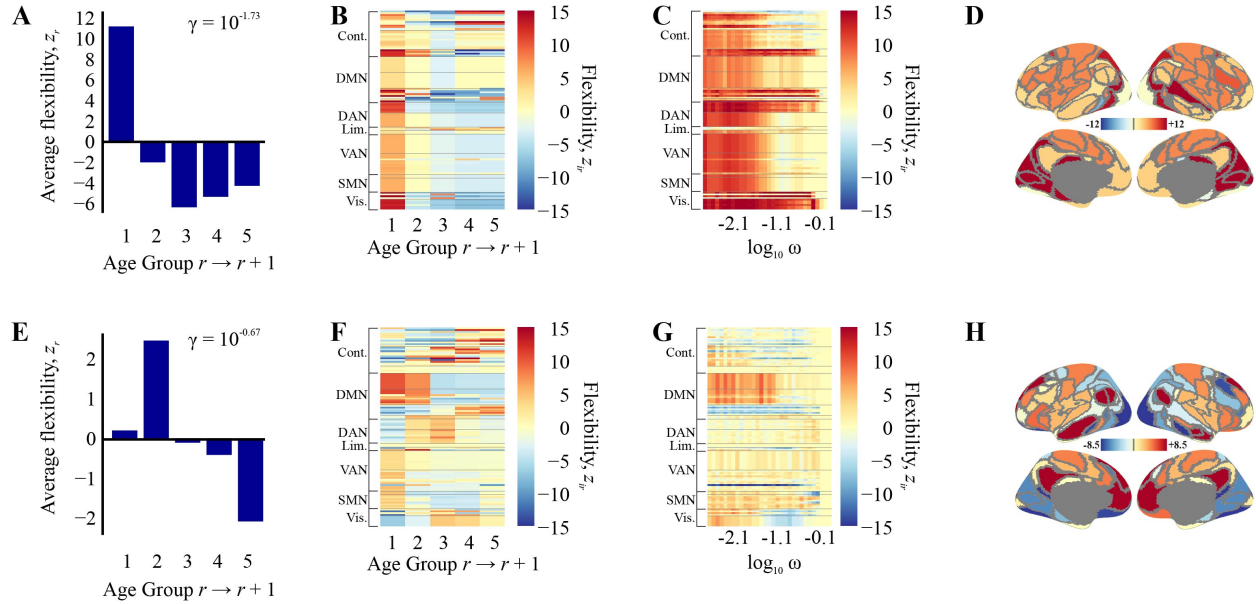


Figure 3.16. We reproduce Figure 3.13 from the main text for  $K = 6$ . Flexibility showing age-related change in community composition. (A) When  $\gamma = 10^{-1.73}$  a greater than expected number of brain regions switch communities between the first two layers. Subsequent layers show community assignments that are more stable than expected. (B) A depiction of node-wise flexibility scores across layers. (C) A depiction of the flexibility between layers 1 and 2 across the full range of  $\omega$ , illustrating that control regions, default mode, dorsal attention, and visual networks change their community assignments most consistently. (D) Topographic representation of flexibility scores between layers 1 and 2. In panels (E-H) we reproduce the same figures as (A-D) but with  $\gamma = 10^{-0.67}$ . Plots (A-B) and (E-F) are shown with  $\omega = 10^{-1.5}$ .

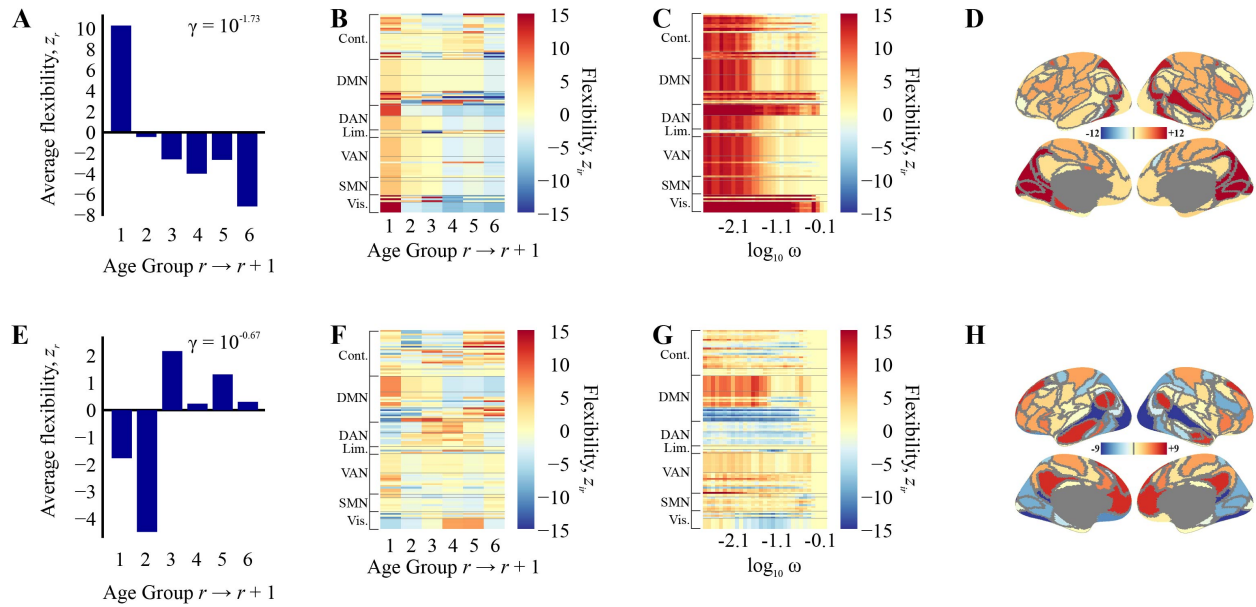


Figure 3.17. We reproduce Figure 6 from the main text for  $K = 7$ . Flexibility showing age-related change in community composition. (A) When  $\gamma = 10^{-1.73}$  a greater than expected number of brain regions switch communities between the first two layers. Subsequent layers show community assignments that are more stable than expected. (B) A depiction of node-wise flexibility scores across layers. (C) A depiction of the flexibility between layers 1 and 2 across the full range of  $\omega$ , illustrating that control regions, default mode, dorsal attention, and visual networks change their community assignments most consistently. (D) Topographic representation of flexibility scores between layers 1 and 2. In panels (E-H) we reproduce the same figures as (A-D) but with  $\gamma = 10^{-0.67}$ . Plots (A-B) and (E-F) are shown with  $\omega = 10^{-1.5}$ .

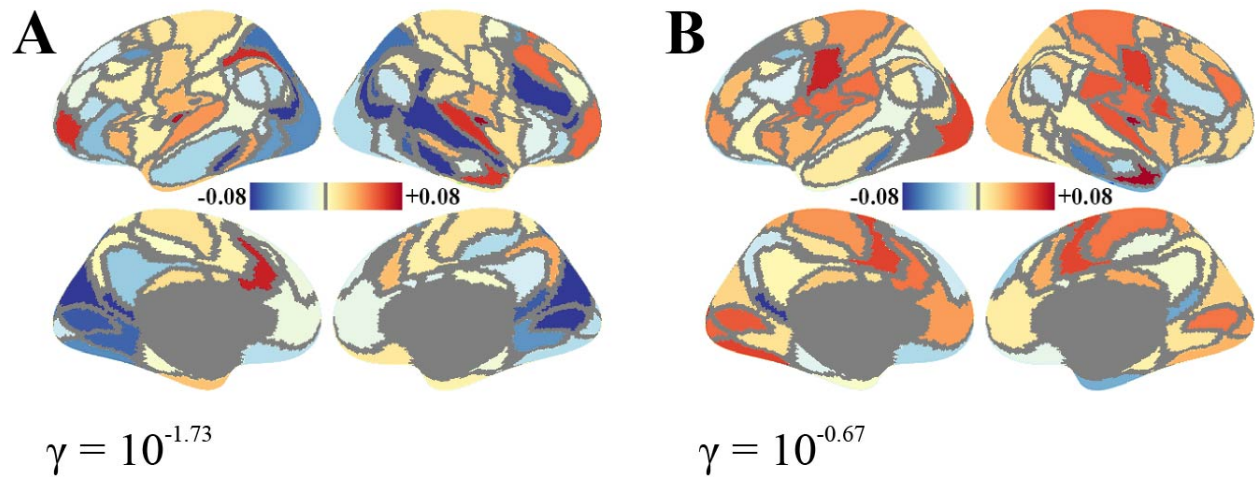


Figure 3.18. Participation coefficient scores. (A) Regions that consistently show increased (red) or decreased (blue) participation coefficient between the first and last layers when  $\gamma = 10^{-1.73}$  and the magnitude of that change. (B) Same plot as in panel (A) but shown for  $\gamma = 10^{-0.67}$ . Both plots shown with  $\omega = 10^{-1.5}$ .



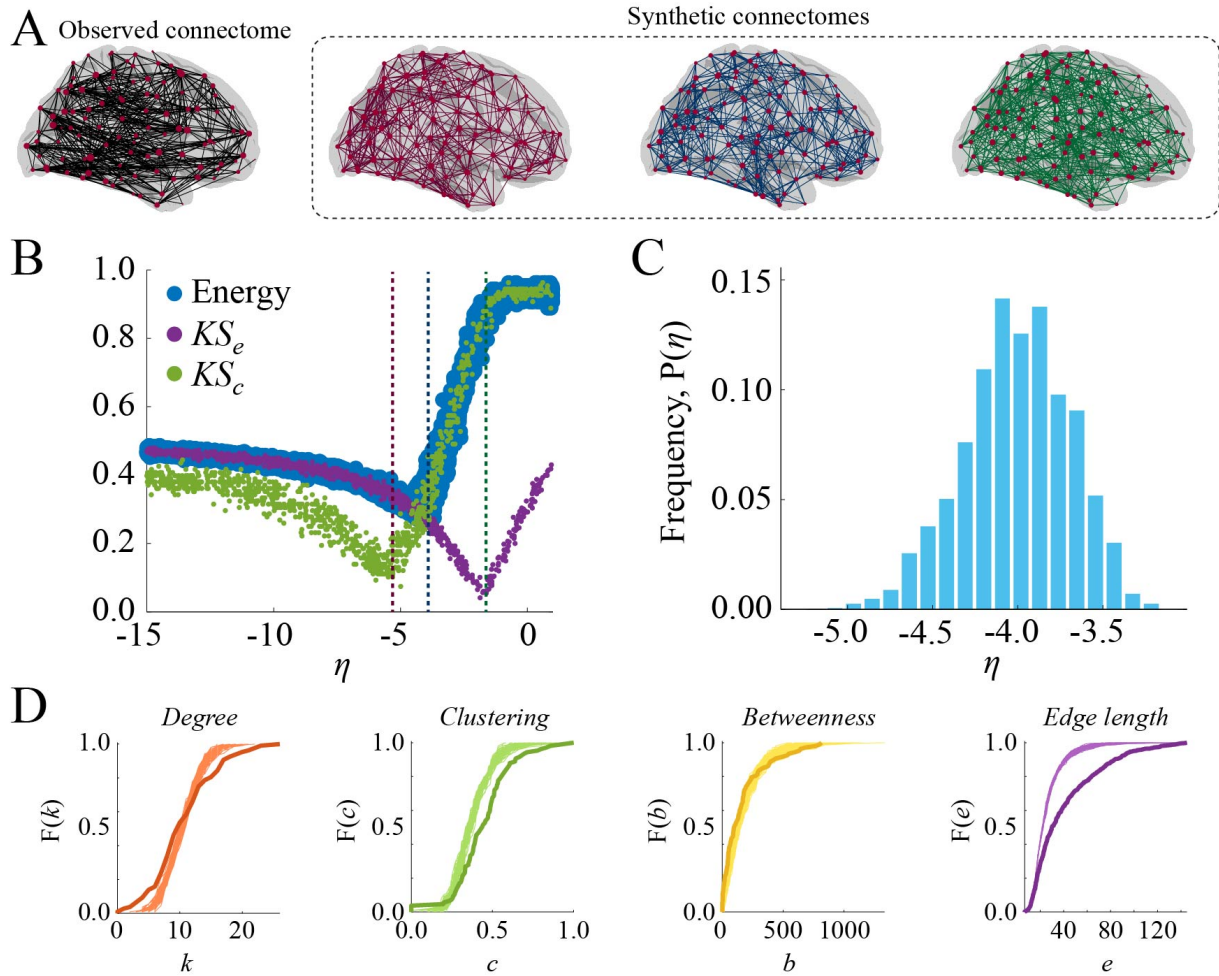


Figure 4.1 Summary of the geometric model: (A) observed (black) and synthetic networks generated at different points in parameter space. (B) Energy landscape showing the behavior of  $KS_e$ ,  $KS_c$ , and energy as a function of  $\eta$ . The dashed vertical lines indicate the parameter values at which the example synthetic networks were generated. (C) Distribution of  $\eta$  parameter of top 1% lowest-energy synthetic networks aggregated across all participants. (D) Cumulative distributions of degree (orange), clustering coefficient (green), betweenness centrality (yellow), and edge length (purple) for observed connectome (darker line) and best-fitting synthetic networks (lighter lines) for a representative participant.



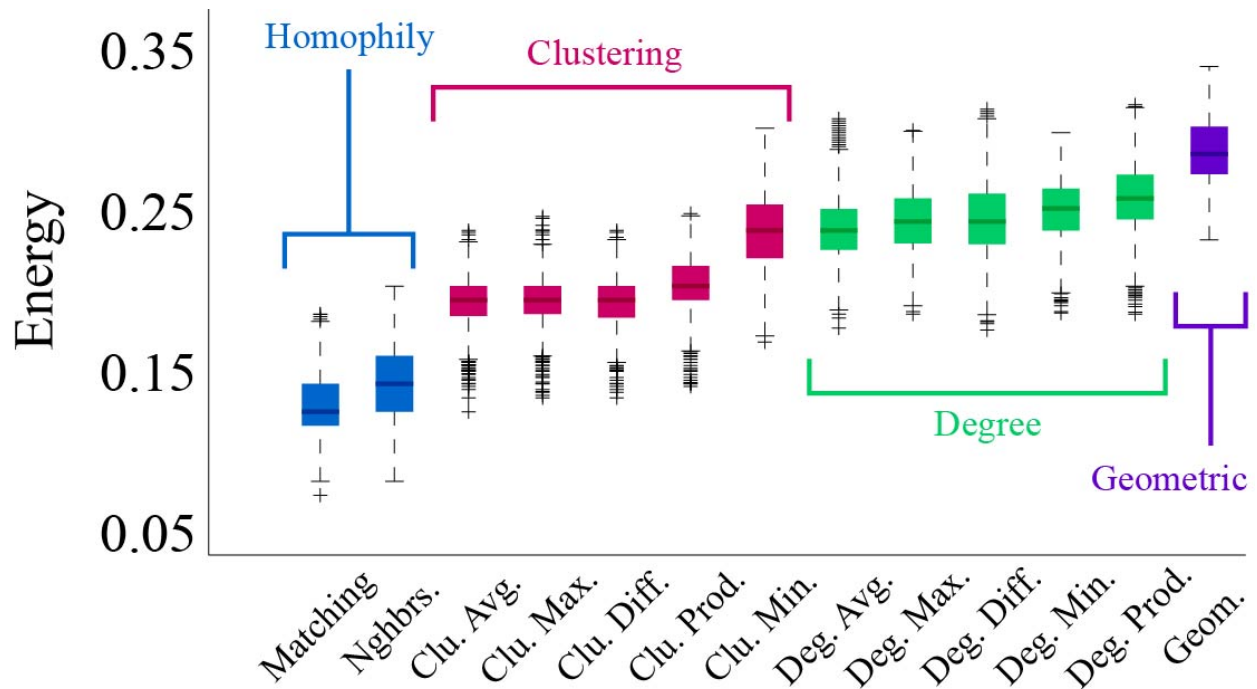


Figure 4.2 Energy distributions across all models. Each box plot represents the top 1% lowest energy synthetic networks generated by each model and aggregated across all participants. The color of each plot indicates the general class of the model: Homophily is shown in blue, clustering in pink, degree in green, and geometric in purple. The specific wiring rule names are shown along the x-axis.

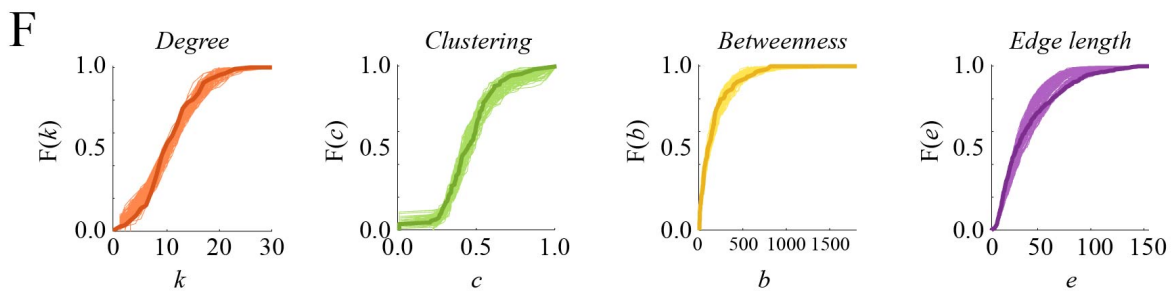
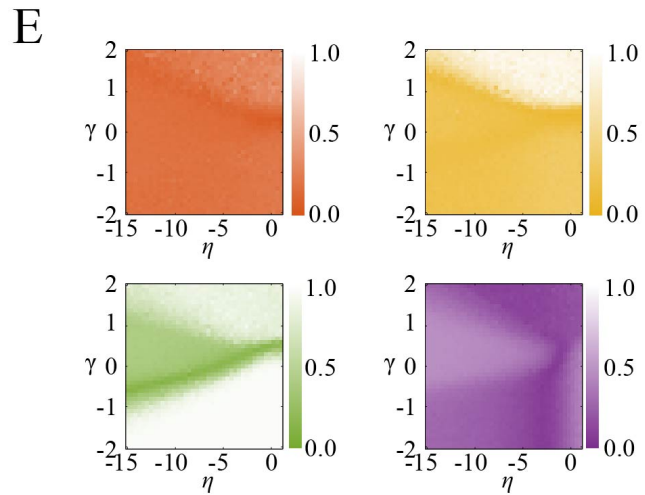
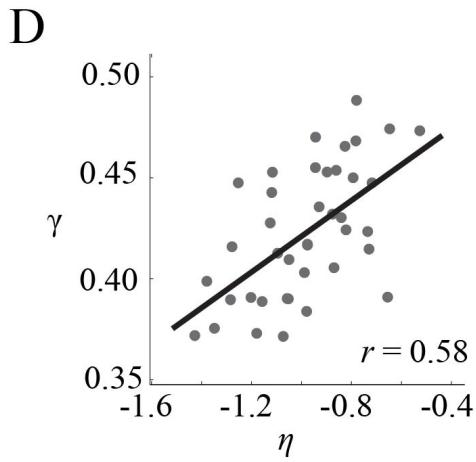
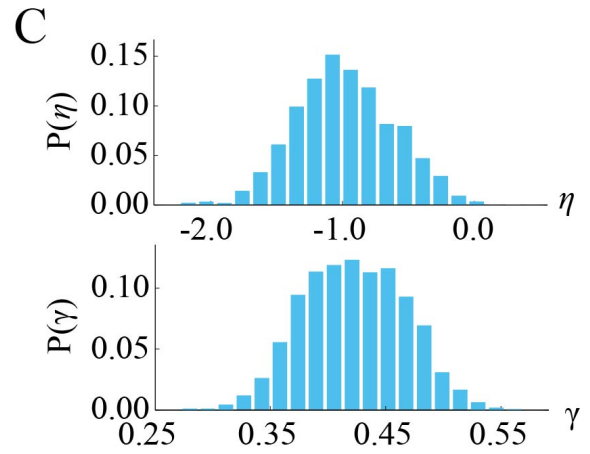
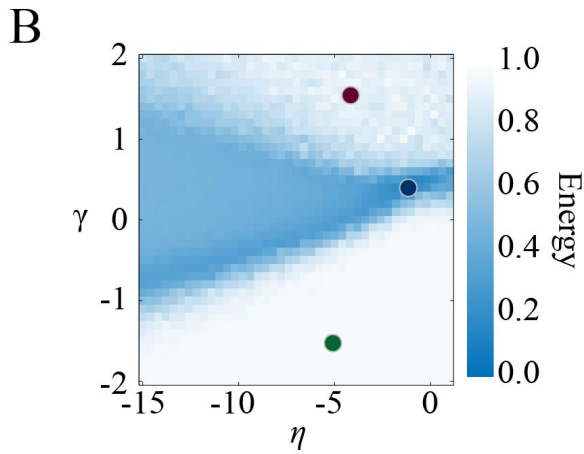
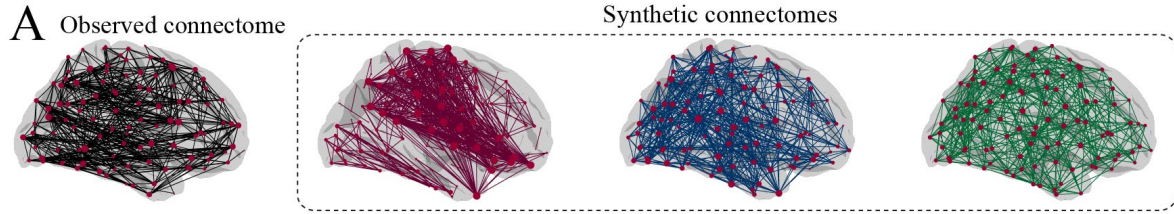


Figure 4.3 Matching Index Model: (A) observed (black) and synthetic networks generated at different points in parameter space. (B) Energy landscape showing the points at which the example synthetic networks were generated. (C) Distribution of  $\eta$  and  $\gamma$  parameters of best-fitting synthetic networks aggregated across all participants. (D) Tradeoff between  $\eta$  and  $\gamma$ . Each point represents the mean parameter values for an individual participant. Participants with larger values of  $\eta$  tend to have the smallest magnitude  $\gamma$  and vice versa. (E) KS statistic landscapes for degree (orange), clustering (green), betweenness (yellow), and edge length (purple) for observed connectome and best-fitting synthetic networks for a single participant. (F) Cumulative distributions of degree (orange), clustering (green), betweenness (yellow), and edge length (purple) for observed connectome (darker line) and best-fitting synthetic networks (lighter lines) for a representative participant.

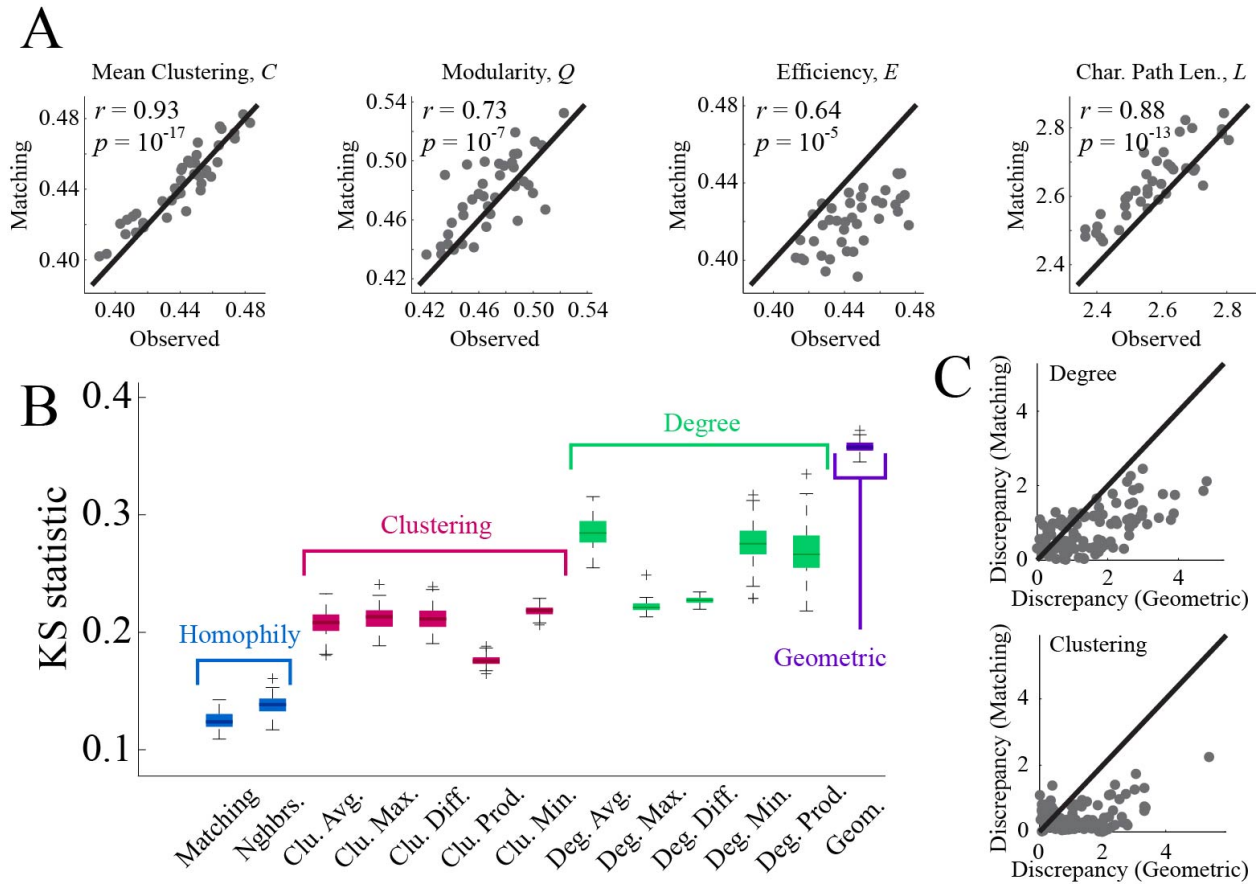


Figure 4.4 Cross validation of the matching index model: (A) Comparison of matching index model and observed connectomes in terms of the graph-theoretic measures mean clustering, modularity, global efficiency, and characteristic path length. (B) Comparison of all models in terms of reproducing the distance-dependent degree assortativity (i.e. the propensity for high degree nodes to be linked by long-distance connections). (C) Discrepancies in degree and clustering coefficient sequences of synthetic networks generated by the matching index model and pure geometric model.

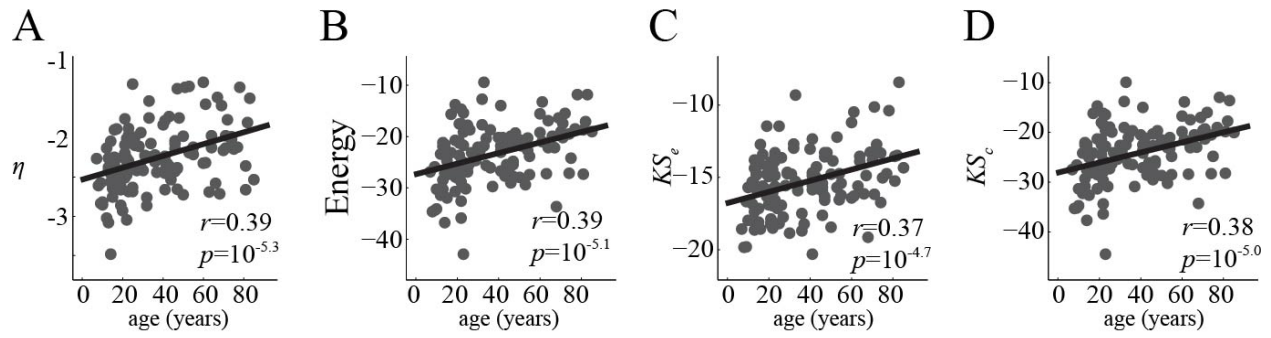


Figure 4.5 Changes in model parameters and energy components across the lifespan: (A) The geometric parameter,  $\eta$  weakens with age. (B) The average energy of each participant's best-fitting synthetic networks (z-scored against an ensemble of synthetic networks generated using a uniform wiring rule) also increases with age. (C, D)  $KS_e$  and  $KS_c$  increase with age, and these increases collectively drive the increase in energy.

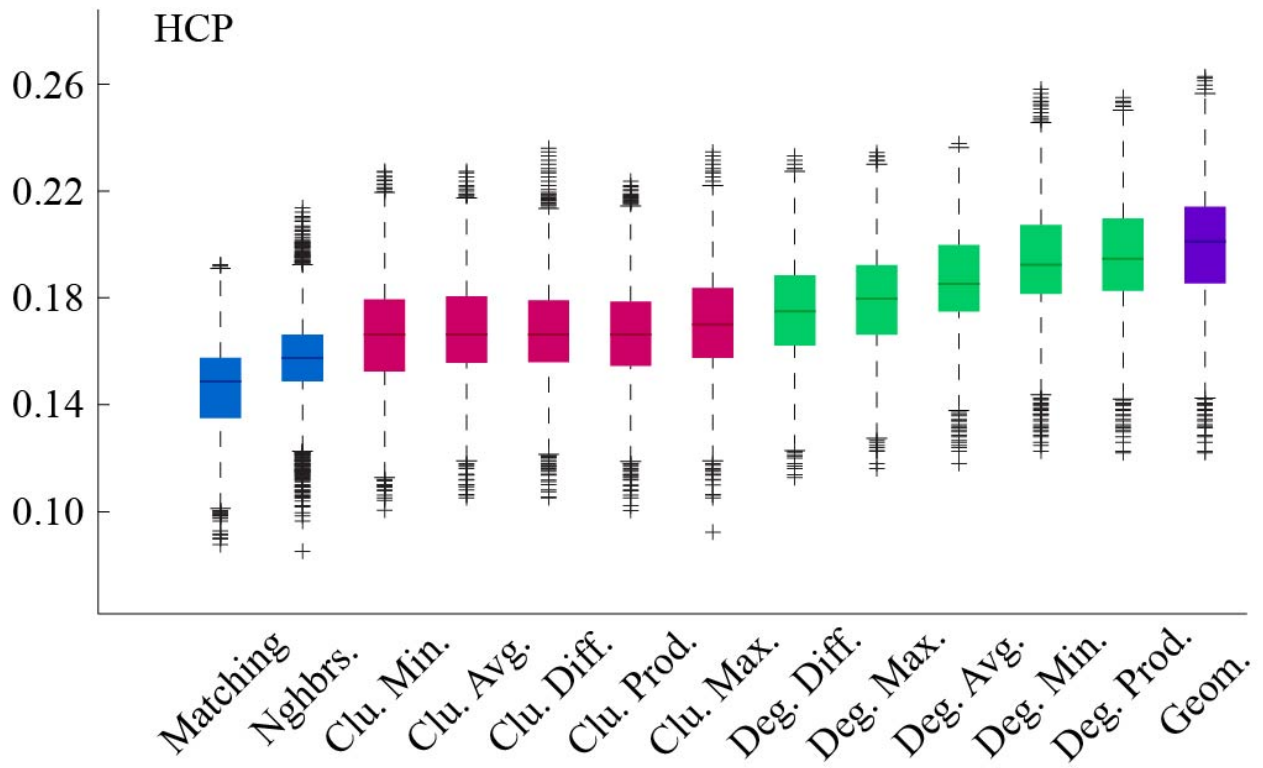


Figure 4.6 Model energies for HCP dataset.

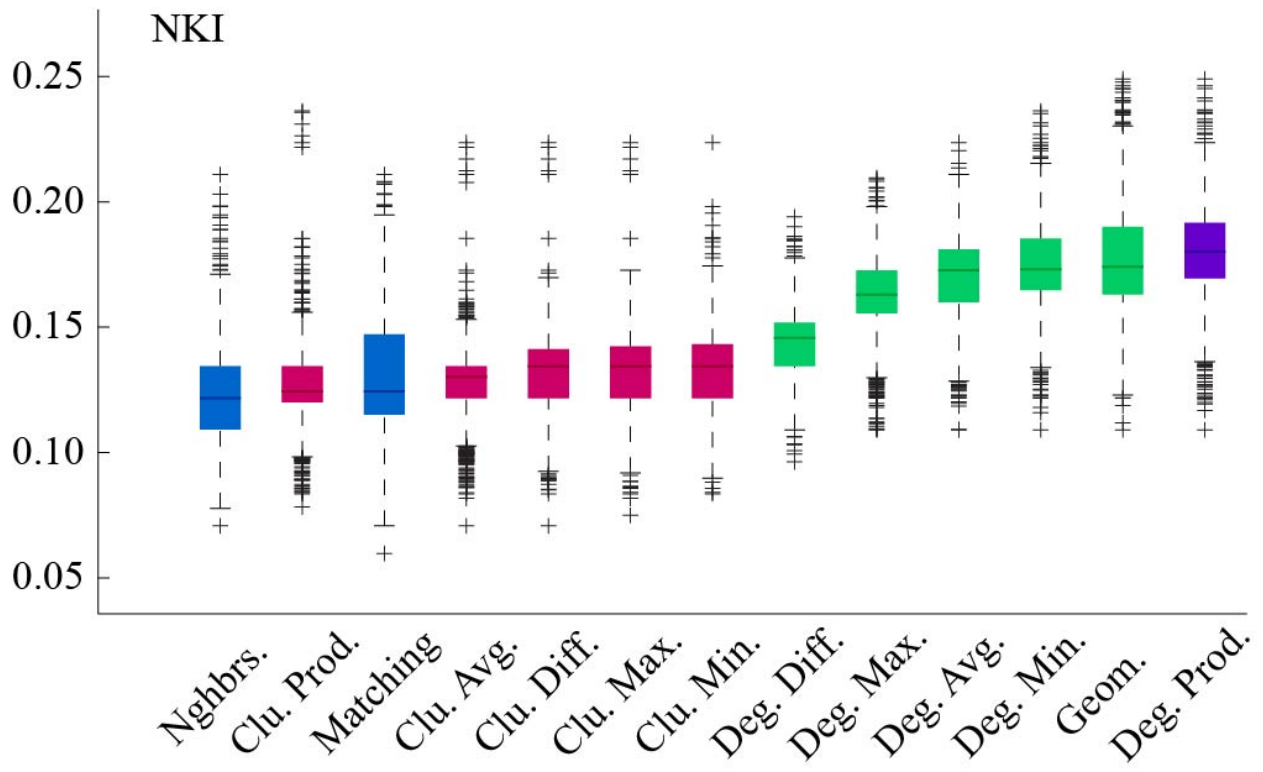


Figure 4.7 Model energies for NKI dataset.

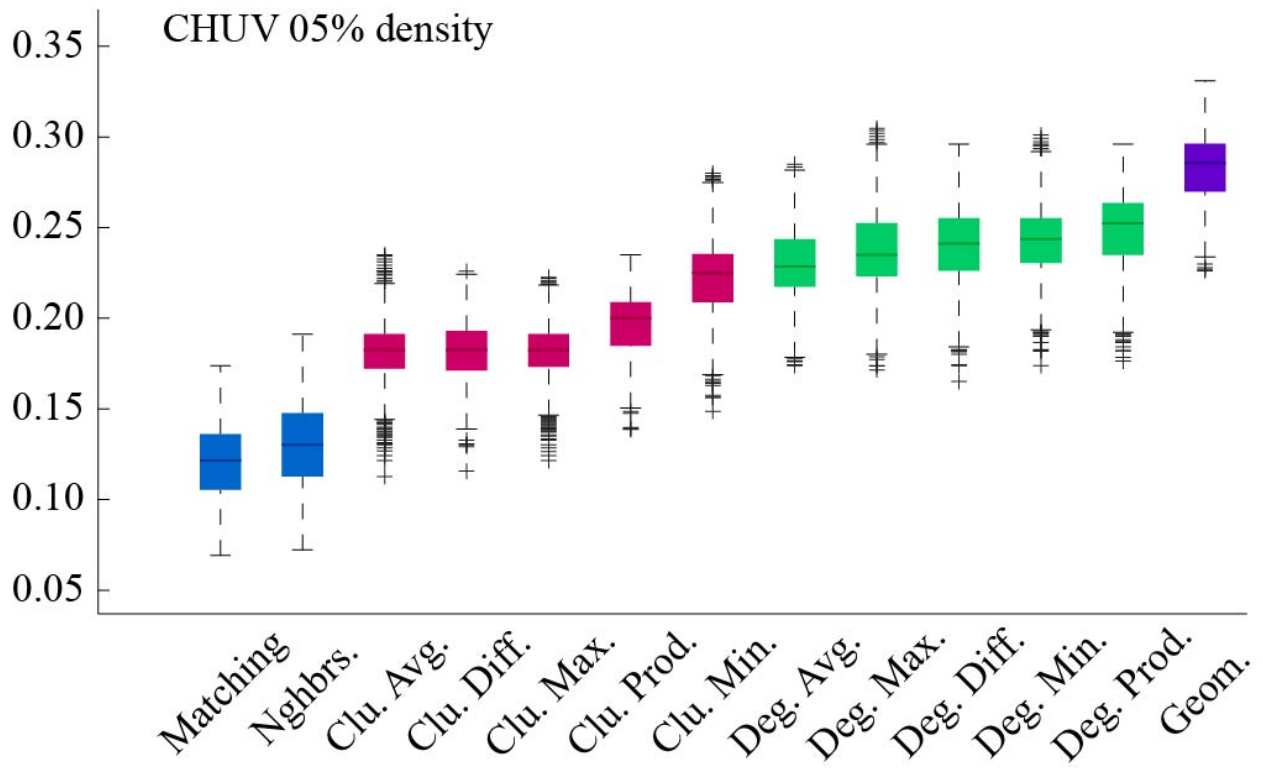


Figure 4.8 Model energies for CHUV dataset with  $\rho \approx 5\%$ .



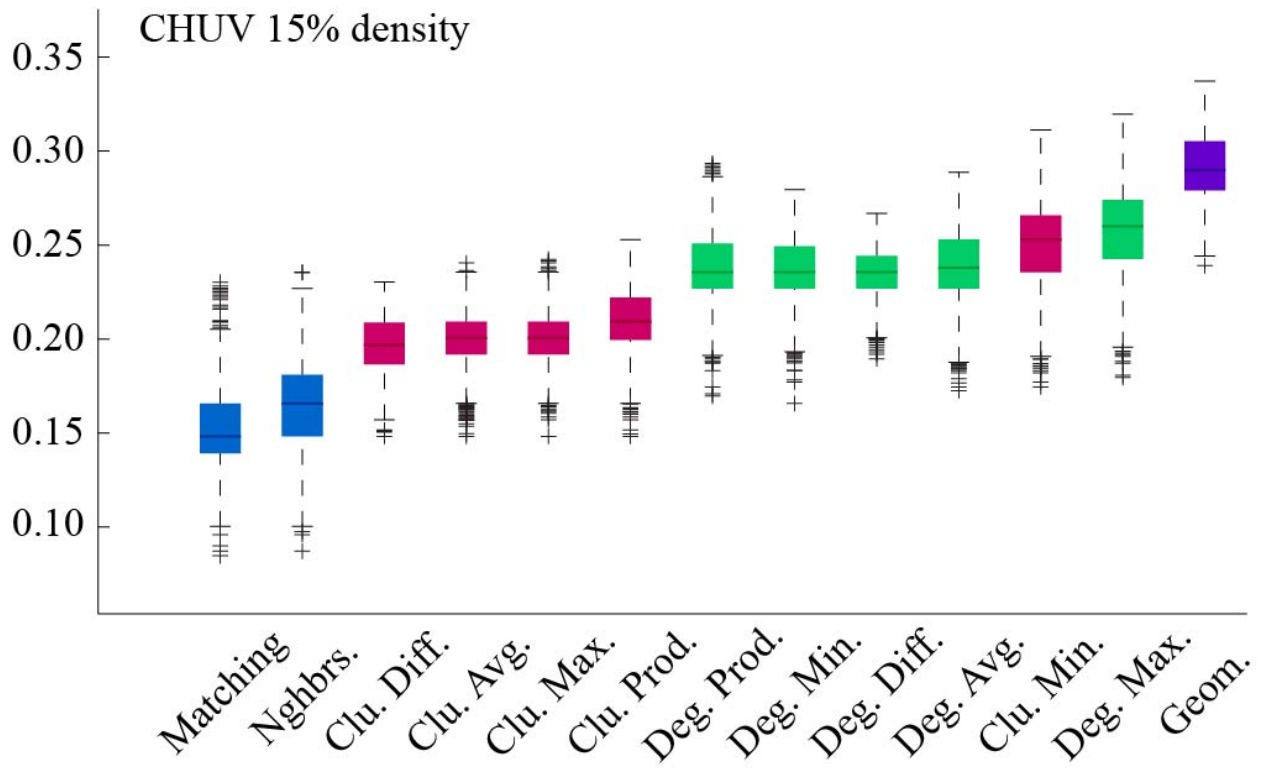


Figure 4.9 Model energies for CHUV dataset with  $\rho \approx 15\%$ .

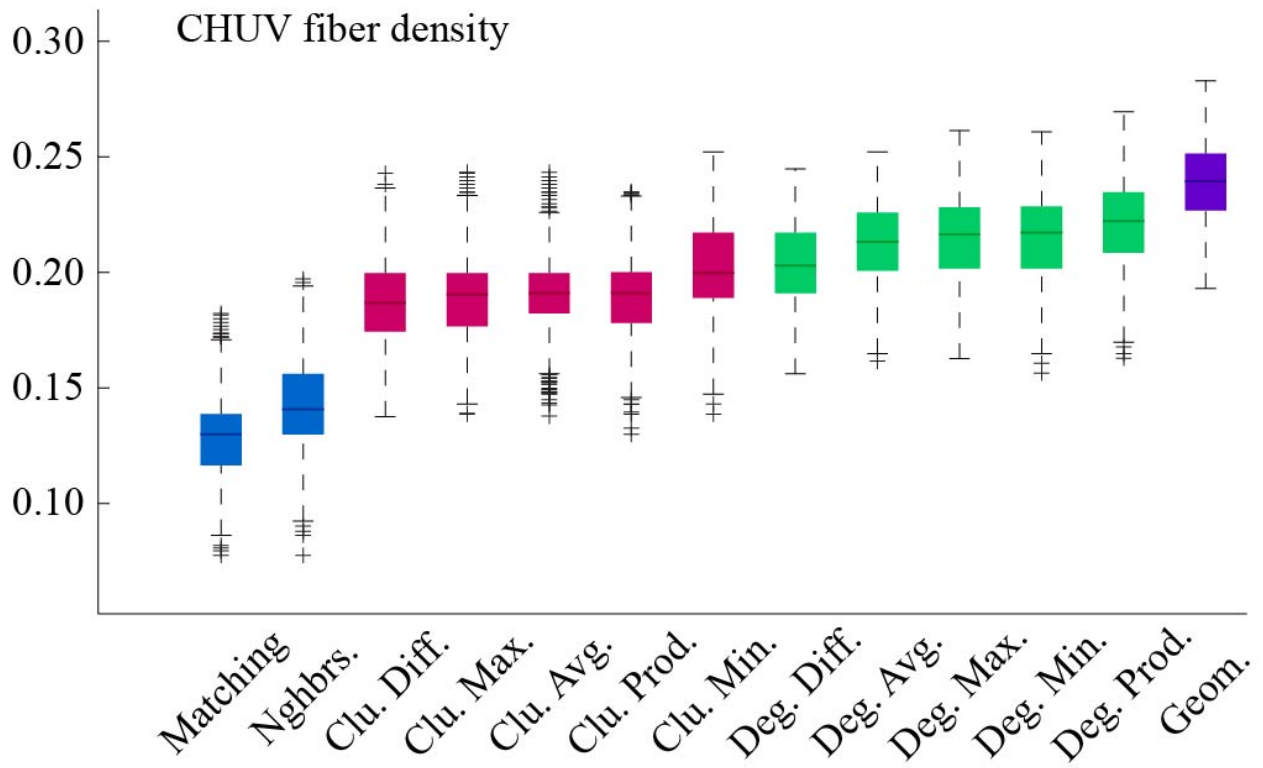


Figure 4.10 Model energies for CHUV dataset with  $\rho \approx 10\%$  and edge presence/absence determined by fiber density weights rather than streamline/fiber tract counts.

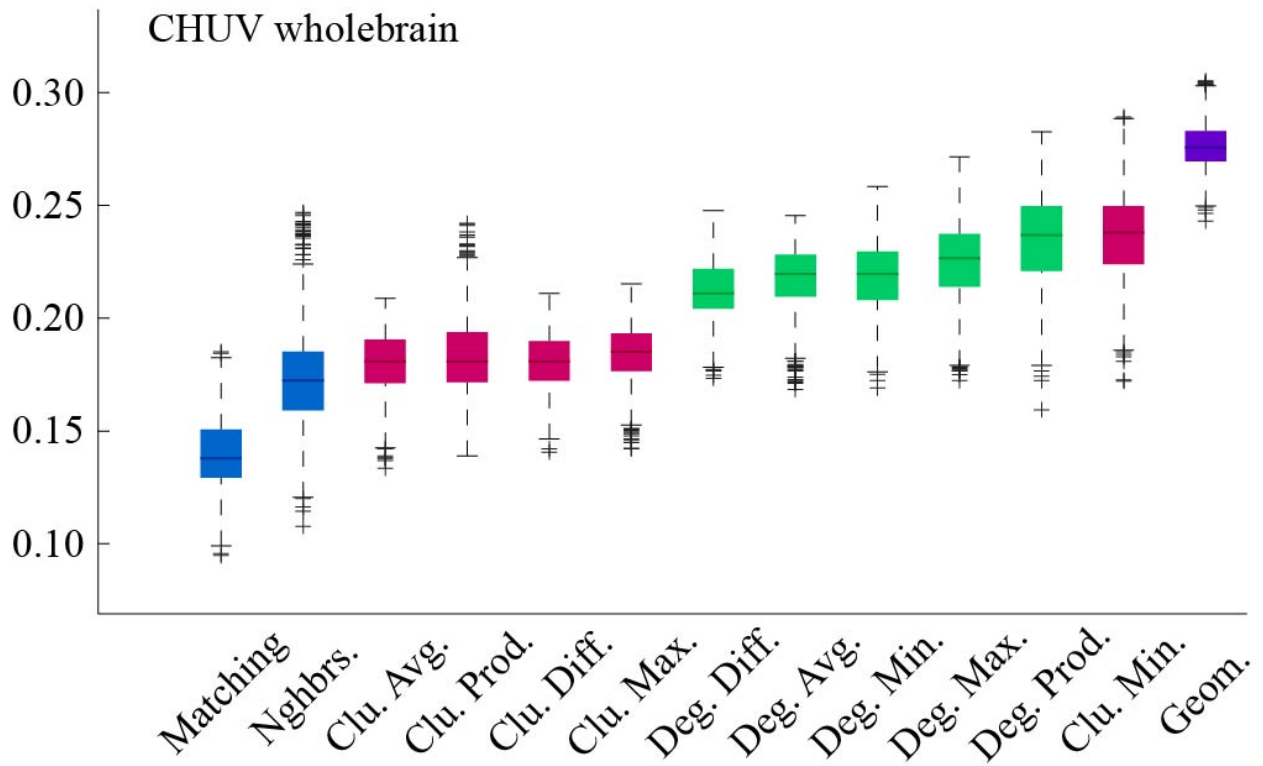


Figure 4.11 Model energies for CHUV dataset with  $\rho \approx 10\%$  but for entire cerebral cortex.

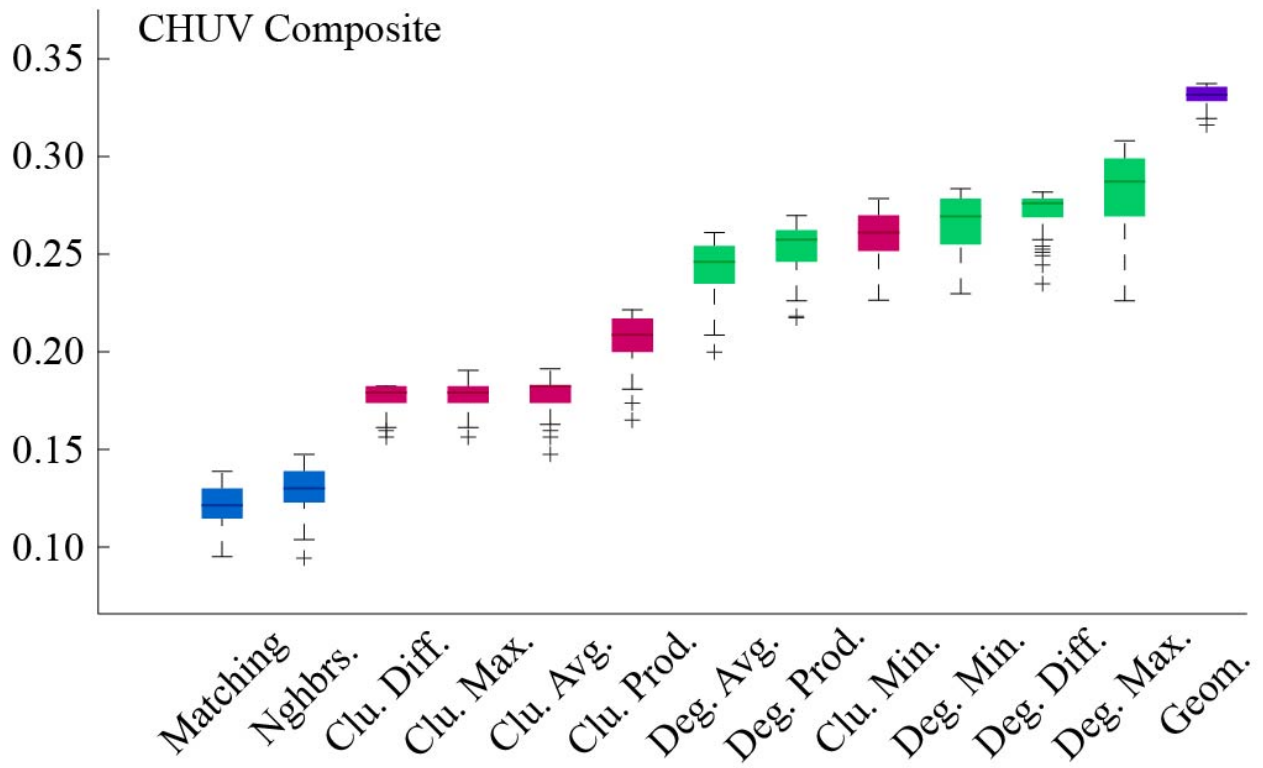


Figure 4.12 Model energies for CHUV composite connectivity matrix.

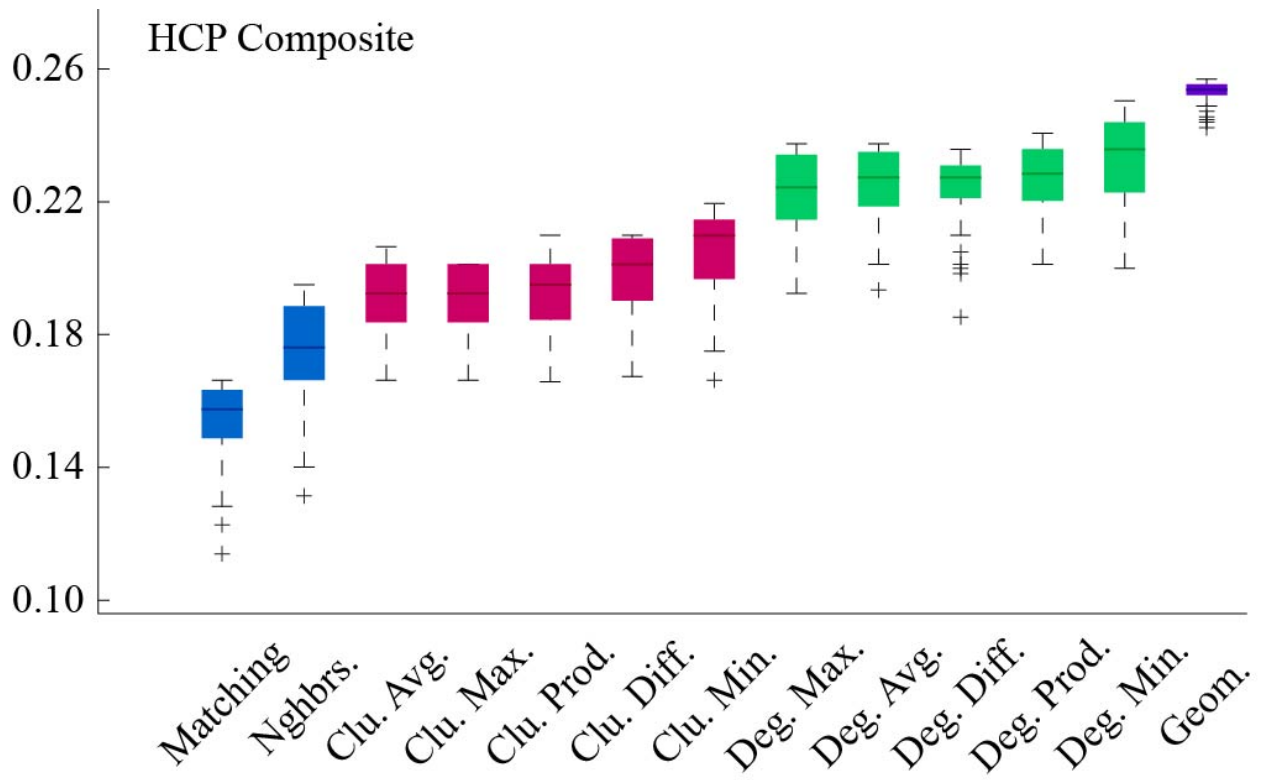


Figure 4.13 Model energies for HCP composite connectivity matrix.

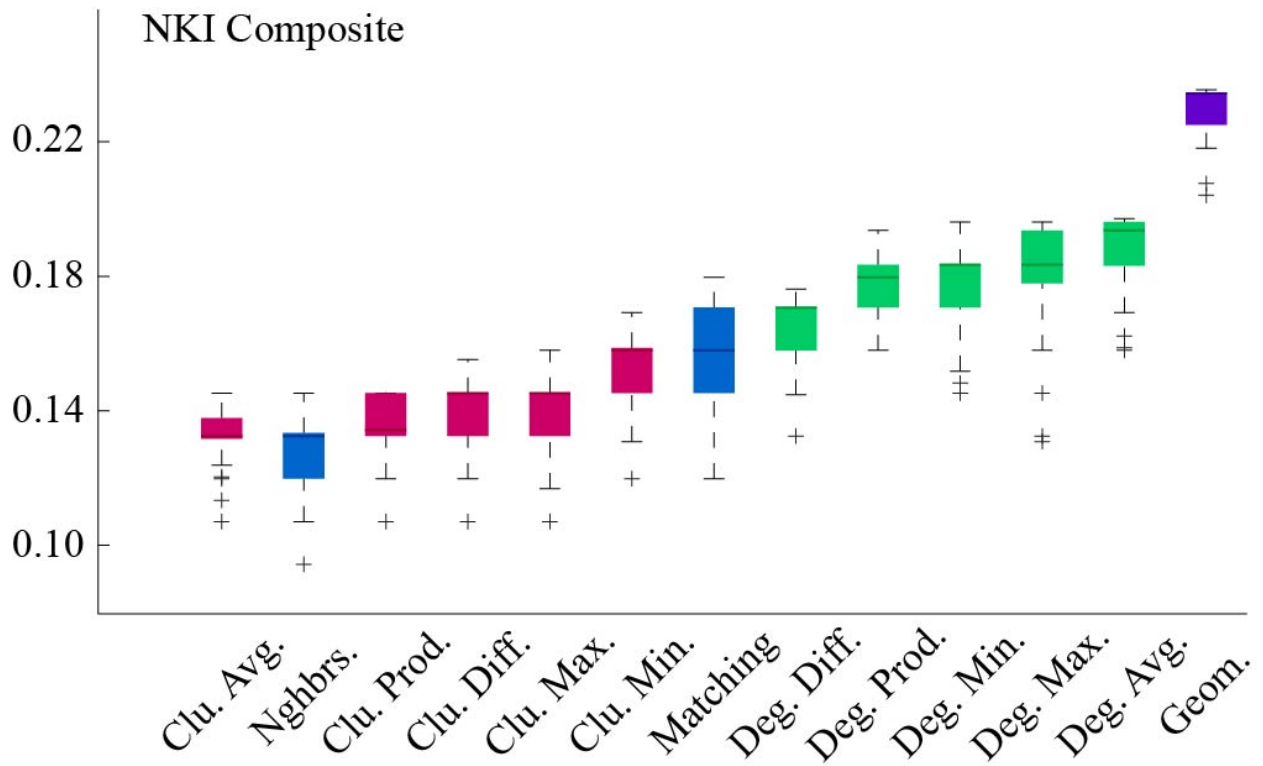


Figure 4.14 Model energies for NKI composite connectivity matrix.

Name	$K(u, v)$	$E$	$\eta$	$\gamma$	$KS_k$	$KS_b$	$KS_e$	$KS_c$
Clu. Avg.	$(\frac{c_u}{\gamma} + \frac{c_v}{\gamma})$	$0.19 \pm 0.02$	$-3.06 \pm 0.48$	$-5.75 \pm 1.62$	$0.14 \pm 0.03$	$0.18 \pm 0.03$	$0.17 \pm 0.03$	$0.15 \pm 0.03$
Clu. Diff.	$ c_u - c_v $	$0.19 \pm 0.02$	$-3.13 \pm 0.49$	$-5.85 \pm 2.07$	$0.15 \pm 0.03$	$0.18 \pm 0.03$	$0.17 \pm 0.03$	$0.16 \pm 0.03$
Clu. Max.	$\max[c_u, c_v]$	$0.19 \pm 0.02$	$-3.14 \pm 0.49$	$-5.75 \pm 1.97$	$0.15 \pm 0.03$	$0.18 \pm 0.03$	$0.17 \pm 0.03$	$0.15 \pm 0.03$
Clu. Min	$\min[c_u, c_v]$	$0.24 \pm 0.03$	$-3.60 \pm 0.41$	$-4.04 \pm 1.09$	$0.12 \pm 0.03$	$0.19 \pm 0.05$	$0.23 \pm 0.03$	$0.17 \pm 0.05$
Clu. Prod.	$c_u c_v$	$0.20 \pm 0.02$	$-3.14 \pm 0.39$	$-3.44 \pm 1.00$	$0.11 \pm 0.03$	$0.18 \pm 0.03$	$0.19 \pm 0.03$	$0.15 \pm 0.04$
Deg. Avg.	$(\frac{k_u}{\gamma} + \frac{k_v}{\gamma})$	$0.24 \pm 0.02$	$-3.76 \pm 0.57$	$2.47 \pm 0.38$	$0.18 \pm 0.05$	$0.18 \pm 0.05$	$0.23 \pm 0.03$	$0.19 \pm 0.04$
Deg. Diff.	$ k_u - k_v $	$0.25 \pm 0.02$	$-4.55 \pm 0.76$	$-1.03 \pm 2.61$	$0.13 \pm 0.04$	$0.19 \pm 0.04$	$0.24 \pm 0.03$	$0.21 \pm 0.05$
Deg. Max.	$\max[k_u, k_v]$	$0.25 \pm 0.02$	$-4.02 \pm 0.60$	$2.20 \pm 0.43$	$0.13 \pm 0.04$	$0.18 \pm 0.05$	$0.24 \pm 0.03$	$0.18 \pm 0.05$
Deg. Min.	$\min[k_u, k_v]$	$0.25 \pm 0.02$	$-3.99 \pm 0.64$	$2.03 \pm 0.47$	$0.20 \pm 0.05$	$0.16 \pm 0.04$	$0.24 \pm 0.03$	$0.21 \pm 0.04$
Deg. Prod.	$k_u k_v$	$0.26 \pm 0.02$	$-3.83 \pm 0.70$	$1.14 \pm 0.32$	$0.19 \pm 0.07$	$0.16 \pm 0.06$	$0.24 \pm 0.04$	$0.22 \pm 0.04$
Matching	$\frac{ X_u \cap X_v }{ X_u \cup X_v }$	$0.12 \pm 0.02$	$-0.98 \pm 0.37$	$0.42 \pm 0.04$	$0.10 \pm 0.03$	$0.10 \pm 0.02$	$0.10 \pm 0.03$	$0.11 \pm 0.02$
Nghbrs.	$\sum_w a_{uw} a_{wv}$	$0.14 \pm 0.02$	$-1.18 \pm 0.43$	$0.35 \pm 0.04$	$0.11 \pm 0.03$	$0.11 \pm 0.03$	$0.11 \pm 0.03$	$0.11 \pm 0.03$
Geom.	<b>1</b>	$0.29 \pm 0.02$	$-4.01 \pm 0.31$	<i>N/A</i>	$0.15 \pm 0.03$	$0.18 \pm 0.04$	$0.29 \pm 0.02$	$0.27 \pm 0.03$

Table 4.1. Complete list of generative models. The first two columns show each model's name and the non-geometric wiring rule. The remaining columns indicate sample mean $\pm$ standard error energy (E), and the four KS statistics.

## Appendix: GRAPH THEORETIC TERMINOLOGY

This dissertation makes reference to a number of graph-theoretic terms. In this appendix we provide a detailed account of the definition of those terms.

A network  $\mathcal{G}$  comprised of  $n$  nodes can be described by its adjacency matrix,  $\mathbf{A} = \{A_{ij}\}$ . If a connection exists between nodes  $i$  and  $j$  then the corresponding element,  $A_{ij}$ , will be associated with some real-valued weight; if no connection exists than the weight is assumed to be zero. In general,  $A_{ij} \neq A_{ji}$ , though we will consider the special case of a symmetric matrix where  $A_{ij} = A_{ji}$ .

*Node strength.* For each node we can define its strength as the total weight of all its connections:

$$s_i = \sum_{j=1}^n A_{ij}$$

In a binary network where connection weights are all equal to 1, node strength is equivalent to degree,  $k_i$ , which counts the total number of connections made by node  $i$ .

*Clustering coefficient.* In a network where all edge weights are equal to zero, node  $i$ 's clustering coefficient,  $c_i$ , counts the fraction of its neighbors that are also neighbors. This can be expressed as:

$$c_i = \frac{2t_i}{k_i(k_i - 1)}$$



Where  $t_i = \sum_{ih} A_{ij}A_{ih}A_{jh}$  counts the number of triangles surrounding node  $i$  in a binary network. In a weighted network,  $t_i = \sum_{jk} \tilde{A}_{ij}\tilde{A}_{ih}\tilde{A}_{jh}$ , where  $\tilde{A}_{ij} = A_{ij}/\max(A_{ij})$ .

*Shortest path matrix.* Given  $\mathbf{A}$  one can calculate the shortest path matrix  $\mathbf{D} = \{D_{ij}\}$  whose elements denote either the minimum number of discrete steps necessary to go from node  $i$  to  $j$  (for binary networks) or the total weight of the shortest path (for weighted networks). The matrix  $\mathbf{D}$  can be acquired straightforward using Dijkstra's algorithm (Dijkstra 1959). It is worth noting, however, that this algorithm seeks the shortest path, which, in a weighted network, is equivalent to the path with the least total weight. However, we usually think of connection weights as being proportional to the strength of connection, not the cost to travel between any pair of connected nodes. Therefore it is necessary to transform connection weights into some measure of cost or distance. One option is to simply take the reciprocal of each edge weight:  $A'_{ij} = \frac{1}{A_{ij}}$  or, for a network whose connection weights fall between 0 and 1,  $A'_{ij} = -\log(A_{ij})$ .

*Betweenness centrality.* The betweenness centrality,  $b_i$ , of a node measures the number of shortest paths that include node  $i$ .

*Characteristic path length.* The characteristic path length of a network is the average number of steps necessary to travel from any node  $i$  to any other node  $j$  and is calculated as:

$$L = \frac{1}{n} \sum_{i=1}^n \sum_{j=1, j \neq i}^n \frac{D_{ij}}{(n-1)}$$

*Global efficiency.* A measure closely related to characteristic path length is that of network efficiency, which scales between 0 and 1:

$$E = \frac{1}{n} \sum_{i=1}^n \sum_{j=1, j \neq i}^n \frac{D_{ij}^{-1}}{(n-1)}$$

*Modularity.* A network that exhibits clusters of densely interconnected nodes is said to be “modular.” One method used to score the quality of modules is the “modularity” function:

$$Q = \sum_{ij} B_{ij} \delta(g_i g_j)$$

Here,  $B_{ij} = A_{ij} - P_{ij}$ , where  $A_{ij}$  and  $P_{ij}$  are the observed and expected weight of the connection between nodes  $i$  and  $j$ , respectively,  $g_i$  is the module or cluster to which node  $i$  is assigned, and  $\delta(g_i g_j)$  is the Kronecker delta function which equals 1 if  $g_i = g_j$  and is zero otherwise. The value of  $Q$  is large when the positive elements of  $B_{ij}$  fall within communities – i.e. when the intra-modular connection density is much greater than expected. The value of  $B_{ij}$  depends upon the choice of null model which defines the expected connection weight,  $P_{ij}$ . A common choice is to define  $P_{ij} = \frac{s_i s_j}{2m}$ , where  $2m = \sum_i s_i$ . This definition corresponds to a null model where each node’s strength is preserved exactly, but where connections are otherwise made at random. Other definitions have been proposed as well, including the constant null model  $P_{ij} = \langle A_{ij} \rangle$  or, for spatially-embedded systems, the gravity model:  $P_{ij} = \frac{X_i X_j}{f(E_{ij})}$ , where  $X_i$  is some (positive) node-level property and  $f(E_{ij})$  is a function of the geometric distance between nodes  $i$  and  $j$ .

*Degree assortativity.* A network is said to exhibit “degree assortativity” if nodes tend to form connections to other nodes with similar degrees. This propensity can be quantified as the Pearson

correlation of stub degrees for each connection (Newman 2002). If this correlation is positive then a network is assortative (connections are formed between nodes of similar degree) and if the correlation is negative then the network is said to be disassortative (connection are made between nodes of dissimilar degree).

*Hub.* There is no single definition of a hub. Operationally, however, hubs tend to be defined as nodes with high degrees (they make many connections) and may also occupy a central position in the network. Here centrality can be determined by a measure such as betweenness centrality, though other centrality measures can be substituted.

*Rich club.* A rich club refers to a group of nodes whose degrees are all greater than  $\kappa$  and are also more densely connected to one another than what one would expect by chance. Formally, we identify rich clubs by first extracting the subgraph,  $\mathcal{G}'$ , comprising the set of nodes with  $k \geq \kappa$  and calculate its density,  $\phi(\kappa)$ , which is also known as the rich club coefficient. Next, we compare  $\phi(\kappa)$  against the null distribution of rich club coefficients obtained from an ensemble of networks whose links have been randomized but where each node's degree has been preserved. If  $\phi(\kappa)$  is much greater than any of the rich club coefficients in the null distribution then we state that for degree  $\kappa$  there is a statistically significant rich club.

## References:

- Achard S, Salvador R, Whitcher B, Suckling J, Bullmore ET (2006). A resilient, low-frequency small-world human brain functional network with highly connected association cortical hubs. *The Journal of Neuroscience*, 26(1), 63-72.
- Achard S, Bullmore ET (2007). Efficiency and cost of economical brain functional networks. *PLOS Computational Biology*, 3(2), e17.
- Ahn YY, Bagrow JP, Lehmann S (2010). Link communities reveal multiscale complexity in networks. *Nature*, 466(7307), 761-764.
- Ahn YY, Ahnert SE, Bagrow JP, Barabási AL (2011). Flavor network and the principles of food pairing. *Scientific Reports*, 1, 196.
- Alexander-Bloch A, Gogtay N, Meunier D, Birn R, Clasen L, Lalonde F, et al (2010). Disrupted modularity and local connectivity of brain functional networks in childhood-onset schizophrenia. *Frontiers in Systems Neuroscience*, 4(147), 1-16.
- Alexander-Bloch, A. F., Lambiotte, R., Roberts, B., R., Giedd, J., Gogtay, N., Bullmore, E. T., (2012). The discovery of population differences in network community structure: new methods and applications to brain functional networks in schizophrenia. *Neuroimage*. 59(4), 3889-3900.
- Allen EA, Damaraju E, Plis SM, Erhardt EB, Eichele T, Calhoun VD (2014). Tracking whole-brain connectivity dynamics in the resting state. *Cerebral Cortex*, 24(3), 663-676.
- Andersson JLR, Skare S (2002). A model-based method for retrospective correction of geometric distortions in diffusion-weighted EPI. *Neuroimage* 16(1), 177-199.
- Andrews-Hanna JR, Snyder AZ, Vincent JL, Lustig C, Head D, Raichle ME, et al (2007). Disruption of large-scale brain systems in advanced aging. *Neuron*, 56(5), 924-935.
- Avena-Koenigsberger A, Goñi J, Betzel RF, van den Heuvel MP, Griffa A, Hagmann P, et al (2014). Using Pareto optimality to explore the topology and dynamics of the human connectome. *Philosophical Transactions of the Royal Society B*, 369(1653), 20130530.
- Bailey A, Ventresca M, Ombuki-Berman B. [Automatic generation of graph models for complex networks by genetic programming] Proc. 14th international conference on genetic and evolutionary computation conference (GECCO '12) [711-718] (ACM, New York, 2012).

Baker JT, Holmes AJ, Masters GA, Yeo BTT, Krienen F, Buckner RL, et al (2013). Disruption of cortical association networks in schizophrenia and psychotic bipolar disorder. *JAMA Psychiatry*, 71(2), 109-118.

Barabási AL, Albert R (1999). Emergence of scaling in random networks. *Science*, 286(5439), 509-512.

Barabási AL, Oltvai ZN (2004). Network biology: understanding the cell's functional organization. *Nature Reviews Genetics*, 5(2), 101-113.

Barabási AL, Gulbahce N, Loscalzo J (2011). Network medicine: a network-based approach to human disease. *Nature Reviews Genetics*, 12(1), 56-68.

Barnea-Goraly N, Menon V, Eckert M, Tamm L, Bammer R, Karchemskiy A, et al (2005). White matter development during childhood and adolescence: a cross-sectional diffusion tensor imaging study. *Cerebral Cortex*, 15(12), 1848-1854.

Barthélemy M (2011). Spatial Networks. *Physics Reports*, 499(1), 1-101.

Basser PJ, Mattiello J, LeBihan D (1994). MR Diffusion tensor spectroscopy and imaging. *Biophysical Journal*, 66(1), 259.

Basser PJ, Pajevic S, Pierpaoli C, Duda J, Aldroubi A (2000). In vivo fiber tractography using DT-MRI data. *Magnetic Resonance in Medicine*, 44(4), 625-632.

Bassett DS, Greenfield DL, Meyer-Lindenberg A, Weinberger DR, Moore SW, Bullmore ET (2010). Efficient physical embedding of topologically complex information processing networks in brains and computer circuits. *PLOS Computational Biology*, 6(4), e1000748.

Bassett DS, Wymbs NF, Porter MA, Mucha PJ, Carlson JM, Grafton ST (2011). Dynamic reconfiguration of human brain networks during learning. *Proceedings of the National Academy of Sciences USA*, 108(18), 7641-7646.

Bassett DS, Yang M, Wymbs NF, Grafton ST. (2015). Learning-induced autonomy of sensorimotor systems. *Nature Neuroscience*, 18(5), 744-751.

Bazzi M, Porter MA, Williams S, McDonald M, Fenn DJ, Howison SD (2014). Community detection in temporal multilayer networks and its application to correlation matrices. arXiv preprint arXiv:1501.00040.

- Beckmann CF, DeLuca M, Devlin JT, Smith SM (2005). Investigations into resting-state connectivity using independent component analysis. *Philosophical Transactions of the Royal Society B*, 360, 1001-1013.
- Bellec P, Rosa-Neto P, Lyttelton OC, Benali H, Evans AC (2010). Multi-level bootstrap analysis of stable clusters in resting-state fMRI. *Neuroimage*, 51(3), 1126-1139.
- Benjamini Y, Hochberg Y (1995). Controlling the false discovery rate: A practical and powerful approach to multiple testing. *Journal of the Royal Statistical Society*, 57(1), 289-300.
- Betzal RF, Griffa A, Avena-Koenigsberger A, Goñi J, Thiran JP, Hagmann P, et al (2013). Multi-scale community organization of the human structural connectome and its relationship with resting-state functional connectivity. *Network Science*, 1(3), 353-373.
- Betzal RF, Byrge L, He Y, Goñi J, Zuo XN, Sporns O (2014). Changes in structural and functional connectivity among resting-state networks across the human lifespan. *Neuroimage*, 102(2), 345-357.
- Betzal RF, Mišić B, He Y, Rumschlag J, Zuo XN, Sporns O (2015a). Functional brain modules reconfigure at multiple scales across the human lifespan.
- Betzal RF, Avena-Koenigsberger, Goñi J, He Y, de Reus MA, Griffa A, et al (2015b). Generative models of the human connectome. *Neuroimage*.
- Blondel VD, Guillaume JL, Lambiotte R, Lefebvre E (2008). Fast unfolding of communities in large networks. *Journal of Statistical Mechanics: Theory and Experiment*, 2008(10), P10008.
- Bluhm RL, Osuch EA, Lanius RA, Boksman K, Neufeld RW, Theberge J, et al (2008). Default mode network connectivity: effects of age, sex, and analytic approach. *Neuroreport*, 19(8), 887-891.
- Börner K, Sanyal S, Vespignani A (2007). *Network Sciences*. *Annual Review of Information Science*, 41(1), 53-607.
- Buckner RL (2004). Memory and executive function in aging and AD: multiple factors that cause decline and reserve factors that compensate. *Neuron*, 44(1), 195-208.
- Buckner RJ, Sepulcre J, Talukdar T, Krienen FM, Liu H, Hedden T, et al (2009). Cortical hubs revealed by intrinsic functional connectivity: mapping, assessment of stability, and relation to Alzheimer's disease. *The Journal of Neuroscience*, 29(6), 1860-1873.

Buckner RL, Krienen FM, Yeo BT (2013). Opportunities and limitations of intrinsic functional connectivity MRI. *Nature Neuroscience*, 16(7), 832-837.

Bullmore ET, Sporns O (2009). Complex brain networks: graph theoretical analysis of structural and functional systems. *Nature Reviews Neuroscience*, 10(3), 186-198.

Bullmore ET, Sporns O (2012). The economy of brain network organization. *Nature Reviews Neuroscience*, 13(5), 336-349.

Cabeza R, Anderson ND, Locantore JK, McIntosh AR (2002). Aging gracefully: compensatory brain activity in high-performing older adults. *Neuroimage*, 17(3), 1394-1402.

Cao M, Wang JH, Dai ZJ, Cao XY, J LL, Fan FM, et al (2014). Topological organization of the human brain functional connectome across the lifespan. *Developmental Cognitive Neuroscience*, 7, 76-93.

Cammoun L, Gigandet X, Meskaldji D, Thiran JP, Sporns O, Do K, et al (2012). Mapping the human connectome at multiple scales with diffusion spectrum MRI. *J. Neurosci. Methods*, 203, 386-397.

Chai XJ, Castanon AN, Ongur D, Whitfield-Gabrieli S (2012). Anticorrelations in resting state networks without global signal regression. *Neuroimage*, 59(2), 1420-1428.

Chan MY, Park DC, Savalia NK, Petersen SE, Wig GS (2014). Decreased segregation of brain systems across the healthy adult lifespan. *Proceedings of the National Academy of Sciences USA*, 111(46), E4997-E5006.

Chang LC, Jones DK, Pierpaoli C (2005). RESTORE: robust estimation of tensors by outlier rejection. *Magnetic Resonance in Medicine*, 53(5), 1088-1095.

Chen Z, Liu M, Gross DW, Beaulieu C (2013). Graph theoretical analysis of developmental patterns of the white matter network. *Frontiers in Human Neuroscience*, 7, 716.

Cherniak C, Mokhtarzada Z, Rodriguez-Esteban R, Changizi K (2004). Global optimization of cerebral cortex layout. *Proceedings of the National Academy of Sciences USA*, 101(4), 1081-1086.

Cleveland WS, Devlin SJ (1988). Locally-weighted regression: An approach to regression analysis by local fitting. *Journal of the American Statistical Association*, 35(1), 596-610.

Cole MW, Bassett DS, Power JD, Braver TS, & Petersen SE (2014). Intrinsic and task-evoked network architectures of the human brain. *Neuron*, 83(1), 238-251.

Costa LDF, Rodrigues FA, Travieso G, Villas Boas PR (2007). Characterization of complex networks: A survey of measurements. *Advances in Physics*, 56(1), 167-242.

Craig AD (2009). How do you feel – now? The anterior insula and human awareness. *Nature Reviews Neuroscience*, 10(1), 59-70.

Craik FI, Bialystok E (2006). Cognition through the lifespan: mechanisms of change. *Trends in Cognitive Sciences*, 10(3), 131-138.

Crossley NA, Mechelli A, Vértes PE, Winton-Brown TT, Patel AX, Ginestet CE, et al (2013). Cognitive relevance of the community structure of the human brain functional coactivation network. *Proceedings of the National Academy of Sciences USA*, 110(28), 11583-11588.

da F Costa L, Kaiser M, Hilgetag CC (2007). Predicting the connectivity of primate cortical networks from topological and spatial node properties. *BMC Systems Biology*, 1(1), 16.

Dall J, Christensen M (2002). Random geometric graphs. *Physical Review E*, 66(1), 016121.

Deco G, Jirsa VK, McIntosh AR (2010). Emerging concepts for the dynamical organization of resting-state activity in the brain. *Nature Reviews Neuroscience*, 12(1), 43-56.

de Reus MA, van den Heuvel MP (2014). Simulated rich club lesioning in brain networks: a scaffold for communication and integration? *Frontiers in Human Neuroscience*, 8, 647.

D'Esposito, M., Zarahn, E., Aguirre, G. K., Rypma, B. (1999). The effect of normal aging on the coupling of neural activity to the BOLD hemodynamic response. *Neuroimage*, 10(1), 6-14.

D'Esposito, M., Deouell, L. Y., Gazzaley, A. (2003). Alterations in the BOLD fMRI signal with ageing and disease: a challenge for neuroimaging. *Nature Reviews Neuroscience*, 4, 863-872.

Destrieux C, Fischl B, Dale A, Halgren E (2010). Automatic parcellation of human cortical gyri and sulci using standard anatomical nomenclature. *Neuroimage*, 53(1), 1-15.

Dijkstra EW (1959). A note on two problems in connexion with graphs. *Numerische mathematik*, 1(1), 269-271.



Dosenbach NU, Nardos B, Cohen AL, Fair DA, Power JD, Church JD, et al (2010). Prediction of individual brain maturity using fMRI. *Science*, 329(5997), 1358-1361.

Douaud G, Groves AR, Tamnes CK, Westlye LT, Duff EP, Engvig, A. et al (2014). A common brain network links development, aging, and vulnerability to disease. *Proceedings of the National Academy of Sciences USA*. 111(49), 17648-17653.

Doucet G, Naveau M, Petit L, Delcroix N, Zago L, Crivello F, et al (2011). Brain activity at rest: a multiscale hierarchical functional organization. *Journal of Neurophysiology*, 105(6), 2753-2763.

Ercsey-Ravasz M, Markov NT, Lamy C, Van Essen DC, Knoblauch K, Toroczkai Z, et al (2013). A predictive network model of cerebral cortical connectivity based on a distance rule. *Neuron*, 80(1), 184-197.

Estrada E, Hatano N (2008). Communicability in complex networks. *Physical Review E*, 77(3), 036111.

Fair DA, Dosenbach NU, Church JA, Cohen AL, Brahmbhatt S, Miezin FM, et al (2007). Development of distinct control networks through segregation and integration. *Proceedings of the National Academy of Sciences USA* 104(33), 13507-13512.

Fair DA, Cohen AL, Dosenbach NU, Church JA, Miezin FM, Barch DM, et al (2008). The maturing architecture of the brain's default network. *Proceedings of the National Academy of Sciences USA* 105(10), 4028-4032.

Fair DA, Cohen AL, Power JD, Dosenbach NUF, Church JA, Miezin FM, et al (2009). Functional brain networks develop from a "local to distributed" organization. *PLOS Computational Biology*, 5(5), e1000381.

Ferreira LK, Busatto GF. (2013). Resting-state functional connectivity in normal brain aging. *Neuroscience & Biobehavioral Reviews*, 37(3), 384-400.

Fornito A, Zalesky A, Bullmore ET (2010). Network scaling effects in graph analytic studies of human resting-state fMRI data. *Frontiers in Systems Neuroscience*, 4, 22.

Fornito A, Zalesky A, Breakspear M (2015). The connectomics of brain disorders. *Nature Reviews Neuroscience*, 16(3), 159-172.

Fortunato S, Barthelemy M (2007). Resolution limit in community detection. *Proceedings of the National Academy of Sciences USA*, 104(1), 36-41.

- Fortunato S (2010). Community detection in graphs. *Physics Reports*, 486(3), 75-174.
- Fransson P, Skiöld B, Horsch S, Nordell A, Blennow M, Lagercrantz H, et al (2007). Resting-state networks in the infant brain. *Proceedings of the National Academy of Sciences USA*, 104(39):15541-15536.
- Fransson P, Marrelec G (2008). The precuneus/posterior cingulate cortex plays a pivotal role in the default mode network: evidence from a partial correlation network analysis. *Neuroimage*, 42(3), 1178-1184.
- Friston KJ, Williams S, Howard R, Frackowiak RS, Turner R (1996). Movement-related effects in fMRI time-series. *Magnetic Resonance in Medicine*, 35, 346-355.
- Friston KJ, Harrison L, Penny W (2003). Dynamic causal modeling. *Neuroimage*, 19(4), 1273-1302.
- Friston K (2011). Functional and effective connectivity: a review. *Brain Connectivity*, 1(1), 13-36.
- Geerligs L, Renken RJ, Saliassi E, Maurits NM, Lorist MM (2014). A brain-wide study of age-related changes in functional connectivity. *Cerebral Cortex*, doi: 10.1093/cercor/bhu012.
- Glasser MF, Sotiropoulos SN, Wilson JA, Coalson TS, Fischl B, Andersson JL, et al (2013). The minimal preprocessing pipelines for the Human Connectome Project. *Neuroimage*, 80(15), 105-124.
- Golland Y, Golland P, Bentin S, Malach R (2008). Data-driven clustering reveals a fundamental subdivision of the human cortex into two global systems. *Neuropsychologia*, 46, 540-553.
- Goñi J, Avena-Koenigsberger A, Velez de Mendizabal N, van den Heuvel MP, Betzel RF, Sporns O (2013). Exploring the morphospace of communication efficiency in complex networks. *PLOS ONE*, 8(3), e58070.
- Goñi J, van den Heuvel MP, Avena-Koenigsberger A, Velez de Mendizabal N, Betzel RF, Griffa A, et al (2014). Resting-brain functional connectivity predicted by analytic measures of network communication. *Proceedings of the National Academy of Sciences USA*, 111(2), 833-838.
- Gong G, He Y, Concha L, Lebel C, Gross DW, Evans AC, et al (2009). Mapping anatomical connectivity patterns of human cerebral cortex using in vivo diffusion tensor imaging tractography. *Cerebral Cortex*, 19(3), 524-536.

Good BH, de Montjoye YA, Clauset A (2010). Performance of modularity maximization in practical contexts. *Physical Review E*, 81(4), 056106.

Grady, C. L. (2012). The cognitive neuroscience of ageing. *Nature Reviews Neuroscience*. 13, 491-502.

Guimera R, Amaral LAN (2005). Functional cartography of complex metabolic networks. *Nature*, 433(7028), 895-900.

Hagmann P, Kurant M, Gigandet X, Thiran P, Wedeen VJ, Meuli R, et al (2007). Mapping whole-brain structural networks with diffusion MRI. *PLOS ONE*, 2(7), e597.

Hagmann P, Cammoun L, Gigandet X, Meuli R, Honey CJ, Wedeen VJ, et al (2008). Mapping the structural core of human cerebral cortex. *PLOS Biology*, 6(7), e159.

Haimovici A, Tagliazucchi E, Balenzuela P, Chialvo DR (2013). Brain organization into resting state networks emerges at criticality on a model of the human connectome. *Physical Review Letters*, 110(17), 178101.

Hämäläinen M, Hari R, Ilmoniemi RJ, Knuutila J, OV Lounasmaa (1993). Magnetoencephalography – theory, instrumentation, and applications to noninvasive studies of the working human brain. *Reviews of Modern Physics*, 65(2), 413.

Handwerker DA, Gonzalez-Castillo J, D’Esposito M, Bandettini PA, (2012). The continuing challenge of understanding and modeling hemodynamic variation in fMRI. *Neuroimage*. 62(2), 1017-1023.

Hawellek DJ, Hipp JF, Lewis CM, Corbetta M, Engel AK (2011). Increased functional connectivity indicates the severity of cognitive impairment in multiple sclerosis. *Proceedings of the National Academy of Sciences USA*, 108(47), 19066-19071.

He Y, Wang J, Wang L, Chen ZJ, Han C, Yang H, et al (2009). Uncovering intrinsic modular organization of spontaneous brain activity in humans. *PLOS ONE*, 4(4), e5226.

Henderson JA, Robinson PA (2013). Using geometry to uncover relationships between isotropy, homogeneity, and modularity in cortical connectivity. *Brain Connectivity*, 3(4), 423-437.

Hermundstad AM, Bassett DS, Brown KS, Aminoff EM, Clewett D, Freeman S, et al (2013). Structural foundations of resting-state and task-based functional connectivity in the human brain. *Proceedings of the National Academy of Sciences USA*, 110(5), 6169-6174.

Hertzog C, Kramer AF, Wilson RS, Lindenberger U (2009). Enrichment effects on adult cognitive development: can the functional capacity of older adults be preserved and enhanced? *Psychological Science in the Public Interest*, 9(1), 1-65.

Hidalgo CA, Hausmann R (2009). The building blocks of economic complexity. *Proceedings of the National Academy of Sciences USA*, 106(26), 10570-10575.

Hirschberger M, Qi Y, Steuer RE (2004). Randomly generating portfolio-selection covariance matrices with specified distributional characteristics. *European Journal of Operational Research*, 177(3), 1610-1625.

Honey CJ, Kötter R, Breakspear M, Sporns O (2007). Network structure of cerebral cortex shapes functional connectivity on multiple time scales. *Proceedings of the National Academy of Sciences USA*, 104(24), 10240-10245.

Honey CJ, Sporns O, Cammoun L, Gigandet X, Thiran JP, Meuli R, et al (2009). Predicting human resting-state functional connectivity from structural connectivity. *Proceedings of the National Academy of Sciences USA* 106(6), 2035-2040.

Hutchinson RM, Wornelsdorf T, Allen EA, Bandettini PA, Calhoun VD, Corbetta M, et al (2013). Dynamic functional connectivity: promise, issues, and interpretations. *Neuroimage*, 80, 360-378.

Jiang L, Xu T, He Y, Hou XH, Wang J, Cao XY, et al (2014). Toward neurobiological characterization of functional homogeneity in the human cortex: regional variation, morphological association and functional covariance network organization. *Brain Structure and Function*, 1-23.

Jolles DD, van Buchem MA, Crone EA, Rombouts SA (2013). Functional brain connectivity at rest changes after working memory training. *Human Brain Mapping*, 34(2), 396-406.

Jutla IS, Jeub LG, Mucha PJ. A generalized Louvain method for community detection implemented in MATLAB. URL <http://netwiki.amath.unc.edu/GenLouvain> (2011).

Kaiser M, Hilgetag CC (2004a). Spatial growth of real-world networks. *Physical Review E*, 69(3), 036103.

Kaiser M, Hilgetag CC (2004b). Modeling the development of cortical systems networks. *Neurocomputing*, 58, 297-302.

Kaiser M, Hilgetag CC (2006). Nonoptimal component placement, but short processing paths, due to long-distance projections in neural systems. *PLOS Computational Biology*, 2(7), e95.

Kaiser M, Hilgetag CC (2007). Development of multi-cluster cortical networks by time windows for spatial growth. *Neurocomputing*, 70(10-12), 1829-1832.

Kaiser M, Hilgetag CC, Van Ooyen A (2009). A simple rule for axon outgrowth and synaptic competition generates realistic connection lengths and filling fractions. *Cerebral Cortex*, 19(12), 3001-3010.

Kaiser M, Hilgetag CC, Kötter R (2010). Hierarchy and dynamics in neural networks. *Frontiers in Neuroinformatics*, 4(112), 1-3.

Kelly AMC, Di Martino A, Uddin LQ, Shehzad Z, Gee DG, Reiss PT, et al (2009). Development of anterior cingulate functional connectivity from late childhood to early adulthood. *Cerebral Cortex*, 19(3), 640-657.

Kivelä M, Arenas A, Barthelemy M, Gleeson JP, Moreno Y, Porter MA (2014). Multilayer networks. *Journal of Complex Networks*, 2(3), 203-271.

Klein TA, Endrass T, Kathmann N, Neumann J, Von Cramon DY, Ullsperger M (2007). Neural correlates of error awareness. *Neuroimage*, 34(4), 1774-1781.

Klimm F, Bassett DS, Carlson JM, Mucha PJ (2014). Resolving structural variability in network models and the brain. *PLOS Computational Biology*, 10(3), e1003491.

Kochunov P, Glahn DC, Lancaster J, Thompson PM, Kochunov V, Rogers B, et al (2011). Fractional anisotropy of cerebral white matter and thickness of cortical gray matter across the lifespan. *Neuroimage*, 58(1), 41-49.

Krioukov D, Papadopoulos F, Kitsak M, Vahdat A, Boguña M (2010). Hyperbolic geometry of complex networks. *Physical Review E*, 82(3), 036106.

Kumar R, Raghavan P, Rajagopalan S, Sivakumar D, Tomkins A, Upfal E (2000). Stochastic models for the web graph. In *Foundations of Computer Science, 2000. Proceedings. 41st Annual Symposium on* (pp. 57-65). IEEE.

Lancichinetti A, Radicchi F, Ramasco JJ, Fortunato S (2011). Finding statistically significant communities in networks. *PLOS ONE*, 6(4), e18961.

- Lancichinetti A, Fortunato S (2011). Limits of modularity maximization in community detection. *Physical Review E*, 84(6), 066122.
- Lancichinetti A, Fortunato S (2012). Consensus clustering in complex networks. *Scientific Reports*, 2, 336.
- Latora V , Marchiori M (2001). Efficient behavior of small-world networks. *Physical Review Letters*, 87(19), 198701.
- Laughlin SB, Sejnowski TJ (2003). Communication in Neuronal Networks. *Science*, 301(5641), 1870-1874.
- Leskovec J, Lang KJ, Dasgupta A, Mahoney MW (2008, April). Statistical properties of community structure in large social and information networks. In *Proceedings of the 17th international conference on World Wide Web* (pp. 695-704). ACM.
- Lewis CM, Baldassarre A, Comitteri G, Romani GL, Corbetta M (2009). Learning sculpts the spontaneous activity of the resting human brain. *Proceedings of the National Academy of Sciences USA*, 106(41), 17558-17563.
- Li SC, Lindenberger U, Sikström S (2001). Aging cognition: from neuromodulation to representation. *Trends in Cognitive Sciences*, 5(11), 479-486.
- Li SC, Brehmer Y, Shing YL, Werkle-Bergner M, Lindenberger U (2006). Neuromodularity of associative and organizational plasticity across the lifes span: Empirical evidence and neurocomputational modeling. *Neuroscience & Biobehavioral Reviews*, 30, 775-790.
- Lim S, Han CE, Uhlhaas PJ, Kaiser M (2013). Preferential detachment during human brain development: Age- and sex-specific structural connectivity in diffusion tensor imaging (DTI) data. *Cerebral Cortex*, doi:10.1093/cercor/bht333.
- Lim S, Kaiser M (2015). Developmental time windows for axon growth influence neuronal network topology. *Biological Cybernetics*, 109(2), 275-286.
- Logothetis NK, Pauls J, Augath M, Trinath T, Oeltermann A (2001). Neurophysiological investigation of the basis of the fMRI signal. *Nature*, 412(6843), 150-157.

- Lohse C, Bassett DS, Lim KO, Carlson JM (2013). Resolving structure in human brain organization: Identifying mesoscale organization in weighted network representations. *PLOS Computational Biology*, 10(10), e1003712.
- Ma L, Narayana S, Robin DA, Fox PT, Xiong J (2011). Changes occur in resting state network of motor system during 4weeks of motor skill learning. *Neuroimage*, 58(1), 226-233.
- MacMahon M, Garlaschelli D (2015). Community detection for correlation matrices. *Physical Review X*, 5, 021006.
- Maslov S, Sneppen K (2002). Specificity and stability in topology of protein networks. *Science*, 296(5569), 910-913.
- McIntosh A, Mišić B (2013). Multivariate statistical analysis for neuroimaging data. *Annual Review of Psychology*, 64, 499-525.
- Meier TB, Desphande AS, Vergun S, Nair VA, Song J, Biswal BB, et al (2012). Support vector machine classification and characterization of age-related reorganization of functional brain networks. *Neuroimage*, 60(1), 601-613.
- Menezes T, Roth C (2014). Symbolic regression of generative network models. *Scientific Reports*, 4, 1-7.
- Menon V, Uddin L (2010). Saliency, switching, attention and control: a network model of insula function. *Brain Structure and Function*, 214(5-6), 655-667.
- Meunier D, Achard S, Morcom A, Bullmore E (2009a). Age-related changes in modular organization of human brain functional networks. *Neuroimage*, 44, 715-723
- Meunier D, Lambiotte R, Fornito A, Ersche KD, Bullmore ET (2009b). Hierarchical modularity in human brain functional networks. *Frontiers in Neuroinformatics*, 3(37), 1-12.
- Meunier D, Lambiotte R, Bullmore ET (2010). Modular and hierarchically modular organization of brain networks. *Frontiers in Neuroscience*, 4, 200.
- Middendorf M, Ziv E, Wiggins CH (2005). Inferring network mechanisms: the drosophila melanogaster protein interaction network. *Proceedings of the National Academy of Sciences USA*, 102(9), 3192-3197.

Mišić B, Betzel RF, Nematzadeh A, Goñi J, Griffa A, Hagmann P, et al (2015). Cooperative and competitive spreading dynamics on the human connectome. *Neuron*, 86(6), 1518-1529.

Mitchison G (1991). Neuronal branching patterns and the economy of cortical wiring. *Philosophical Transactions of the Royal Society B*, 245(1313), 151-158.

Mori S, Crain BJ, Chacko VP, van Zijl PC (1999). Three-dimensional tracking of axonal projections in the brain by magnetic resonance imaging. *Annals of Neurology*, 45(2), 265-269.

Mori S, van Zijl PC (2002). Fiber tracking: principles and strategies – a technical review. *NMR in Biomedicine*, 15(7-8), 468-480.

Mori S (2002). Two and three-dimensional analyses of brain white matter architecture using diffusion imaging. *CNS Spectrums*, 7(7), 529-534.

Mucha PJ, Richardson T, Macon K, Porter MA, et al (2010). Community structure in time-dependent, multiscale, and multiplex networks. *Science*, 328(5980), 876-878.

Murphy K, Birn RM, Handwerker DA, Jones TB, Bandettini PA (2009). The impact of global signal regression on resting state correlations: are anti-correlated networks introduced? *Neuroimage*, 44(3), 893-905.

Mwangi B, Hasan KM, Soares JC (2013). Prediction of individual subject's age across the human lifespan using diffusion tensor imaging: A machine learning approach. *Neuroimage*, 75(15), 58-67.

Newman MEJ (2002). Assortative mixing in networks. *Physical Review Letters*, 89(20), 208701.

Newman MEJ, Girvan M (2004). Finding and evaluating community structure in networks. *Physical Review E*, 69(2), 026113.

Newman MEJ (2006). Modularity and community structure in network. *Proceedings of the National Academy of Sciences USA*, 103(23), 8577-8582.

Newman MEJ (2012). Communities, modules and large-scale structure in networks. *Nature Physics*, 8(1), 25-31.

Nicosia V, Vértés PE, Schafer WR, Latora V, Bullmore ET (2013). Phase transition in the economically modeled growth of a cellular nervous system. *Proceedings of the National Academy of Sciences USA*, 110(19), 7880-7885.



Nooner KB, Colcombe SL, Tobe RH, Mennes M, Benedict MM, Moreno AL, et al (2012). The NKI-Rockland sample: A model for accelerating the pace of discover science in psychiatry. *Frontiers in Neuroscience*, 6, 152.

Nunez PL, Srinivasan R (2006). *Electric fields of the brain: the neurophysics of EEG*. Oxford University Press.

Onada K, Ishihara M, Yamaguchi S (2012). Decreased functional connectivity by aging is associated with cognitive decline. *The Journal of Cognitive Neuroscience*, 24(11), 2186-2198.

O'Reilly JX, Croxson PL, Jbabdi S, Sallet J, Noonan MP, Mars RB, et al (2013). Causal effect of disconnection lesions on interhemispheric functional connectivity in rhesus monkeys. *Proceedings of the National Academy of Sciences USA*. 110(34), 13982-13987.

O'Sullivan MRCP, Jones DK, Summers PE, Morris RG, Williams SCR, Markus HS (2001). Evidence for cortical “disconnections” as a mechanism of age-related cognitive decline. *Neurology*, 57(4), 632-638.

Palla G, Derenyi I, Farkas I, Vicsek T (2005). Uncovering overlapping community structure of complex networks in nature and society. *Nature*, 435(7043), 814-818.

Papadopoulos F, Kitsak M, Serrano MA, Boguña M, Krioukov D (2012). Popularity versus similarity in growing networks. *Nature*, 489, 537-540.

Park J, Carp J, Hebrank A, Park DC, Polk TA (2010). Neural specificity predicts fluid processing ability in older adults. *The Journal of Neuroscience*, 30(27), 9253-9259.

Pascual-Leone A, Amedi A, Fregni F, Merabet LB (2005). The plastic human brain cortex. *Annual Reviews of Neuroscience*, 28, 377-401.

Porter MA, Onnela JP, Mucha PJ (2009). Communities in networks. *Notices of the AMS*, 56(9), 1082-1097.

Power JD, Fair DA, Schlaggar BL, Petersen SE (2010). The development of human functional brain networks. *Neuron*, 67(5), 735-748.

Power JD, Cohen AL, Nelson SM, Wig GS, Barnes KA, Church JA, et al (2011). Functional network organization of the human brain. *Neuron*, 72(4), 665-678.

Power JD, Barnes KA, Snyder AZ, Schlaggar BL, Petersen SE (2012). Spurious but systematic correlations in functional connectivity MRI networks arise from subject motion. *Neuroimage*, 59(3), 2142-2154.

Power JD, Mitra A, Laumann TO, Snyder AZ, Schlaggar BL, Petersen SE (2014). Methods to detect, characterize, and remove motion artifact in resting state fMRI. *Neuroimage*, 84, 320-341.

Power JD, Schlaggar BL, Petersen SE (2015). Recent progress and outstanding issues in motion correction in resting state fMRI. *Neuroimage*, 102, 536-551.

Ravasz E, Somera AL, Mongru DA, Oltvai ZN, Barabási AL (2002). Hierarchical organization of modularity in metabolic networks. *Science*, 30(297), 1551-1555.

Reichardt J, Bornholdt S, (2006). Statistical mechanics of community detection. *Physical Review E*, 74(1), 016110.

Reveley C, Seth AK, Pierpaoli C, Silva AC, Yu D, Saunders RC, et al (2015). Superficial white matter fiber systems impede detection of long-range cortical connections in diffusion MR tractography. *Proceedings of the National Academy of Sciences USA*, doi:10.1073/pnas.1418198112.

Richards JE, Sanchez C, Phillips-Meek M, Xie W (2015). A database of age-appropriate average MRI templates. *Neuroimage*, doi:10.1016/j.neuroimage.2015.04.055.

Rogers BP, Morgan VL, Newton AT, Gore JC (2007). Assessing functional connectivity in the human brain by fMRI. *Magnetic Resonance Imaging*, 25(10), 1347-1357.

Rosvall M, Bergstrom CT (2008). Maps of random walks on complex networks reveal community structure. *Proceedings of the National Academy of Sciences USA*, 105(4), 1118-1123.

Rubinov M, Sporns O (2010). Complex network measures of brain connectivity: uses and interpretations. *Neuroimage*, 52(3), 1059-1069.

Rubinov M, Sporns O (2011). Weight-conserving characterization of complex function brain networks. *Neuroimage*, 56(4), 2068-2079.

Sambataro F, Murty VP, Callicott JH, Tan HY, Das S, Weinberger DR, et al (2010). Age-related alterations in default mode network: Impact on working memory performance. *Neurobiology of Aging*, 31(5), 839-852.

Samu D, Seth AK, Nowotny T (2014). Influence of wiring cost on the large-scale architecture of human cortical connectivity. *PLOS Computational Biology*, 10(4), e1003557.

Satterthwaite TD, Wolf DA, Loughead J, Ruparel K, Elliot MA, Kaonarson H, et al (2012). Impact of in-scanner head motion on multiple measures of functional connectivity: relevance for studies of neurodevelopment in youth. *Neuroimage*, 60(1), 623-632.

Satterthwaite TD, Elliot MA, Gerraty RT, Ruparel K, Loughead J, Calkins ME, et al (2013). An Improved Framework for Confound Regression and Filtering for Control of Motion Artifact in the Preprocessing of Resting-State Functional Connectivity Data. *Neuroimage*, 64(1), 240-256.

Schwarz AJ, McGoñigle J (2011). Negative edges and soft thresholding in complex network analysis of functional connectivity data. *Neuroimage*, 55(3), 1132-1146.

Sepulcre J, Sabuncu MR, Yeo TB, Liu H, Johnson KA (2012). Stepwise connectivity of the modal cortex reveals the multimodal organization of the human brain. *The Journal of Neuroscience*, 32(31), 10649-10661.

Seth AK (2010). A MATLAB toolbox for Granger causal connectivity analysis. *Journal of Neuroscience Methods*, 186(2), 262-273.

Smith SM, Fox PT, Miller KL, Glahn DC, Fox PM, Mackay CE, et al (2009). Correspondence of the brain's functional architecture during activation and rest. *Proceedings of the National Academy of Sciences, USA*, 106(31), 13040-13045.

Smith SM, Miller KL, Salimi-Khorshidi, Webster M, Beckmann CF, Nichols TE, et al (2011). Network modeling methods for fMRI. *Neuroimage*, 54(2), 875-891.

Smyser CD, Inder TE, Shimony JS, Hill JS, Degnan AJ, Snyder AZ, et al (2010). Longitudinal analysis of neural network development in preterm infants. *Cerebral Cortex*, 20(12), 2852-2862.

Solé RV, Pastor Satorras R, Smith E, Kepler TB (2002). A model of large-scale proteome evolution. *Advances in Complex Systems*, 5(1), 43-54.

Song HF, Kennedy H, Wang XJ (2014). Spatial embedding of structural similarity in the cerebral cortex. *Proceedings of the National Academy of Sciences USA*, 111(46), 16580-16585.

Sowell ER, Peterson BS, Thompason PM, Welcome SE, Henkenius AL, Toga AW (2003). Mapping cortical change across the human lifespan. *Nature Neuroscience*, 6(3), 309-315.

Sporns O (2011). *Networks of the brain*. MIT Press.

Sporns O (2014b). Contributions and challenges for network models in cognitive neuroscience. *Nature Reviews Neuroscience*, 17(4), 1-9. doi:10.1038/nrn.3690.

Sporns O, Betzel RF (2015). Modular brain networks. *Annual Reviews of Psychology*

Sullivan EV, Pfefferbaum A (2006). Diffusion tensor imaging and aging. *Neuroscience & Biobehavioral Reviews*, 30, 49-761.

Supekar K, Musen M, Menon V (2009). Development of large-scale functional brain networks in children. *PLOS Biology*, 7(7), e1000157.

Supekar K, Uddin LQ, Prater K, Amin H, Greicius MD, Menon V. (2010). Development of functional and structural connectivity within the default mode network in young children. *Neuroimage*, 52(1), 290-301.

Thomas C, Frank QY, Irfanoglu MO, Modi P, Saleem KS, Leopold DA, et al (2014). Anatomical accuracy of brain connections derived from diffusion MRI tractography is inherently limited. *Proceedings of the National Academy of Sciences USA*, 111(46), 16574-16579.

Tomasi D, Volkow ND (2012). Aging and functional brain networks. *Molecular Psychiatry*, 17(5), 549-558.

Tournier JD, Mori S, Leemans A (2011). Diffusion tensor imaging and beyond. *Magnetic Resonance in Medicine*, 65(6), 1532-1556.

Traag VA, van Dooren P, Nesterov Y (2011). Narrow scope for resolution-limit-free community detection. *Physical Review E*, 84(1), 016114.

Traud AL, Kelsic ED, Mucha PJ, Porter MA (2011). Comparing community structure to characteristics in online collegiate social networks. *SIAM Reviews*, 53(3), 526-543.

Utevsky, A. V., Smith D. V., Huettel, S. A. (2014). Precuneus is a functional core of the default-mode network. *The Journal of Neuroscience*, 34(3), 932-940.

van den Heuvel MP, Sporns O (2011). Rich-club organization of the human connectome. *The Journal of Neuroscience*, 31(44), 15775-15786.

van den Heuvel MP, Sporns O (2013). Network hubs in the human brain. *Trends in Cognitive Sciences*, 17(12), 683-696.

van den Heuvel MP, Fornito A (2014). Brain networks in schizophrenia. *Neuropsychological Review*, 24(1), 32-48.

van den Heuvel MP, Kersbergen KJ, de Reus MA, Keunen, K, Kahn, RS, Groenendaal F, et al (2014). The neonatal connectome during preterm brain development. *Cerebral Cortex*. bhu095.

Van Essen D, Ugurbil K, Auerbach E, Barch D, Behrens T, Bucholz R, et al (2012). The Human Connectome Project: A data acquisition perspective. *Neuroimage*, 62(4), 2222-2231.

Vann SD, Aggleton JP, Maguire EA (2009). What does the retrosplenial cortex do? *Nature Reviews Neuroscience*, 10(11), 792-802.

Vázquez A, Flammini A, Maritan A, Vespignani A (2002). Modeling of protein interaction networks. *Complexus*, 1(1), 38-44.

Vértes PE, Alexander-Bloch AF, Gogtay N, Giedd JN, Rapoport JL et al (2012). Simple models of human brain functional networks. *Proceedings of the National Academy of Sciences USA*, 109(15), 5868-5873.

Wang L, Su L, Shen H, Hu D (2012). Decoding lifespan changes of the human brain using resting-state functional connectivity MRI. *PLOS ONE*, 7(8), e44530.

Wang Z, Chen LM, Négyessy L, Friedman RM, Mishra A, Gore JC, et al (2013). The Relationship of Anatomical and Functional Connectivity to Resting-State Connectivity in Primate Somatosensory Cortex. *Neuron*, 78(6), 1116-1126.

Watts DJ, Strogatz SH (1998). Collective dynamics of ‘small-world’ networks. *Nature*, 393(6684), 440-442.

Wilcoxon F (1945). Individual comparisons by ranking methods. *Biometrics bulletin*, 80-83.

Xu T, Yang Z, Jiang L, Xing XX, Zuo XN (2015). A connectome computation system for discovery science of brain. *Science Bulletin*, 60(1), 86-95.

Yan L, Zhuo Y, Wang B, Wang DJ (2011). Loss of coherence of low frequency fluctuations of BOLD fMRI in visual cortex of healthy aged subjects. *The Open Neuroimaging Journal*, 5, 105-111.

Yan CG, Cheung B, Kelly C, Colcombe S, Craddock RC, Di Martino A, et al (2013). A comprehensive assessment of regional variation in the impact of head movements on functional connectomics. *Neuroimage*, 76(1), 183-201.

Yang Z, Chang C, Xu T, Jang L, Handwerker DA, Castellanos FX, et al (2014). Connectivity trajectory across lifespan differentiates the precuneus from the default network. *Neuroimage*, 89, 45-56.

Yap PT, Fan Y, Chen Y, Gilmore JH, Lin W, Shen D (2011). Development trends of white matter connectivity in the first years of life. *PLOS ONE*, 6(9), e24678.

Yeh FC, Wedeen V, Tseng W (2010). Generalized q-sampling imaging. *IEEE Transactions on Medical Imaging*, 29, 1625-1635.

Yeo BTT, Krienen FM, Sepulcre J, Sabuncu MR, Lashkari D, Hollinshead M, et al (2011). The organization of the human cerebral cortex estimated by intrinsic functional connectivity. *Journal of Neurophysiology*, 106(3), 1125-1165.

Zalesky A, Fornito A, Harding IH, Cocchi L, Yücel M, Pantelis C, et al (2010). Whole-brain anatomical networks: does the choice of nodes matter?. *Neuroimage*, 50(3), 970-983.

Zalesky A, Fornito A, Bullmore E (2012). On the use of correlation as a measure of network connectivity. *Neuroimage*, 60(4), 2096-1206.

Zhang B, Horvath S (2005). A general framework for weighted gene co-expression network analysis. *Statistical Applications in Genetics and Molecular Biology*, 4(1), 1128.

Zhang P, Moore C (2014). Scalable detection of statistically significant communities and hierarchies, using message passing for modularity. *Proceedings of the National Academy of Sciences USA*, 111(51) 18144-18149.

Zuo XN, Kelly C, Di Martino A, Mennes M, Margulies DS, Bangaru S, et al (2010). Growing together and growing apart: Regional and sex differences in the lifespan developmental trajectories of functional homotopy. *The Journal of Neuroscience*, 30(45), 15034-15043.

Zuo XN, Ehmke R, Mennes M, Imperati D, Castellanos FX, Sporns O, et al (2012). Network centrality in the human functional connectome. *Cerebral Cortex*, 22(8), 1862-1875.

Zuo XN, Anderson JS, Bellec P, Birn MR, Biswal BH, Blautsik J, et al (2014). An open science resource for establishing reliability and reproducibility in functional connectomics. *Scientific Data*, 1, 140049.

Zuo XN, X XX (2014). Test-retest reliabilities of resting-state fMRI measurements in human brain functional connectomics: A systems neuroscience perspective. *Neuroscience & Biobehavioral Reviews*, 45, 100-118.

## RICHARD F. BETZEL – CURRICULUM VITAE

---

### RESEARCH INTERESTS

---

My research program focuses on characterizing the features of the human connectome and the relationship of these features to large-scale brain dynamics as well as human behavior, disease, and cognition. A major component of this research involves modeling the human brain as a complex network, and analyzing this network with a set of mathematical tools that includes elements of graph theory, information theory, and dynamical systems theory.

### CONTACT

---

Richard Betzel, M.S., Ba.  
Department of Psychological and Brain Sciences  
1101 East 10<sup>th</sup> Street  
Indiana University  
Bloomington, IN 47405

Phone: 440-315-6142

Email: richard [dot] betzel [at] gmail [dot] com

Twitter: @richardfbetzel

Homepage: <http://pages.iu.edu/~rbetzel/>

### EDUCATION

---

2003-2007	Undergraduate studies in Physics at Oberlin College, Oberlin, OH
2008-2010	Master of Science in Human Biomechanics at Indiana University Research Advisor: Prof. Jesus Dapena
2012-2015	Dual Ph.D. in Psychological and Brain Sciences (Cognitive Neuroscience concentration) and Program in Cognitive Science Dissertation: Age-related changes in human anatomical and functional brain networks. Research Advisor: Prof. Olaf Sporns
2015-Pres	Postdoctoral Researcher at University of Pennsylvania, Philadelphia, PA Postdoctoral Advisor: Prof. Danielle S. Bassett

### HONORS AND AWARDS

---

2008-2009	HPER Fellowship
2009-2010	Cooper Scholarship
2012-Pres	National Science Foundation Integrative Graduate Education and Research Traineeship (IGERT) in "The Dynamics of Brain-Body-Environment Systems"
2013	IGERT Travel Award to Cambridge University, Cambridge, UK (\$4500)
2014	IGERT Travel Award to Annual Meeting of SfN, Washington, DC (\$2200)
2014	IGERT Travel Award to Annual Meeting of OHBM, Honolulu, HA (\$3500)



2014 Departmental Commendation on Qualifying Examination (June 24 2014).  
2015 IGERT Travel Award to NetSci2015, Zaragoza, Spain (\$3000)  
2015 IGERT Poster Showcase voted 3<sup>rd</sup> Place (“Generative Models of Human Connectome”)  
2015 J.R. Kantor Graduate Award (IU PBS)

#### PROFESSIONAL MEMBERSHIP

---

2011- Pres The Society for Neuroscience  
2014- Pres Organization for Human Brain Mapping  
2015- Pres Network Science Society

#### INTERNSHIPS

---

7/2013-8/2013 Cambridge University, Cambridge UK. Supervised by Prof. Edward Bullmore

#### AD HOC REVIEWER

---

Human Brain Mapping, Neuroimage, The Journal of Complex Networks, PLOS ONE, Brain Connectivity

#### TEACHING EXPERIENCE

---

2008-2012 HPER-P391 (now listed as SPH-K391) Biomechanics laboratory sections during Fall, Spring, and Summer sessions.

#### UNDERGRADUATE SUPERVISION

---

2014- Pres Jeffrey Rumschlag  
2014-2015 Jennifer Huang

#### PEER-REVIEWED PUBLICATIONS

---

1. **RF Betzel**, M Fukushima, Y He, XN Zuo, O Sporns (in preparation). Finding events in time-varying functional connectivity.
2. B Mišić, **RF Betzel**, M de Reus, MP van den Heuvel, O Sporns (in preparation). Multivariate structure-function relationships in human brain networks.
3. **RF Betzel**, B Mišić, Y He, XN Zuo, O Sporns (Under review). Functional modules reconfigure at multiple scales across the human lifespan.
4. **RF Betzel**, A Avena-Koenigsberger, J Goñi, Y He, M de Reus, A Griffa, PE Vértés, B Mišić, P Hagmann, JP Thiran, MP van den Heuvel, XN Zuo, ET Bullmore, O Sporns (2015). Generative models of the human connectome. Neuroimage.

5. B Mišić\*, **RF Betzel**\* (co-first authors), A Nematzadeh, J Goñi, A Griffa, P Hagmann, A Flammini, YY Ahn, O Sporns (2015). Cooperative and competitive spreading on the human connectome. *Neuron*, 86, 1518-1529.
6. O Sporns, **RF Betzel** (2015). Modular Brain Networks. *Annual Review of Psychology*. 67(1)
7. B Mišić, J Goñi, **RF Betzel**, O Sporns, AR McIntosh (2014). A network convergence zone in the hippocampus. *PLOS Computational Biology*, 10(12), e1003982.
8. A Avena-Koenigsberger, J Goñi, **RF Betzel**, MP van den Heuvel, A Griffa, P Hagmann, JP Thiran, O Sporns (2014). Using Pareto optimality to explore the topology and dynamics of the human connectome. *Philosophical Transactions of the Royal Society B: Biological Sciences*, 369(1653) 20130530.
9. **RF Betzel**, L Byrge, Y He, J Goñi, XN Zuo, O Sporns (2014). Changes in structural and functional connectivity among resting state networks across the human lifespan. *Neuroimage*, 102(2), 345-357.
10. J Goñi, MP van den Heuvel, A Avena-Koenigsberger, NV de Mendizabal, **RF Betzel**, A Griffa, P Hagmann, B Corominas-Murtra, JP Thiran, O Sporns (2014). Resting-brain functional connectivity predicted by analytic measures of network communication. *Proceedings of the National Academy of Sciences, USA*, 111(2), 833-838.
11. **RF Betzel**, A Griffa, A Avena-Koenigsberger, J Goñi, P Hagmann, JP Thiran, O Sporns (2013). Multi-scale community organization of the human structural connectome and its relationship with resting-state functional connectivity. *Network Science*, 1(3), 353-373.
12. J Goñi, A Avena-Koenigsberger, NV de Mendizabal, MP van den Heuvel, **RF Betzel**, O Sporns (2013). Exploring the morphospace of communication efficiency. *PLOS ONE*, 8(3), e58070.
13. **RF Betzel**, MA Erickson, M Abell, BF O'Donnell, WP Hetrick, O Sporns (2012). Synchronization dynamics and evidence for a repertoire of network states in resting EEG. *Frontiers in Computational Neuroscience*, 6, 74.

PRESS

---

1. Mišić et al 2015 (Neuron)

Indiana University press release:

<http://news.indiana.edu/releases/iu/2015/06/social-network-brain-model.shtml>

Neuroscience News:

<http://neurosciencenews.com/neural-networks-meme-brain-mapping-2134/>

Scientific Computing:

<http://www.scientificcomputing.com/news/2015/06/twitter-tracking-model-sheds-light-how-information-spreads-brain>

#### POSTERS AND CONFERENCE PROCEEDINGS

---

1. RF Betzel et al (October 2015). Functional modules reconfigure at multiple scales across the human lifespan. Annual meeting of the Society for Neuroscience. Chicago, IL.
2. B Mišić et al (October 2015). Multivariate structure-function relationships in human brain networks. Annual meeting of the Society for Neuroscience. Chicago, IL.
3. H Mohr et al (June 2015). Large-scale integration and segregation of functional brain modules during rapid learning processes. Annual meeting of the Organization for Human Brain Mapping. Honolulu, HA.
4. RF Betzel et al (June 2015). Generative models of the human connectome. Annual meeting of the Organization for Human Brain Mapping. Honolulu, HA.
5. B Mišić et al (June 2015). Cooperative and competitive spreading on the human connectome. Annual meeting of the Organization for Human Brain Mapping. Honolulu, HA.
6. RF Betzel et al (October 2014). Changes in structural and functional connectivity among resting-state networks across the human lifespan. Annual meeting of the Society for Neuroscience. Washington, DC.
7. RF Betzel et al (October 2013). Multi-scale community organization in the human connectome and its relationship with functional connectivity. Annual meeting of the Society for Neuroscience, San Diego, CA.
8. A Avena-Koenigsberg et al (October 2013). Using Pareto optimality to explore the topology and dynamics of the human connectome. Annual meeting of the Society for Neuroscience, San Diego, CA.

9. J Goñi et al (October 2013). Resting brain functional connectivity predicted by analytic measures of network communication. The Indiana Neuroimaging Symposium, Bloomington, IN.
10. RF Betzel et al (May 2013). Multi-scale community organization in the human connectome and its relationship with functional connectivity. IGERT Research Showcase, Bloomington, IN.
11. A Griffa et al (April 2013). Group representative partitions of human brain structural networks. Annual meeting of the International Society for Magnetic Resonance in Medicine, Salt Lake City, UT.
12. J Goñi (November 2012). Predicting resting-state functional connectivity by modeling random-walk processes on structural connectivity. Annual meeting of the Society for Neuroscience, New Orleans, LA.
13. RF Betzel (November 2011). Recurrent functional network topologies reveal a finite dynamic repertoire in resting-state EEG. Annual meeting of the Society for Neuroscience, Washington, DC.
14. MA Erickson (September 2011). Functional network organization of schizophrenia and healthy control participants in resting state EEG. Annual meeting for the Society for Research in Psychopathology, Boston, MA.

#### INVITED TALKS

---

1. NetSci 2015 (Brain networks satellite symposium) (Zaragoza, Spain) (June 1 2015) – Generative models of the human connectome.
2. Indiana University, guest lecture (Networks of the Brain undergraduate course, taught by Olaf Sporns) (March 10 2015) – Changes in structural and functional connectivity among resting-state networks across the human brain.
3. University of Pennsylvania Complex Systems Seminar (March 6 2015) – Generative models of the human connectome.
4. University of Cambridge Brain Mapping Unit Networks Meeting (July 16 2013) – Relating structure and function: Diffusion and modularity in the human connectome.